ULTRASONIC LINEAR ARRAY EVALUATION OF CONCRETE PAVEMENTS

A DISSERTATION

SUBMITTED TO THE FACULTY OF THE GRADUATE SCHOOL

OF THE UNIVERSITY OF MINNESOTA

BY

Kyle Edward Hoegh

IN PARTIAL FULFILLMENT OF THE REQUIREMENTS

FOR THE DEGREE OF

Doctor of Philosophy

Advisor: Lev Khazanovich

June 2013

Acknowledgements

Thank you to all of those who have paved the way to the completion of my Ph.D. Thank you especially to Dr. Lev Khazanovich, who was a wonderful advisor. I'd also like to thank my extremely knowledgeable committee, Dr. Mihai Marasteanu, Dr. Henryk Stolarski, and Dr. Alena Talkachova. Maureen Jensen, Dr. Shongtao Dai and many MnDOT personnel were crucial to the success of the work presented in this dissertation. Mr. Tom Yu from the FHWA was also extremely helpful in the work presented herein. I am thankful for being given the chance to work with all of you. Of course my wife, mother, and father and all of my family and friends have been a great support system for me. Your constant encouragement has led me to where I am today.

This dissertation is dedicated to my wife and inspiration, Logan Hoegh.

Abstract

Nondestructive evaluation is an important tool for assurance of proper construction practices and selection of rehabilitation procedures for civil infrastructure. Improvements in technology for testing of concrete structures, such as the introduction of dry point contact ultrasonic arrays, allow for collection of repeatable and spatially diverse shear wave impulse time-histories. This dissertation deals with development of methods that can be used for quantitative evaluation of concrete pavement structures using ultrasound linear array systems. The synthetic aperture focusing technique was adapted to handle spatially diverse measurement pairs. Kirchoff migration and the Hilbert transform were utilized to correlate high intensity portions of the instantaneous amplitude time history envelopes to the physical location of changes in acoustic impedance of the tested medium. To mitigate the effect of limited aperture, the interpretation methods were generalized to accommodate virtual array systems and implemented to create two- and three-dimensional reconstructions of the subsurface concrete structure. This reconstruction analysis was applied for practical pavement problems such as reinforcement and layer boundary location, as well as stochastic flaw detection. Comprehensive ground truth validation on several full-scale concrete pavements confirmed the high resolution of the analytical tools developed in this dissertation.

Contents

i. List of Tables

ii. List of Figures

1 Introduction

1.1 Problem Statement and Research Objectives

The pavement infrastructure faces deterioration problems due to the increasing traffic volumes and challenging environmental conditions (Scott et. al 2003). Visual inspection is the most widely used technique for determining pavement condition. However, visual inspection does not allow for determination of the distress until it manifests at the surface. Ideally, subsurface defects should be identified in a timely manner to allow for quality control prior to completion of the construction process. For *in-situ* concrete pavements detection of distress prior to extreme subsurface damage accumulation or surface exposure can be beneficial in maintaining pavement to avoid costly rehabilitation or in determining optimal rehabilitation type and timing. Development of effective nondestructive methods and improvement of data interpretation techniques are important for increasing service life of pavements.

Various methods based on different physical principles such electromagnetic wave propagation (ground penetrating radar), eddy current (magnetic pulse induction), and infrared emission (infrared thermography) have been successfully applied for concrete pavements and several major improvements have been made in the last several decades (Malhotra et al. 2004; Manning et al., 1980; Chong et al., 2003; Davis, 2003; Davis et al., 1998; Rao et al., 2009; Washer et al., 2009; Gibson et al., 2005; Gucunski et al., 2010).

Elastic-wave based methods have also been successfully applied for many years in concrete pavement and related fields for detecting planar layer interfaces. However, complex geometries requiring evaluation or imaging of non-planar or irregular flaws is difficult using conventional methods (Carino, 2001; Scott et al., 2003; Büyüköztürk, 1998). Many improvements have been made in elastic wave-based technology to allow for the use of transducer arrays with multiple angles of transmission and reception. This improvement in repeatability and productivity of data collection opens the opportunity

for development of quantitative signal interpretation techniques that have not been feasible in the past.

The objective of the research presented in this thesis involves improvement of concrete pavement subsurface characteristic quantification capabilities. This included development of methods that can be applied to signal interpretation of ultrasonic linear array impulse time-history data or combinations, thereof. These methods were validated and used to investigate several important concrete pavement-related practical problems.

1.2 Research Approach

The methods in this thesis are developed for signal interpretation of shear wave impulse response time histories from multiple fixed distance transducer pairs in a self-contained ultrasonic linear array. This included generalizing Kirchoff migration-based synthetic aperture focusing technique (SAFT) reconstruction methods to handle the spatially diverse transducer pair locations, creating expanded virtual arrays with associated two-dimensional and three-dimensional reconstruction methods, and creating concrete pavement specific automated reconstruction interpretation methods (reinforcement detection, layer boundary detection, and stochastic flaw detection). Interpretation of the reconstruction techniques developed in this study was validated using the results of laboratory and field forensic studies. Applicability of the developed methods for solving practical engineering problems was demonstrated through several large scale case studies involving evaluation of in-service concrete pavements.

1.3 Thesis Organization

Chapter 1 formulates the problem and introduces the research objectives and approach.

Chapter 2 presents the literature review including the common needs for nondestructive subsurface diagnostics, conventional nondestructive evaluation methods, basics of elastic wave propagation in concrete, and the modern signal interpretation techniques.

Chapter 3 presents the reconstruction and automated analysis techniques developed in this thesis for interpretation of the ultrasonic linear array. This includes adaptation of the Kirchoff-based SAFT reconstruction for spatially diverse transducer pairs in a linear array, reconstruction techniques associated with virtual expansion of the array, as well as methods for automated interpretation of the reconstructions for several pavement problems.

Chapter 4 presents validation of the various signal interpretation techniques. This includes pavement specific applications such as quantification of PCC slab thickness, reinforcement location, delamination and defect inclusion detection, as well as deterioration diagnostics.

Chapter 5 presents use of the techniques presented in this thesis for various practical concrete pavement nondestructive evaluation problems. This includes evaluation of a recently constructed continuously reinforced concrete highway pavement, recently rehabilitated jointed plain highway concrete pavement, and in-service transverse joints at the Minnesota Road Research Facility.

Chapter 6 summarizes the work completed as a part of this thesis and provides recommendations for future work in related areas.

2 Literature Review

This chapter introduces typical concrete pavement applications for nondestructive evaluation (NDE). This includes diagnostic needs, such as detection of subsurface inclusions or defects, cracking or other flaws, as well as layer boundary assessment. Methods using different physical principles, that are conventionally used to nondestructively evaluate these concrete pavement problems, are discussed. Elastic wave-based methods and the various wave propagation types and relationships in concrete material are discussed. Finally, the ultrasonic linear array technology and signal interpretation methods, that are the basis for the methods developed of this thesis, are introduced.

2.1 Concrete Pavement Subsurface Diagnostic Types

There is a wide range of subsurface information that can be useful in assuring quality of pavement construction or making decisions for rehabilitation or maintenance of existing concrete pavements. This can include identification of various subsurface inclusions, flaws, or layer boundary conditions.

2.1.1 Subsurface Inclusions and Flaws

Nondestructive identification of subsurface concrete pavement inclusions is an important pavement problem. This includes location of metal reinforcements such as dowels, tie bars, or continuous reinforcement, as well as unplanned inclusions/defects such as clay balls, cracks, delamination, or voids.

Reinforcement in concrete pavement is placed at specific locations to properly function. For instance, dowels are generally placed at the mid-depth, parallel to the surface with equal embedment on both sides of jointed plain concrete pavement (JPCP) transverse joints to provide load transfer (Hoegh et al., 2008). Translation from these designed locations can lead to distress (Saxena et al., 2012; Yu et al., 2007). The importance of correct bar placement is also prevalent in continuously reinforced concrete pavement

(CRCP) and tie bars at longitudinal joints. If the location of the reinforcements can be identified, potential constructability issues can be resolved or proper rehabilitation strategies can be formulated.

Introduction of foreign materials or improper construction procedures can cause inclusions in concrete pavement if not mixed and consolidated properly (Kosmatka et al., 2011). These inclusions are not generally confined to the surface. It can be useful to evaluate the extent of these defects when determining the effect on pavement performance.

Cracking is a common phenomenon in concrete pavements. While certain pavement, such as continuously reinforced concrete pavements are designed to have a nominal level of cracking, the severity and extent often exceeds the designed amount. In addition, environmental actions such as thermal expansion and contraction, shrinkage, freeze-thaw cycling as well as heavy wheel axle loading can cause undesirable cracking in pavements leading to pavement failure. Many times the cracking in the pavement can initiate in the subsurface. Knowledge of the extent of such subsurface cracking and type can lead to mitigation actions prior to failure of the concrete pavement (Darter et al., 1993).

While delamination from corrosion in concrete bridge decks is a common distress, similar mechanisms can occur in continuously reinforced concrete pavement, or uncut tie wires in dowel baskets (Clear, 1989). The horizontal plane cracks reduce the structural capacity of the structure which leads to spalling at the surface as the crack propagates (Zollinger, 1994).

Problems with the pavement construction process can lead to improperly consolidated concrete. When present near the surface or in loadbearing areas this can lead to premature failure. For instance, poor consolidation/spalling issues around dowels in jointed plain concrete pavement can lead to lower load transfer efficiency (Rao et al., 2009)

2.1.2 Layer Boundaries

Layer boundary information is also a typical diagnostic need for NDE methods in concrete pavements. Concrete layer thickness is one of the most important parameters affecting long term concrete pavement performance. Several pavement design procedures, including the Guides for the American Association of State Highway and Transportation Officials (AASHTO), Portland Cement Association (PCA), and Illinois DOT Mechanistic Design, emphasize the importance of this parameter showing that thickness deficiency can lead to premature pavement failure (AASHTO, 1993; Packard, 1984; Salsilli, 1995). Naturally, an evaluation of as constructed pavements for acceptance and assessment of construction quality involves thickness measurements. The Federal Highway Administration developed a performance-related specification evaluation tool (Pavespec 2.0). One of the key input parameters to this tool includes thickness variation along the project. Currently many agencies use destructive methods such as coring that only allow for only a limited sampling of the in-situ pavement thickness (Grove, 2012). Nondestructive testing methods can be used to get more detailed information about the pavement thickness (Schubert et al., 2004; Edwards et al., 2012; Grove et al., 2012).

In concrete pavement rehabilitated using partial depth repair, or newly constructed two-lift concrete pavement, the bond condition at the layer boundary is critical to proper performance (Tompkins et al., 2009). If a repair material is not fully bonded with the underlying pavement, the repair material can spall at the surface. Similarly, the bond condition of two lift concrete construction can lead to a loss in structural capacity if the layers are not fully bonded.

2.2 Concrete Pavement NDE Methods

Nondestructive evaluation has been used in concrete pavements for several decades. For example, identification of subsurface concrete flaws such as cracks, delamination, spalling, and poor consolidation are common nondestructive testing diagnostic needs for concrete pavements (Abdallah et al., 2009; Ansari et al., 1992; Cheng et al., 1993; Clark

et al., 2003; Escalante, 1989; Gibson et al., 2005; Gucunski et al., 2009; Gucunski et al., 2010; Sack et al., 2009). Nondestructive methods are also used for thickness detection and layer boundary condition assessment Basu et al., 2004; Edwards et al., 2011; Schubert et al., 2004).

Common Non-destructive testing (NDT) techniques include ground penetrating radar (GPR), magnetic field tomography, and infrared thermography (Malhotra et al. 2004; Manning et al., 1980; Chong et al., 2003; Davis, 2003; Davis et al., 1998; Rao et al., 2009; Washer et al., 2009). All of these methods are based on different physical principles and have unique strengths and limitations. These methods have advanced in terms of the hardware components, signal interpretation resolution, speed of data collection, and analysis due to increases in computational capability (Belytschko et al., 1983; Bungey, 2006; Buyukozturk, 1998). A brief summary of the state of the art as well as strengths and weaknesses of these methods is given below. Elastic wave-based methods such as the dry point contact ultrasound linear array technology used in this thesis are treated separately in section 2.3.

2.2.1 Ground Penetrating Radar

Ground penetrating radar (GPR) transmits electromagnetic waves into the test medium and the reflection of those waves at interfaces of different dielectric properties gives information about changes in the test medium. The wave speed is dependent on the dielectric properties of the material, and can be used with various signal interpretation methods to determine the target depth (Cao et al. 2008; Cao et al.; 2011; Cao 2011; Abdallah, 2009; Clemena 1991; Economou et al. 2012; Louliza et al., 2001; Maierhofer, 2003; Plati et al., 2012; Scott et al., 2000).

GPR has been applied in the past for detection of reinforcement corrosion (Arndt, 2011; Clemena et al., 1992) inspection bridge deck pavement (Belli et al 2008), structural assessment (Benedetto et al., 2012; Catapano et al., 2012), highway pavement structure characterization (Maser, 1996; Maser, 2000; 1996; Maser, 2008; Maser et al. 1990;

Morey, 1998; Scullion et al., 1995), airport pavement assessment, (Moropoulou et al., 2002), concrete thickness (Davis et al., 2005, Cao et al., 2011; Saarenketo et al., 2000), and identification of delamination in concrete pavements (Li et al., 2008).

Figure 2.1 shows a MnDOT owned and operated 2.6 GHz ground-coupled antenna as well as an example output of GPR where parabolic reflections can be observed due to the presence of dowels (Cao et al., 2011). The surface of the concrete in the GPR outputs appears flat because the antenna is in continuous contact with the surface while being dragged.

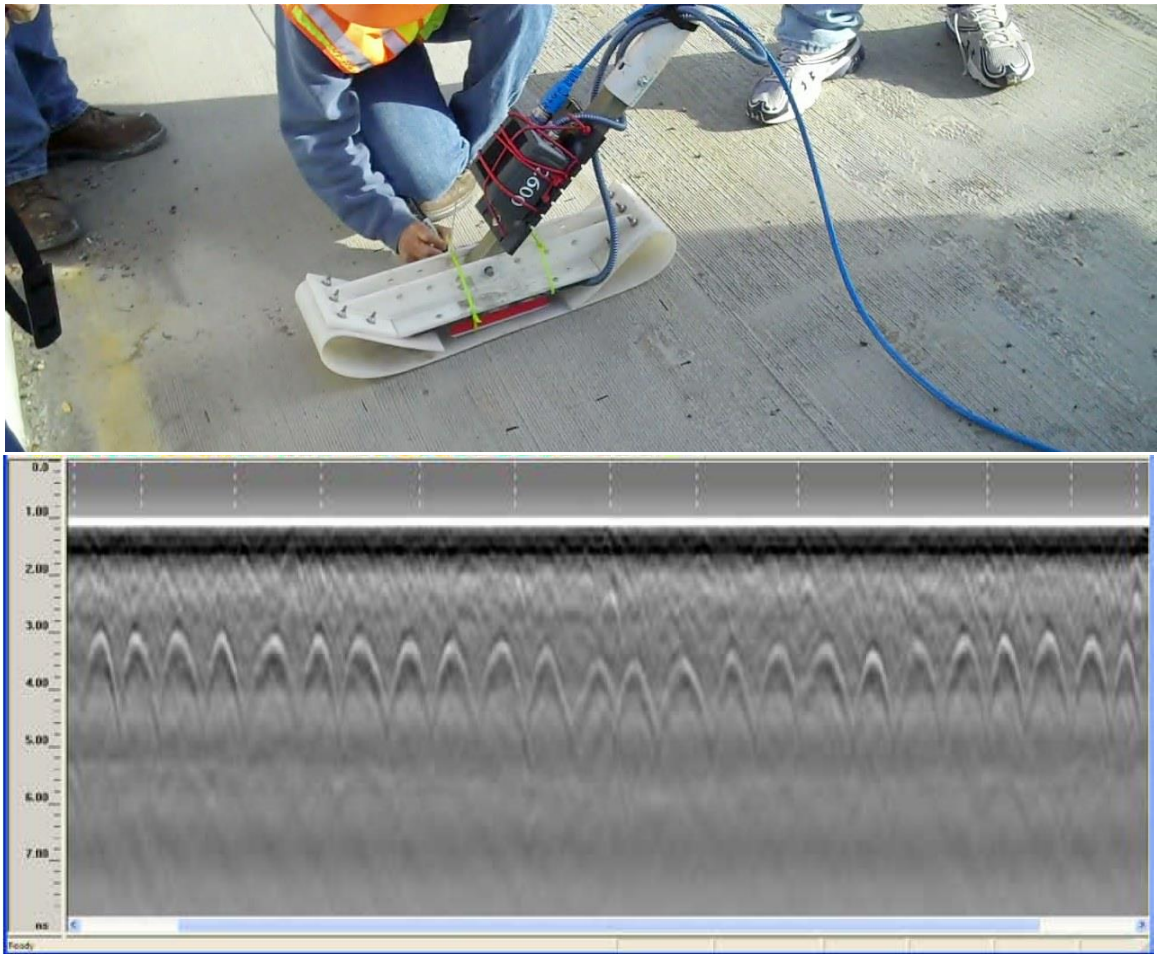

Figure 2-1. Ground coupled GPR and example output at a transverse joint.

GPR can also be operated using air coupled antennas such as the one shown in figure 2.2. Past studies show that GPR is capable of achieving high speed measurements of

pavements although the accuracy reduces with higher speeds and detecting non-uniform cracks is difficult (Griffiths et al., 1999). GPR signals are highly affected by environmental conditions including sensitivity to moisture conditions (Scott et al 2003; Griffiths et al., 1999).

Figure 2-2. Air coupled GPR mounted on a van for highway speed measurements (Maser, 2000).

2.2.2 Infrared Thermography

Infrared thermography can detect thermal anomalies by measuring infrared emission at the surface of a pavement. A difference in surface temperature can indicate a subsurface anomaly such as the presence of delamination in concrete, although this method is limited by environmental conditions and depth of the defect (Carino, 1993; Halabe, 2007; Marchetti et al., 2008). Figure 2.3 shows thermography equipment and laboratory measurements.

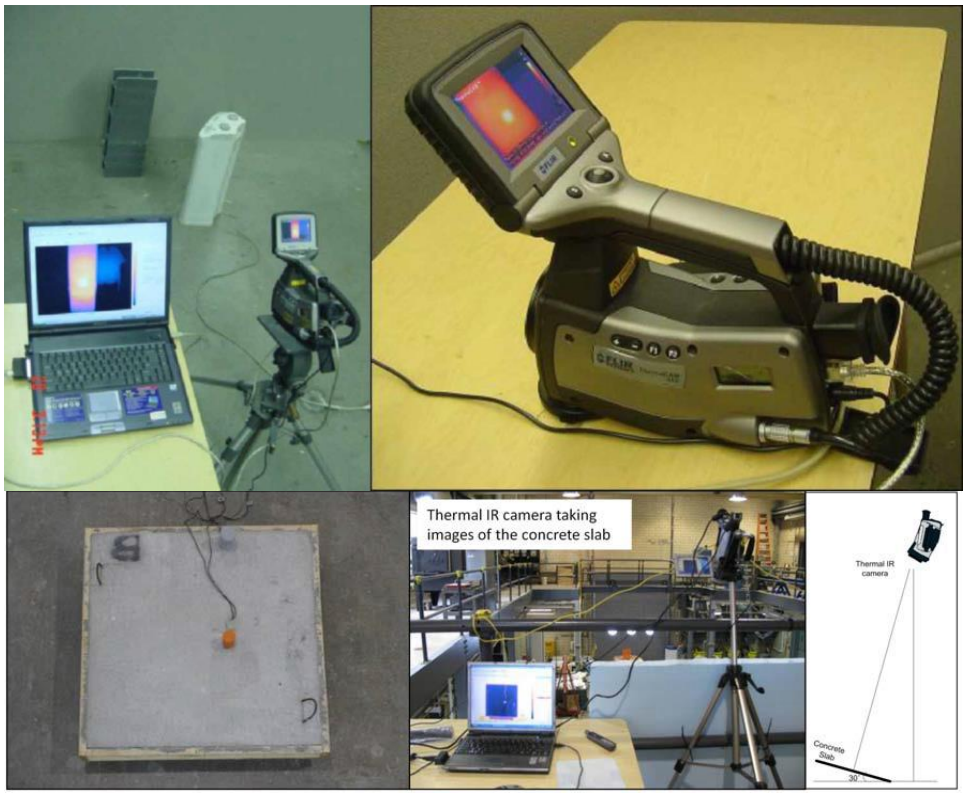

Figure 2-3. Example infrared thermography and laboratory measurements (Halabe, 2007).

2.2.3 Magnetic Pulse-Induction

Magnetic pulse-induction and the distribution of the eddy current induced by an applied magnetic field can be used to determine the position, size, shape, and orientation of metal inclusions in a pavement. Figure 2.4 shows an example measurement with a pachometer which is a conventional eddy current based method. Numerous evaluations of the accuracy of one magnetic pulse-induction device, the MIT Scan-2, have shown it to be a reliable tool for locating metal inclusions with high accuracy (Hoegh et al., 2008; Hossain et al., 2006). However, if either the dimensions or metal properties are not known it is difficult to determine the location of the subsurface inclusion. It should be noted that this method does not detect any type of non-metallic inclusions or defects (Rao et al., 2009).

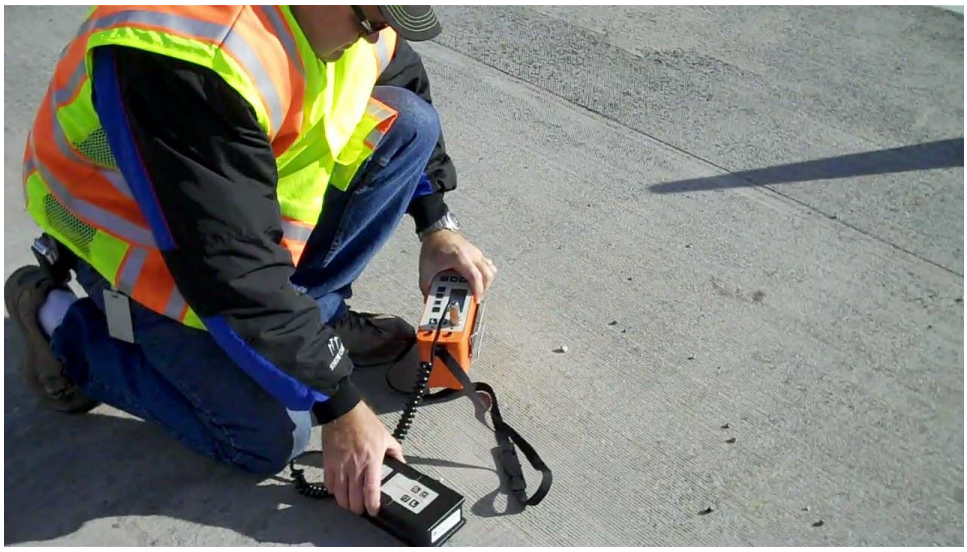

Figure 2-4. Example eddy current magnetic based device (pachometer).

2.3 Elastic Waves in Concrete

The rapid oscillatory motion of molecules produced by vibration of a body is referred to as sound (Junger et al., 1972). Unlike waves that can travel in a vacuum, such as an electromagnetic wave (Griffiths, 1999); sound waves require a physical medium where the wave travels through vibration of particles progressively through individual equilibriums (Junger, 1972). In general, the mechanism of sounding methods in mediums such as concrete pavements involves application of a force causing a distortion in the concrete which results in elastic waves propagating in the medium (Soize, 2001).

2.3.1 Elastic Wave Relationships

When exposed to a short duration external impact, concrete reacts approximately like an elastic solid medium. The distortion and subsequent movements in the concrete can be described using three general modes of wave propagation categorized by the coverage and direction of particle motion with respect to propagation direction: P-waves, S-waves, and R-waves (Graff, 1991). The compression (also known as longitudinal or primary) waves (P-wave) has particle motion parallel with the direction of wave propagation. The transverse (also known as shear) wave (S-wave) has particle motion perpendicular to the wave propagation direction. The Rayleigh wave (R-wave) is a combination of P- and S-

waves where particles move in a retrograde elliptical direction (Krstulovic-Opara et al., 1996; Zhu et al., 2004). Figure 2.5 shows a point source impact in an elastic solid with these three wave modes. It can be observed that the R-wave propagates along the surface, and the P-wave and S-waves propagate throughout the solid in a hyperbolic nature (Bolotin, 1961; Bolotiin et al., 1960; Colton et al., 1998).

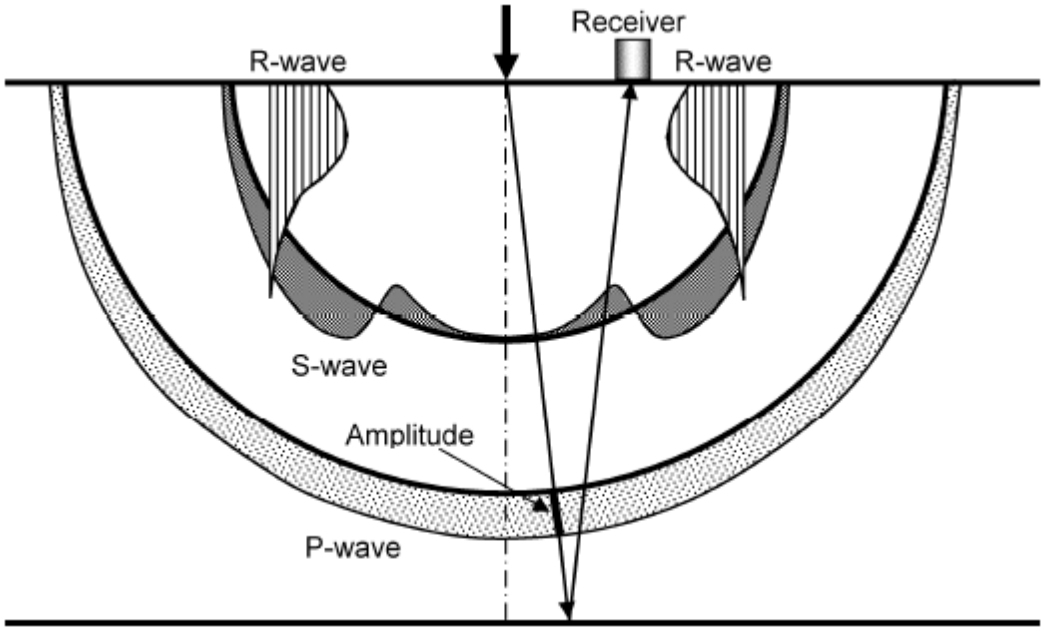

Figure 2-5. Elastic wave propagation (Carino, 2001).

If concrete is approximated as an isotropic and elastic medium, the relationship between elastic parameters (Modulus, Poisson's ratio), density, and wave velocity in concrete has the form shown in equations 2.1 (Schubert et al., 2008; Carino 2001):

$$C_P = \sqrt{\frac{E(1-\mu)}{(1-\mu)(1-2\mu)\rho}} \qquad [2.1(a)]$$

$$C_S = \sqrt{\frac{E}{2(1+\mu)\rho}} \qquad [2.1(b)]$$

$$C_R = C_s \frac{0.87+1.12\mu}{1+\mu} \qquad [2.1(c)]$$

Where E is Young's modulus of elasticity, μ is Poisson's ratio, ρ is density, C_P is the compression or pressure wave (P-wave) velocity, C_S is the transverse or shear wave (S-wave) velocity, and C_R is the Rayleigh wave (R-wave) velocity. The ultrasonic linear array method used in this study is based on shear waves. Assuming a typical value for Poisson's ratio in concrete, $\mu = 0.2$, the velocity of the wave types has the following relationship with respect to shear waves:

$$C_S = 0.61C_P = 1.09C_R \quad [2.2]$$

Table 2.1 gives some additional information including the particle motion, relative wave speeds, and energy content of the various wave types (Graff, 1991).

Table 2-1. Wave type information (adapted from Graff 1991; Carino, 2001)

Wave Type	Particle Motion	Propagation Medium	Relative Wave Speed, $\mu = 0.2$	Energy Content % (Graff 1991)
P-wave	Parallel to propagation direction	Solid, liquid, or gas body wave	0.61	7
S-wave	Perpendicular to propagation direction	Solid body wave	1	26
R-wave	Retrograde elliptical	Surface wave	1.09	67

It can be observed from the table that the P-wave has the lowest amount of energy from a point source impact, and can propagate in mediums such as solid, liquid, or gas. Methods based on P-waves can have issues achieving the necessary penetration depth due to the low energy content, but the ability to propagate in all medium types allows for air coupled possibilities in concrete pavement diagnostics (Bhardwaj et al., 2000; Green,

2004; Luukkala, 1973). Shear waves have significantly higher energy content from a point source impact and require a solid material for propagation (Achenbach, 1973; Graff, 1991). The higher energy content for a similar point source impact allows for greater penetration depth in heterogeneous mediums such as concrete pavement. Rayleigh waves have the highest energy content but are confined to the surface at a depth approximately equal to its wavelength (Achenbach, 1973; Graff, 1991).

Elastic waves can be useful in evaluating concrete pavements because changes in subsurface properties such as flaws, inclusions, or layer boundaries cause reflections back to the surface (Barbone et al., 2004). The amount of reflection is governed by the changes in the acoustic properties as well as the incident angle according to the Zoeppritz equations (Shuey, 1985; Avseth, 2005; Achenbach, 1973; Jain, 1987). For a transverse wave with normal incidents at the boundary of interest, the reflectivity at the boundary is shown in equation 2.3 (Achenbach, 1973; Avseth, 2005).

$$\Psi_R = \frac{C_{s_1}\rho_1 - C_{s_2}\rho_2}{C_{s_1}\rho_1 + C_{s_2}\rho_2}\Psi_I = \frac{Z_1 - Z_2}{Z_1 + Z_2}\Psi_I = R_{1,2}\Psi_I \quad [2.3]$$

Where Ψ_I is the amplitude of the incident elastic wave, Ψ_R is the amplitude of the reflected elastic wave, C_{s_1} is the shear wave velocity in the incident medium, ρ_1 is the density of the incident medium, C_{s_2} is the shear wave velocity of the boundary material, ρ_2 is the density of the boundary material, $Z_1 = C_{s_1}\rho_1$ and $Z_2 = C_{s_2}\rho_2$ is the acoustic impedance of each material, respectively, and $R_{1,2}$ is the reflection coefficient between the two materials. Figure 2.6 gives an illustration of these variables for a transverse wave with normal incidence at a layer boundary.

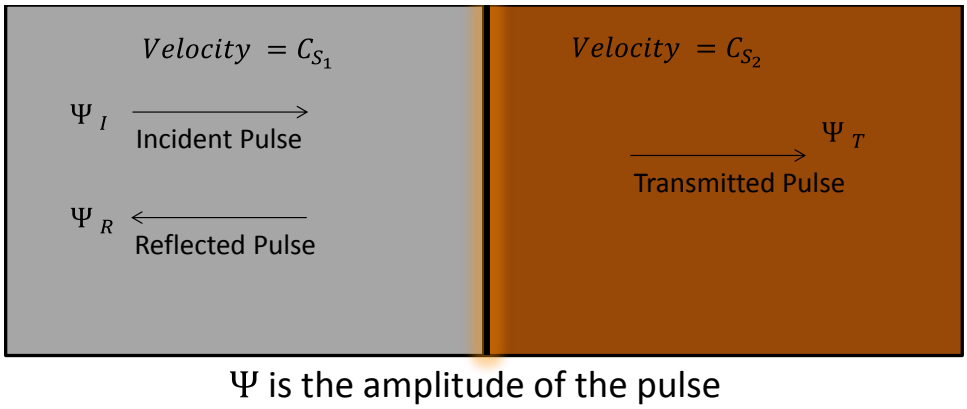

Figure 2-6. Normal incidence pulse reflected and transmitted at a boundary.

A few observations can be made from this relationship with regard to use of elastic waves for concrete pavement diagnostics. As shown in equations 1a through 1c the velocity of the wave is positively correlated to the stiffness of the material. Thus, reflections of elastic waves are extremely sensitive to interfaces such as cracks, voids, or delamination where the change in velocity and density from concrete to air is extremely high (Kellezi, 2000; Sadri et al., 2009; Sansalone et al., 1987). Additionally, it can be observed that the phase of the reflected transverse wave depends on the type of material interface causing the reflection. Thus for materials such as concrete, reflection from an interface with steel, where the acoustic impedance is higher, causes a negative reflection coefficient and corresponding π phase shift in the reflected shear wave (Achenbach, 1973; Keefe, 1992; Colton, 1998). These relationships can be used in elastic wave-based methods to obtain information about the concrete pavement related subsurface problems discussed in section 2.1.

2.3.2 Elastic Wave-Based Methods

Evaluation of pavements and bridge decks for delamination or other internal conditions is commonly conducted through rudimentary sounding methods such as chain dragging or rod sounding. These methods have been used with a certain level of success in the past due to the low cost and availability, but are purely subjective, highly affected by user error, and do not provide the necessary precision and extent of damage that more

sophisticated sounding methods can achieve (Cheng et al., 1993; Liu, 2010; Pratt et al., 1992). Various elastic wave-based methods are presented in this section.

2.3.2.1 Conventional Impact Echo

Conventional impact echo (IE) is a commonly used elastic wave based method (see figure 2.7). The IE testing technique involves generation of compression, shear, and Rayleigh waves using a mechanical impact at the surface (Schubert et al., 2001). The waves reflected from internal changes in acoustic impedance or external boundaries and recorded on the surface, where the impact was generated, give information about the structure using signal interpretation techniques normally based on spectral analysis (Scott et al., 2003).

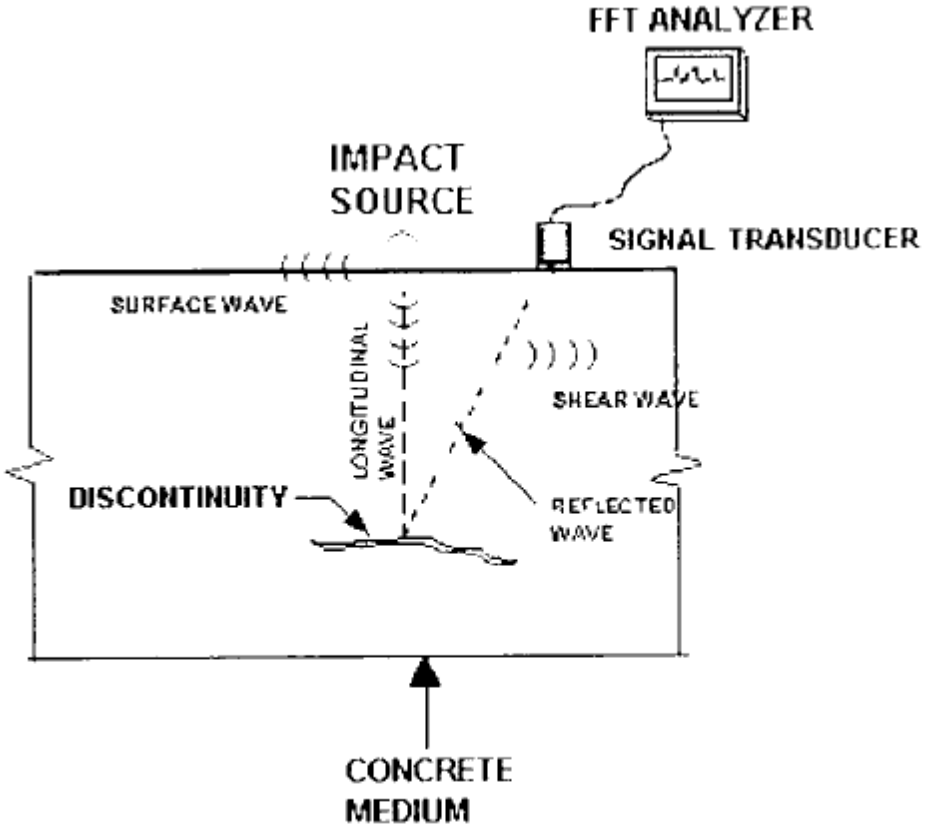

Figure 2-7. Schematic illustration of the IE test procedure (Scott et al 2003).

If the propagation velocity is known, the frequency spectrum can be used to determine the depth of the discontinuity or thickness of the material using the relationship given below (Scott et al 2003, Schubert et al., 2008):

$$D = \frac{C_p}{n*f} \quad [2.4]$$

Where D is the depth of the discontinuity, f is the resonant frequency between the impact and the discontinuity, C_p is the pressure wave (p-wave) velocity, and n is assumed to be 2 according to the full travel path to the reflecting interface and back. However the factor n = 2 has to be changed to n=4 for changes from low to high acoustic impedance (Schubert, 2008). The n=2 factor is generally valid for most impact echo problems, where interfaces causing the reflection are generally lower than the surrounding concrete material such as a concrete/air interface in delamination (Schubert et al., 2008; Schubert, 2001).

Figure 2.8 shows a conventional impact echo setup where a round metal ball is used to create the impact (Carino, 2001; Sansalone, 2007). IE is capable of detecting planar layer interfaces, which can be used for thickness determination or the detection of other plate-like inclusions. Testing with this method can be time consuming and only allows for one signal pair to be sent and received per scan. With only one mechanical impact signal and spectral analysis methods that require multiple reflections at the same boundary, there are difficulties in evaluating the complex geometries required for irregular flaw detection (Carino, 2001; Schubert, 2008; Schubert, 2003). Novel evaluation techniques and hardware such as air coupled impact echo have been developed to allow for more productive measurements and multiple measurement pairs (Borwick, 1990; Buckley, 1999; Popovics, 2012; Zhu et al., 2002; Zhu et al., 2007).

Figure 2-8. Impact echo setup with a steel ball mounted on a steel spring rod (Carino, 2001).

2.3.2.2 Spectral Analysis of Surface Waves

Spectral analysis of surface waves (SASW) is another elastic wave-based method. The dispersion of Rayleigh waves gives information about the material in which it propagates. This method has been used for applications such as estimating concrete pavement stiffness and other properties (Krstoluvic-Opara et al. 1996; Cho, 2003; Gucunski et al., 1992). The surface displacements recorded by transducers from various wave frequencies from mechanical impacts are analyzed using the setup shown in figure 2.9. This method is primarily used to determine velocities at different Rayleigh wave frequencies to indirectly obtain information about the structure from changes in modulus (Park et al., 1999; Stokoe et al., 1994).

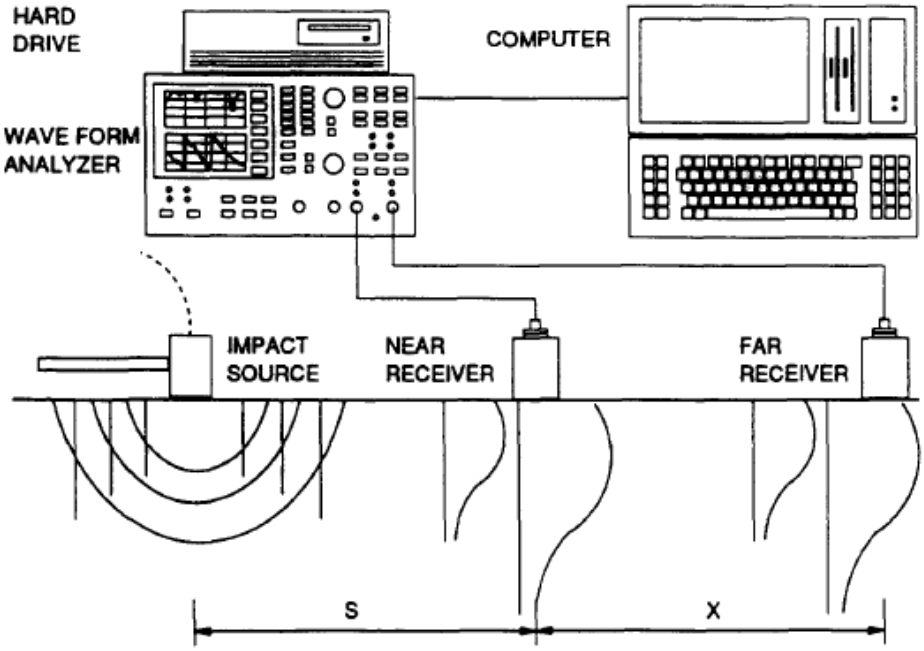

Figure 2-9. Schematic of the SASW (Gucunski, Soil Dynamics, 1992).

2.3.2.3 Ultrasonic Pulse Velocity

Ultrasonic pulse velocity (UPV) is an elastic wave based method where the impulse is emitted and received directly by an ultrasonic transducer (Popovics et al., 1992). Figure 2.10 shows various transducer pair setups used for UPV testing, where the direct arrival is received (a) on the opposite side, (b) at an angle, or (c) along the surface. For concrete pavement applications with only one-sided access, the setup shown in figure 2.10(c) is often the only applicable measurement type.

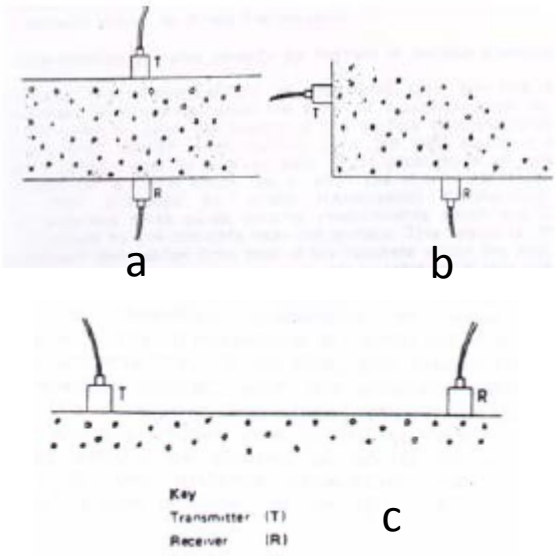

Figure 2-10. Various sending and receiving positions for UPV testing (Adapted from International Atomic Energy Agency, 2002).

The direct arrival of the elastic wave of interest (P-wave in this example) is used to determine the wave velocity by simply taking the distance traveled divided by time of propagation:

$$C_p = \frac{L}{T} \qquad [2.5]$$

where L is the path length and T is the time taken by the pulse to traverse that length.

Conventionally, the pulse is transmitted into and received from the concrete using a liquid coupling material such as grease or cellulose paste to transfer the vibration to the concrete and back. This process can be time consuming and often confines UPV testing to laboratory and/or testing of samples rather than on-site concrete pavement testing. The relatively recent technological advances in dry point contact (DPC) transducers provide a lower frequency, higher power impact without the need for liquid coupling. DPC transducers, manufactured by Acoustic Control Systems, are capable of transmitting low frequency elastic waves (30 kHz to 150 kHz) allowing for ultrasonic methods that can

penetrate greater distances in pavement applications (Nesvijski, 1997; Liang et al., 2009; Moheimani, 2003; Nesvijski, 1997; Vladisauskas et al., 2011; Vladisauskas et al., 2010; Dutoit, 2005). The "touch and go" measurements with fixed transducer locations speed up the data collection process and eliminate many of the issues with conventional ultrasonic testing as applied to concrete structures. Figure 2.11 shows an ultrasonic pulse velocity (UPV) device that was one of the first applications of these types of transducers for pavement applications (Khazanovich et al., 2005).

Figure 2-11. UK1401 ultrasonic pulse velocity device (Khazanovich et al., 2005).

2.3.3 Ultrasonic Linear Array

The conventional elastic wave based methods can produce significant deviations when detecting back walls and flaws in materials such as concrete with elastic heterogeneity caused by aggregates, pores, and cracks. The results of this limited information can lead to reliability problems due to the sensitivity to small shifts of source and sensor positions (Schubert et al., 2008).

Ultrasonic array technology provides an opportunity to mitigate the issues with limited transducer pairs, signal variability, and sensor positional shift instability, using a self-

contained arrangement of sending and receiving transducer pairs at set spacing. Ultrasonic testing is typically conducted between 750 kHz to 100 MHz, with a wide range of applications in both biomedical and industrial fields(VonRamm, O. T., 1976; Blouin et al., 1998; Minalga et al. 2012; Guzina et al., 2004; Liu, 2008; Lue, 2008; Rupitsh, 2006; Song, 2002; Spies et al., 2002). These types of systems use an array of elements within a single relatively large transducer to provide spatial diversity. Figure 2.12 shows an example ultrasonic phased array setup from (a) 1976 and (b) 2012, with elements phased within a linear array to focus the emitted wave (VonRamm, O. T., 1976; Minalga, 2012).

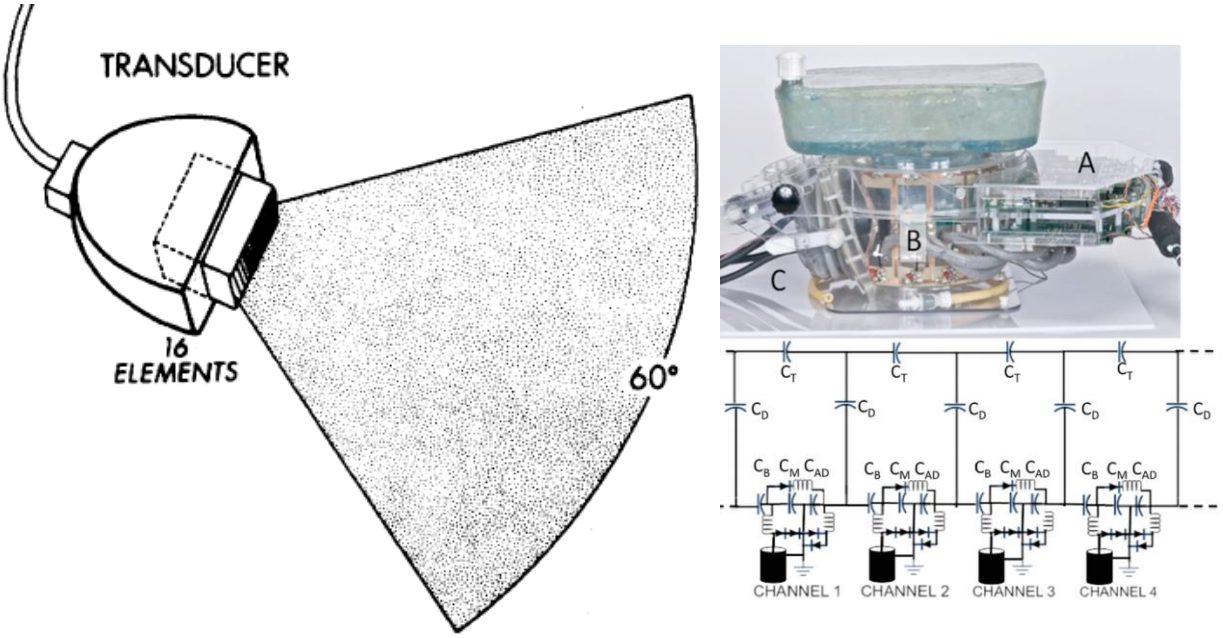

(a) VonRamm et al., 1976 (b) Minalga et al., 2013

Figure 2-12. Transducer array technology for biomedical use adapted from (a) VonRamm et al., 1976, and (b) Minalga et al., 2012.

This type of system with relatively small wavelengths does not allow for the necessary penetration depth in materials with the elastic heterogeneity of concrete. Additionally, while this setup is practical for a laboratory environment, the productivity needed for application to concrete pavement does not allow for a liquid coupled or non-mobile device where the wave is guided.

These issues can be resolved with the use of DPC transducers, similar to the UPV device shown in Figure 2.11, which eliminate the need for a manual mechanical impact. This allows for transducer arrays with multiple angles of transmission and reception that can be used to also address some of the reliability issues dealing with conventional impact echo discussed previously (Shubert et al., 2008). This arrangement allows the transducer spacing to be reduced for higher precision measurements. Two versions of DPC ultrasonic array technology are shown in figures 2.13 and 2.14. The A1220, shown in figure 2.13, consists of sets of 12 emitting transducers and 12 receiving transducers. MIRA, shown in figure 2.14, consists of a linear array of 40 sending and receiving transducers arranged in 10 channels of 4 transducers.

Figure 2-13. A1220 ultrasonic pulse-echo device.

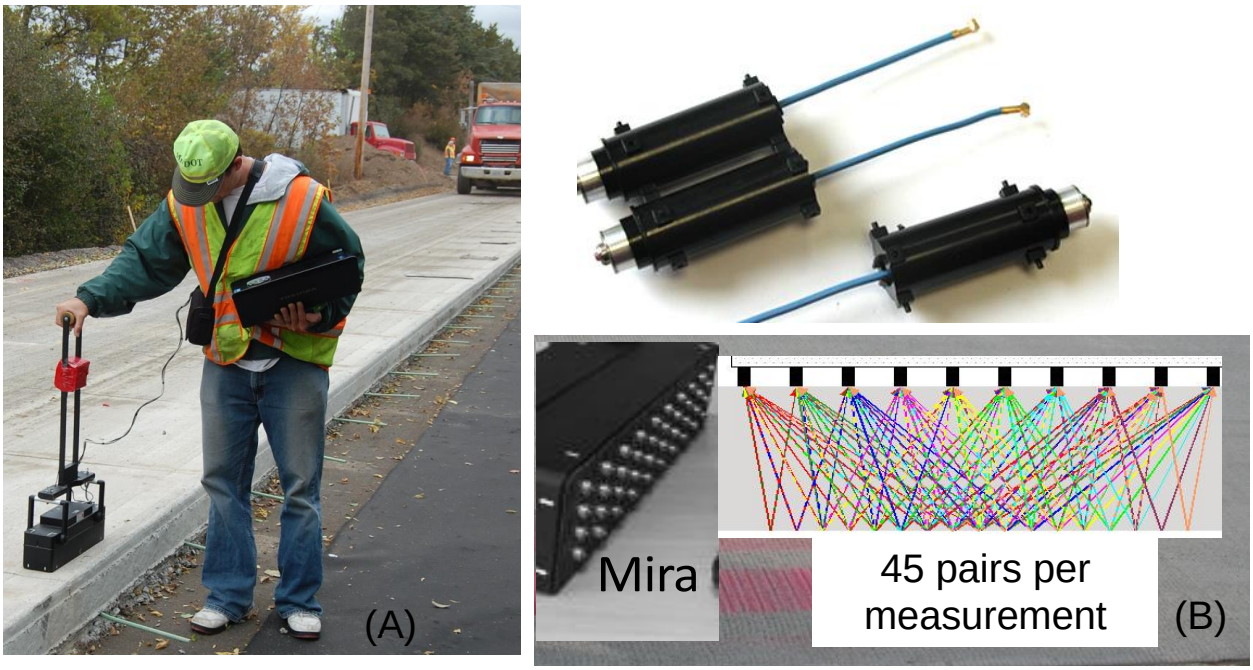

Figure 2-14. MIRA ultrasonic linear array device with a handle designed at the University of Minnesota for more productive measurements on pavement systems.

This thesis deals with the use of the ultrasonic linear array device, MIRA, for concrete pavement evaluation. As observed in figure 2.14, shear waves are emitted and received by multiple transducer pairs allowing for multiple incident angles and consistent analysis of elastically heterogeneous material such as concrete. MIRA incorporates 10 channels, each composed of four transmitting and receiving DPC transducers in a linear array. This linear array operates in a multi-static nature, allowing for 45 transmitting and receiving impulse time-history measurements.

The spacing between adjacent transducer channels is 40 mm (1.6 in.). Thus, horizontally spaced measurement pairs in each MIRA scan include nine pairs at 40 mm (1.6 in.) spacing, eight pairs at 80 mm (3.1 in.) spacing, seven pairs at 120 mm (4.7 in.) spacing, six pairs at 160 mm (6.3 in.) spacing, five pairs at 200 mm (7.9 in.) spacing, four pairs at 240 mm (9.4 in.) spacing, three pairs at 280 mm (11.0 in.) spacing, two pairs at 320 mm (12.6 in.) spacing and one pair at 360 mm (14.2 in.) spacing. Each of the probes can act as either receiver or transmitter with a typical operation ultrasonic frequency of the 50

kHz. The device records shear-wave impulse time-histories from 45 transmitting and receiving transducer pairs in each measurement. Figure 2.15 shows one of the 45 impulse time-history pairs from an example measurement. Figure 2.16 shows a schematic that would cause this type of impulse response. Various versions of this ultrasonic linear array technology have a default calibration mode and reconstruction tools (Botolina et al., 2012; Shi et al., 2009; Bishko, 2008; Mayer et al., 2008; Nesvijski, 2000; Nesvijski, 2003; Sokolov, 2003). However, analysis methods presented in this study use the raw 45 sending and receiving impulse time histories, $\Psi_{e,r}(t)$.

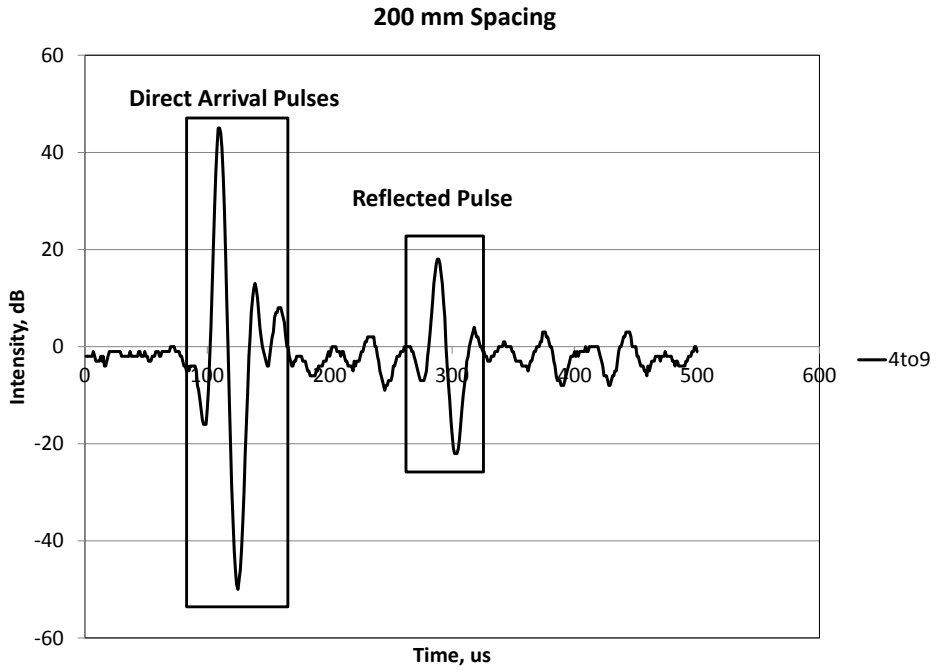

Figure 2-15. Example impulse time history from a transducer pair, Ψ_4,9 (t) from emitting channel 4 to receiving channel 9 (200 mm spacing).

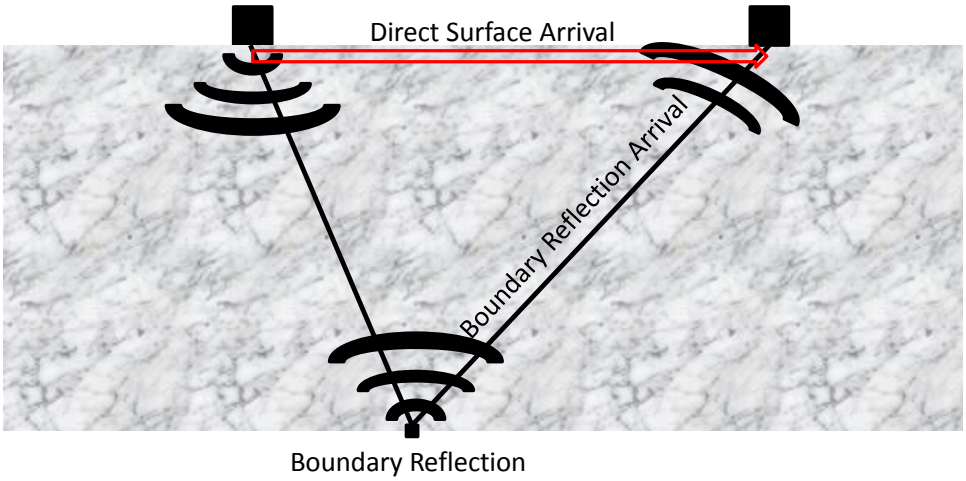

Figure 2-16. Schematic of direct and reflection arrivals.

2.4 Signal Interpretation Techniques

This section summarizes various approaches for interpretation of elastic waves in concrete pavements. While elastic wave propagation is based on different physical principles than the other nondestructive testing techniques described in section 2.2, often the mathematical approach to various signal interpretation methods are analogous between different physical techniques especially as it relates to various wave impulse time-histories (Langenberg et al., 2004, Marklein et al., 2002, Marklein et al., 2006).

2.4.1 Conventional Data Representation

Evaluation of impulse data has been conducted for many years in concrete pavement and related fields. However, the introduction of linear array systems allows for more precise focusing of the location of changes in reflectivity within concrete. Various approaches to elastic wave impulse data interpretation are given below.

The signal interpretation techniques used in this study are based on impulse time histories (A-scan). The A-scan can also be represented in terms of amplitude versus depth (z^*)

below emitting and receiving transducers. The time history values can be converted to depth using the following relationship, where c is the sound wave velocity:

$$(t = \frac{2z^*}{c}) \qquad [2.6]$$

An example of an A-scan from a conventional elastic wave based method is shown in Figure 2.17 (Schickert et al., 2003).

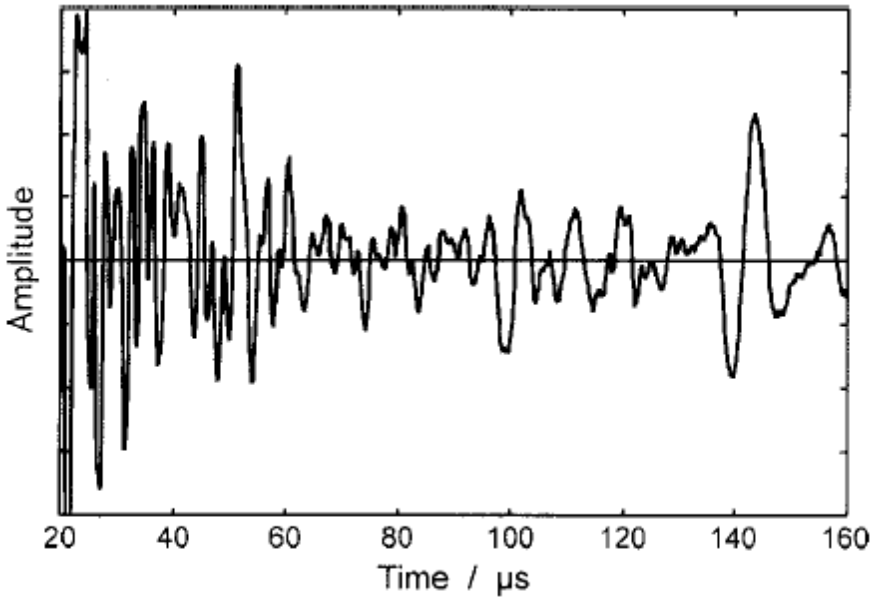

Figure 2-17. Example time domain impulse A-scan (Schickert, 2003).

The representation of the depth, t^*, is given with an asterisk because it only represents a physical depth for a reflection caused by a layer boundary. If an inclusion or other defect is present misrepresentations of the depth of the reflection is likely because an A-scan does not account for the divergent nature of the wave propagation. An example of this type of misrepresentation is given later in this section.

If A-scans are obtained along a linear aperture at regular spacing at k horizontal transducer locations, x_k, a two-dimensional cross section through the specimen depth (B-scan) can be obtained. Traditionally, the amplitude of the A-scans is converted to

grayscale to allow for a two-dimensional representation. Figure 2.18 shows a diagram of the ultrasound testing procedure of a concrete block with drilled inclusions. Figure 2.19 shows the resulting B-scan obtained from multiple A-scans taken in adjacent locations (Schickert, 2003). Two parabolas can be observed with the apex at approximately 200 mm on the left and 100 mm on the right (both identified with white borders).

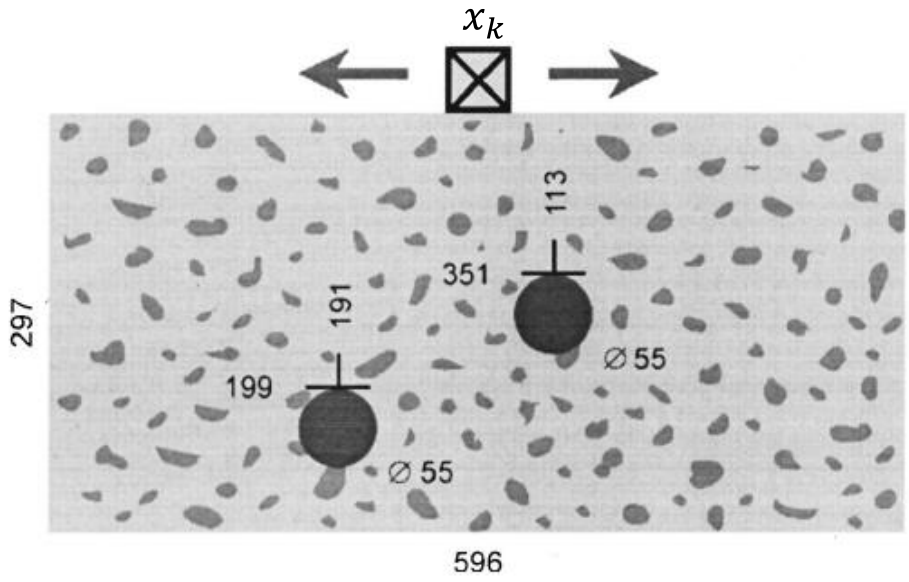

Figure 2-18. Diagram showing testing medium characteristics (adapted from Shickert, 2004).

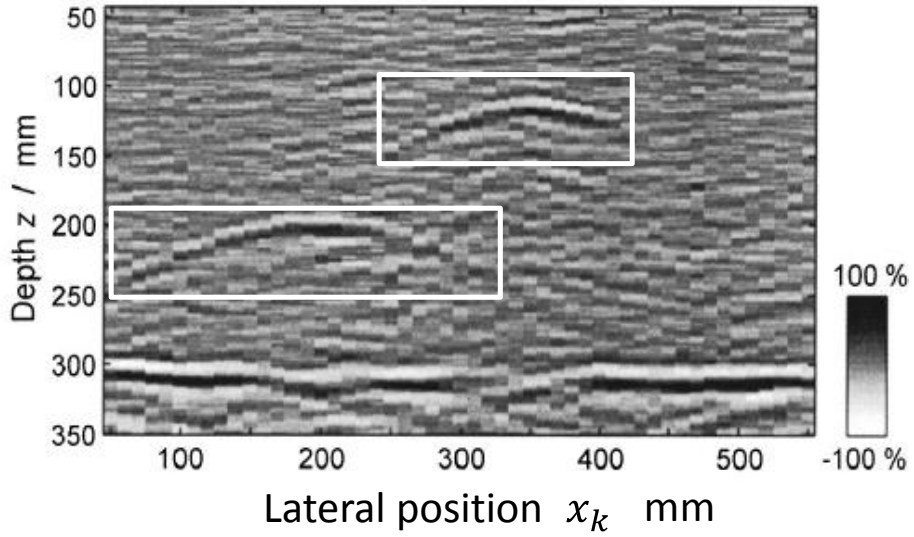

Figure 2-19. Example B-scan (adapted from Schickert, 2003).

While the conventional B-scan representation does not match the location of the inclusions, the hyperbolas caused by the inclusions can be used qualitatively by experienced engineers to intuitively get useful information about the medium. This makes B-scan analysis a popular reconstruction tool for both elastic wave and other methods (see figure 2.1 from GPR section 2.2.1). However, B-scan representations are not focused to the actual location of the inclusions where the change in acoustic impedance occurs. For more complex mediums this type lack of focus can lead to misinterpretations or lack of ability to resolve the object of interest.

2.4.2 Synthetic Aperture Focusing Technique

To determine precise locations of stiffness or density changes within of the region of interest (ROI) under multiple emitting and receiving transducer pairs, the nature of the wave front including the divergence must be accounted for (Junger et al., 1972, Rose, 2004; Marklein et al., 2002; Marklein et al., 2006). Sounding elastic wave methods often operate where the transducer diameter or contact area of the impact is small compared to the wavelength of the emitted pulse. In this case, each transducer can be treated as a point source. Figure 2.20 shows a simulation of a point source wave field from a mechanical impact normal to the surface (Schubert, 2004).

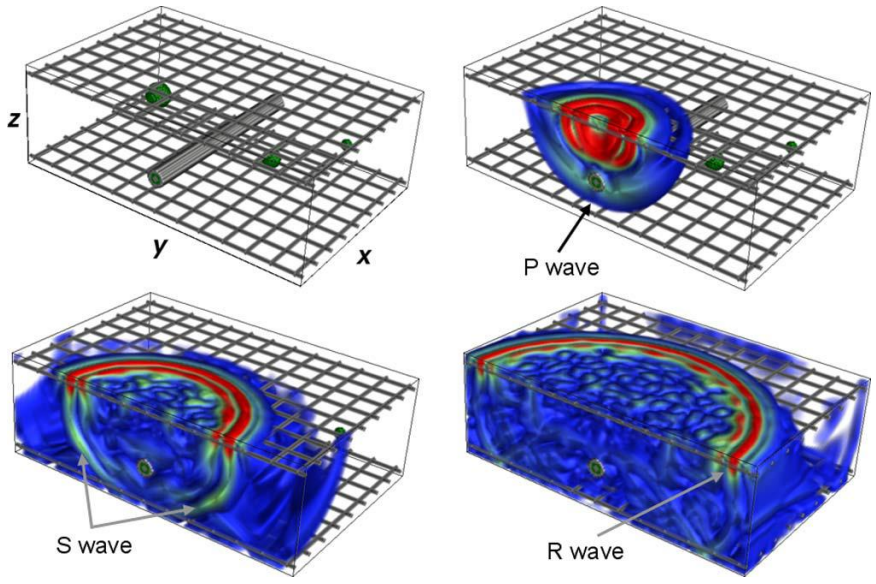

Figure 2-20. Elastic waves created by a point source (Schubert 2004).

The region of interest (ROI) below the point source can be treated as a collection of point targets. The fundamental synthetic aperture reconstruction (SAR) expression for each transducer pair for a continuous time and space model is given in equation 2.7 (Bamler 1992; Stepinski, 2007):

$$s(x_k, t) = \int_x^{\cdot} \int_z^{\cdot} f(x,z)\delta\big(t^*(t, x_k, x, z)\big)dzdx \qquad [2.7]$$

Where $s(x_k, t)$ is the received impulse at transducer position, x_k, due to emitted impulse $\delta\big(t^*(t, x_k, x, z)\big)$; $f(x,z)$ is the reflectivity function of the ROI; x and z are the horizontal and vertical positions in the ROI, respectively; and t^* is defined by the following relationship:

$$t^* = t - \frac{2}{c}\sqrt{z^2 + (x - x_k)^2} \qquad [2.8]$$

where c is the sound velocity, and t is time. Figure 2.21 shows a representation of potential contributing reflectivity point sources according to the fundamental equation if we look only at a single intensity value from the emitted impulse $\delta\big(t^*(t, x_k, x, z)\big)$.

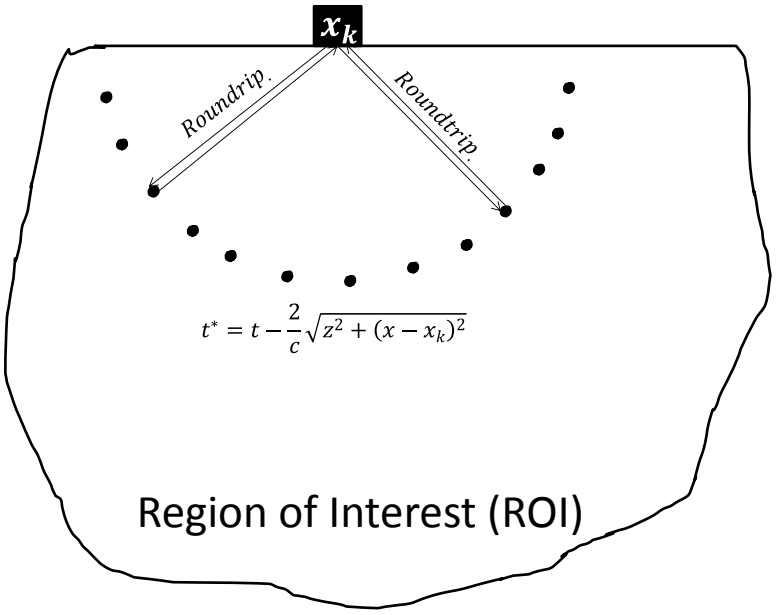

Figure 2-21. Representation of potential contributing point sources at a constant time (Roundtrip) from the emitting/receiving transducer according to the fundamental SAR expression.

The amplitude received at the surface is a combination of reflections from each position below the measurement as defined by the reflectivity function, $f(x,z)$. This function depends on the reflection coefficient of each of the potential point targets in the ROI. Since the reflection coefficients are determined by changes in acoustic impedance characteristics as discussed in section 2.3 and thus contain the information about material changes in stiffness or density, this is the information of interest in this thesis.

Since the material reflectivity $f(x,z)$ is the parameter in question, a process of estimating the relative contribution of all possible reflection points, $\int_x^{\cdot}\int_z^{\cdot}\ldots dzdx$, is made using the various impulses received at the surface, $s(x',t)$, at different transducer locations $\int_{x'}^{\cdot}\ldots dx'$. This results in an image reconstruction with relative reflectivity at each possible reflection point, $\widehat{\boldsymbol{o}}(x,z)$.

The synthetic aperture focusing technique (SAFT) can be used to determine this inverse application of relative reflectivity from the set of transducers to their respective $\widehat{\boldsymbol{o}}(x,z)$ locations within the ROI to create a reconstruction image, $[\hat{O}]$ (SAFT B-scan). To allow for integration over the various transducer locations, $\int_{x'}^{\cdot}\ldots dx'$, the impulses received at the surface versus time can be expressed in terms of distances. This can be accomplished by assuming the velocity in the medium, c, and the time shift factor, t^{SHIFT}, are constants that can be determined from the system and test medium. Discussion of the factors involved in determining the velocity and time shift factor is given in the section 2.4.3. In this case, t can be corrected so that the impulse time history is only associated with the time of flight and high reflectivity locations are associated with peaks in the impulse time history using equation 2.9:

$$t_f = t - t^{SHIFT} = \frac{2}{c}\sqrt{z^2 + (x - x')^2}. \quad [2.9]$$

If the signals are measured on the interval from x'_{min} to x'_{max}, the reconstructed image at each point $\widehat{\boldsymbol{o}}(x, z)$ can be obtained by integrating over all possible transducer impulse locations (Lingvall et al., 2003; Qi et al., 2012; Gray et al., 2002; Schmitz et al., 2000; Claerbout, 2004; Stepinski, 2007):

$$\widehat{\boldsymbol{o}}(x, z) = \int_{x'_{min}}^{x'_{max}} \alpha(x', x, z) s\left(x', \frac{2}{c}\sqrt{z^2 + (x - x')^2}\right) dx' \quad [2.10]$$

Where $\alpha(x', x, z)$ is the apodization factor that is typically a function of the distance traveled, divergence of the wave propagation, and incident angle of reflecting interface at each reflection point location with respect to the emitted/received signal. Often this factor can be omitted so that $\alpha(x', x, z) \stackrel{\text{def}}{=} 1$ assumes a sinc-shaped beam pattern representation (Duarte et al., 2003; Stepinski, 2007; Claerbout, 2004;). A weighting function (rather than the simple 1 application from above) can also be applied when deemed appropriate. Since, in practice, the signal and reconstruction matrix are discretized in time, the time of flight must often be rounded to the nearest integer. If the sampling rate is such that this causes significant error, interpolation between points can be performed.

The SAFT B-scan reconstruction image from the same data used to create the B-scan from figure 2.17 is shown in figure 2.22 (Schickert, 2003). It can be observed that the resulting representation of the inclusions is more focused than the parabola representation from the conventional B-scan. Since this divergent nature of the point source is accounted for, the reconstruction is a better representation of the reflectivity function of the material in the ROI.

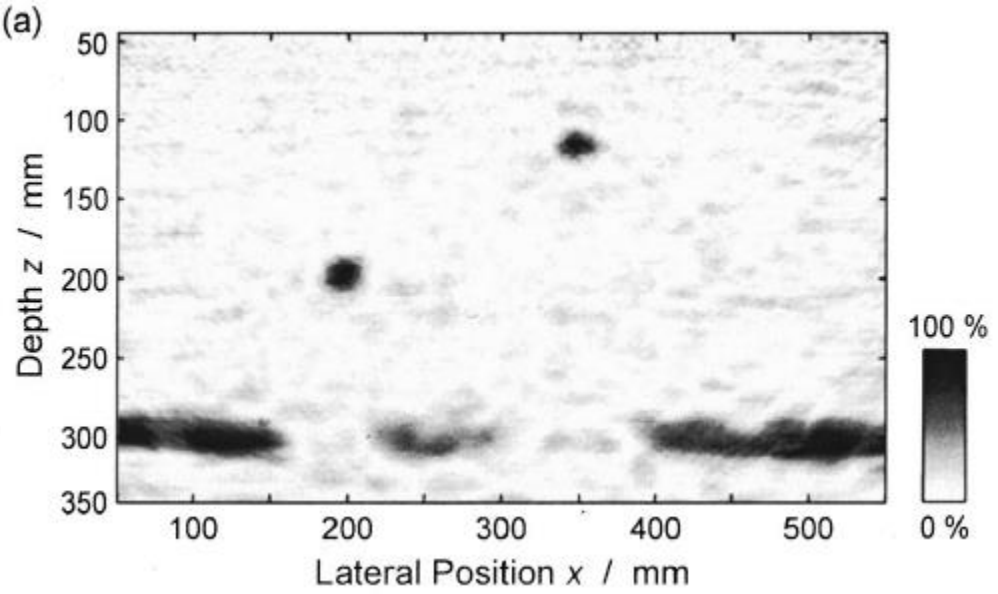

Figure 2-22. SAFT representation of the inclusions from figure 2.17 (Schickert, 2003).

The measured signals are often only available at N locations at a certain spacing Δx. Figure 2.23 shows this type of setup with x_1 being the leftmost transducer and x_N being the rightmost transducer.

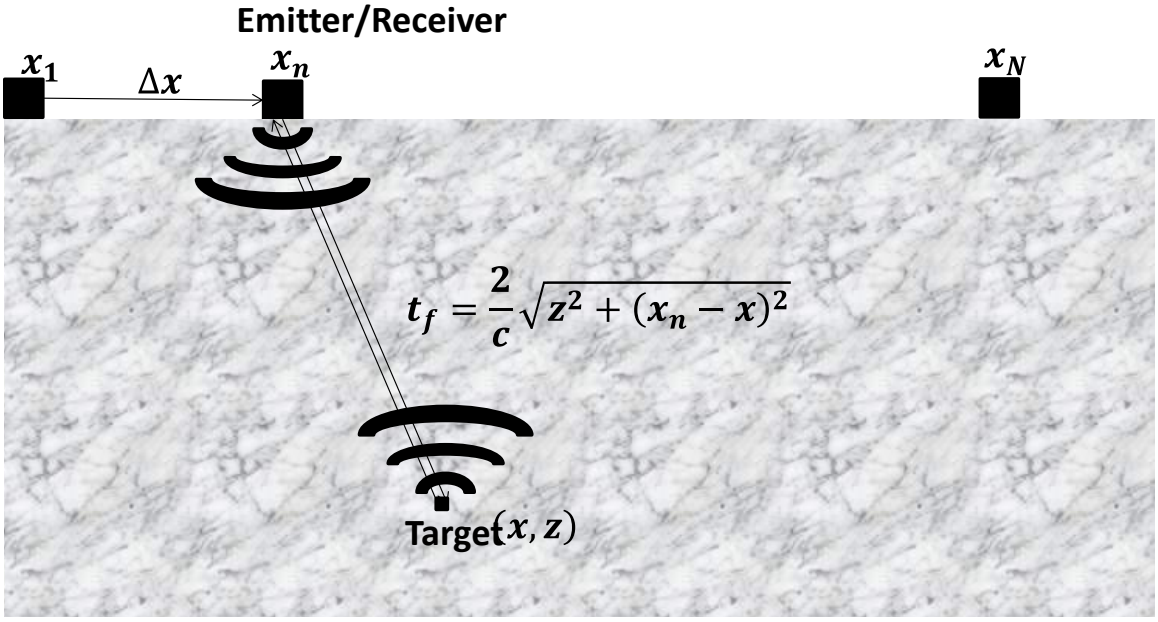

Figure 2-23. Schematic of discrete step size transducer position representation.

For this type of setup, the reconstructed image at each point $\hat{o}(x, z)$ can be obtained by summing over all possible transducer impulse locations:

$$\hat{o}(x, z) = \sum_{n=1}^{N} \alpha(x_n, x, z) s\left(x_n, \frac{2}{c}\sqrt{z^2 + (x - x_n)^2}\right) \quad [2.11]$$

If the reflection due to each transducer pair is conducted at each point $\hat{o}(x, z)$, the reconstructed image, which is an approximation of the reflectivity function of the material from the fundamental SAR equation, can be obtained. If the ROI is defined to be W units wide and have D units in depth, the following matrix formalization can be used to represent the SAFT reconstructed image:

$$[\hat{O}] = \begin{bmatrix} \hat{o}_{1,1} & \hat{o}_{2,1} & \cdots & \cdots & \hat{o}_{W,1} \\ \hat{o}_{1,2} & \cdots & \cdots & \cdots & \cdots \\ \cdots & \cdots & \hat{o}_{i,k} & \cdots & \cdots \\ \cdots & \cdots & \cdots & \cdots & \cdots \\ \hat{o}_{1,D} & \cdots & \cdots & \cdots & \hat{o}_{W,D} \end{bmatrix} \quad [2.12]$$

2.4.3 Time to Space Domain Conversion

Whether the data representation is done using the conventional or novel methods, the accuracy can only be as precise as the velocity used to convert the impulse time-history to distance. For concrete pavements with only one-sided access, P-wave velocities are normally assumed or estimated from coring. This can lead to significant errors due to variation in the concrete properties throughout the tested pavement. For the linear array system used in this study it is necessary to determine the shear wave velocity for accurate reconstruction. By determining velocity using the arrival times of the measurement system at the surface, which is possible with the ultrasonic linear array setup, the velocity at each measurement location can be determined.

This involves taking advantage of the multiple sending and receiving pairs at spatially diverse locations. Figure 2.24 shows the linear array setup where x' denotes the horizontal position of each transducer. For the purposes of this study, transducer channels will be numbered from leftmost to rightmost. For example, the leftmost transducer horizontal coordinate is referred to as x'_1 and the rightmost transducer coordinate is referred to x'_N, where n is the denoted transducer and N is the number of transducer channels being analyzed.

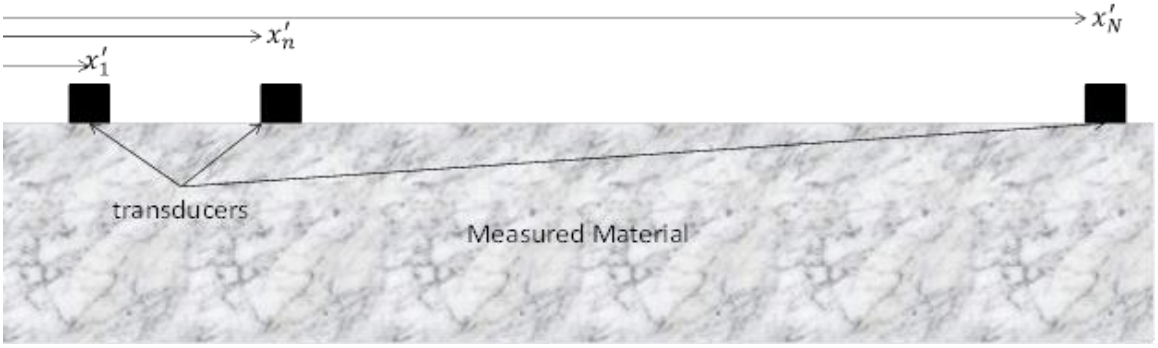

Figure 2-24. Horizontal position of each transducer.

For the impulse time-history, $\Psi_{4,9}(t)$, shown in Figure 2.15 the presence of the shear wave pulse arrival can be observed. The fixed spacing of the transducers allows for identification of the distance traveled along the surface ($x'_{e,r} = x'_r - x'_e$), where $x'_{e,r}$ is the horizontal distance between the emitting (e) transducer and receiving (r) transducer. Information associated with the time required for the wave to travel along this path ($t^f_{e,r}$) can be obtained from the impulse time-histories, $\Psi_{e,r}(t)$, such as the one shown in figure 2.15.

Therefore, with known transducer spacing ($x'_{e,r}$) and time of flight ($t^f_{e,r}$), the material shear wave velocity near the surface estimated from the direct arrival can be obtained using equation 2.12:

$$C_S^{dir} = \frac{x'_{e,r}}{t^f_{e,r}} \qquad [2.12]$$

where C_S^{dir} is the shear wave velocity from the direct arrival.

The shear wave velocity determined from equation 2.12 depends on the precision of the time-of-flight obtained from the impulse time history, $\Psi_{e,r}(t)$. However, this measurement is not a trivial task as the impulse time history depends on many factors depending on the type of piezoelectric transducer pair and boundary conditions. Some of the factors affecting extraction of the time-of-flight travel through the material from the total impulse time histories for the ultrasonic linear array used in this study, $\Psi_{e,r}(t)$ and other systems,$\Psi(t)$, include (Rachlin, 1990; Blum, 1997):

- *Internal transducer electric to mechanical (and vice versa) conversions*: delay related to transducer faces and electronic circuitry.
- *Wave arrival identification*: Delay related to the peak detection procedure.
    - For example, assuming two relatively non-dispersive materials, the initial peak of the direct arrival will be closer to the actual initial arrival for a higher velocity material than would be the case for a lower velocity material due to the difference in pulse wavelength.
- *Other factors*: There may be system uncertainty caused by factors in the sending and receiving process not considered or unknown (for example compliance of the spring loaded transducers, focusing technique of each channel, etc.).

To resolve the issues listed above, it is especially important to have detailed information on the process of signal generation and rigorous methods of determining the un-differentiable delay related to the transducer faces and electronic circuitry. Alternatively, the total system delay can be accounted for without identifying each separate factor by introducing multiple measurements. For instance, the delay from peak detection can be assumed to be constant and subtracted from the total time measurement. In the case of deep sea cores, measurements of physical standard distances with least squares regression can be used to estimate the hardware delay as shown in figure 2.25 (Blum,1997).

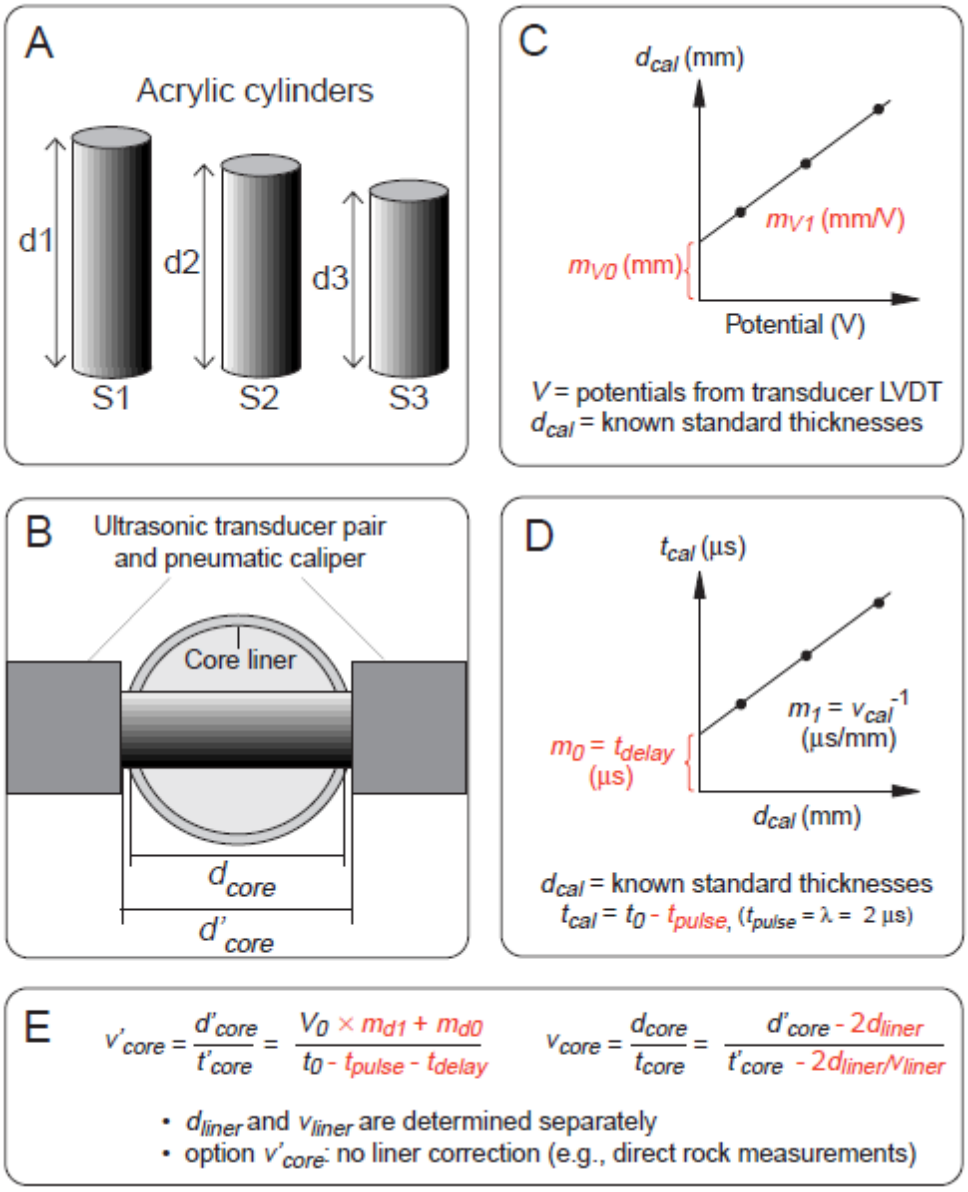

Figure 2-25. Deep sea core measurement procedure of estimating the delay related to electronic circuitry (Blum, 1997).

As shown in figure 2.25D, the difference in travel times can then be used to determine the velocity, rather than relying on calculation of the un-differentiable delay related to the transducers and electronic circuitry (Blum, 1997).

The self-contained static linear array used in this study with multiple transducer pairs permits a similar approach which eliminates the need to account for these un-differentiable factors individually.

This method is based on the following assumptions:

- At least 3 transducer pairs along the same travel path are available, where more pairs allows for more redundancy and thus increased reliability of the measurements.
- The system uncertainty issues described above can be assumed to be constant for the various pairs within a set of measurements
- The shear wave pulse is repeatable so that the same method used to identify the pulse can be used for each transducer pair
- The sampling rate frequency used to create the time-history plot is sufficient to determine the time associated with each pulse arrival for the travel path distance used to calculate the velocity (i.e. the delay between subsequent intensity measurements divided by the travel path distance should be less than required velocity precision).

Figure 2.26 shows the results of 5 sending and receiving transducer pairs from an example measurement with MIRA on a typical concrete pavement. Although the position of each of the transducer pairs is slightly different, they are all spaced at 200 mm apart. It can be observed that although the amplitude of each signal can be variable, each pulse arrival shape and arrival time is repeatable. This illustrates the capability of using this system arrangement and direct arrivals of each transmitted shear wave near the surface to calculate the shear wave velocity.

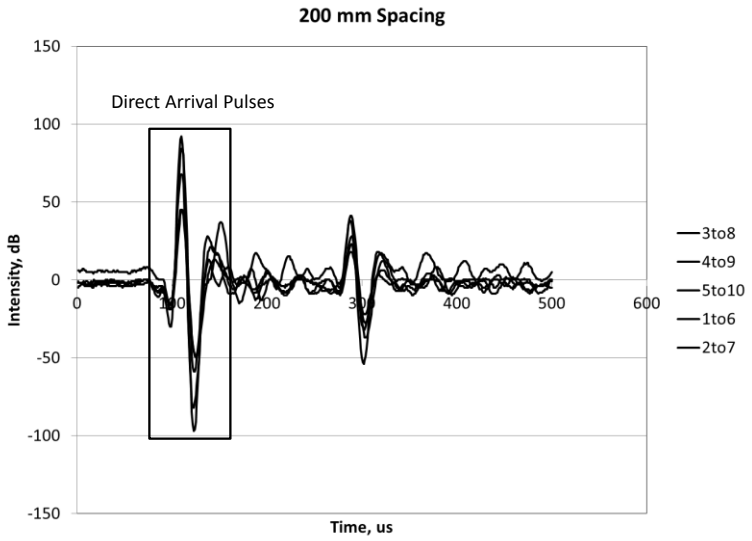

Figure 2-26. Example direct arrival pulses for five 200 mm spaced transducer channel pairs.

To illustrate the method used in this study to account for the system uncertainty, consider a case of 3 transducer pairs using the notation from the diagram shown in figure 2.24. In this method, the distance between the adjacent receiving transducer and the next receiving transducer of interest, $dx'_{n,N} = x'_N - x'_n$, is considered for the velocity calculation. The effective time of flight, $t_{e,r}^{feff}$, between transducers located at x'_N and x'_n is the difference in arrival times $dt_{n,N} = t_N - t_n$. Figure 2.27 shows the corresponding raw data time history received by both locations from the emitted transducer location.

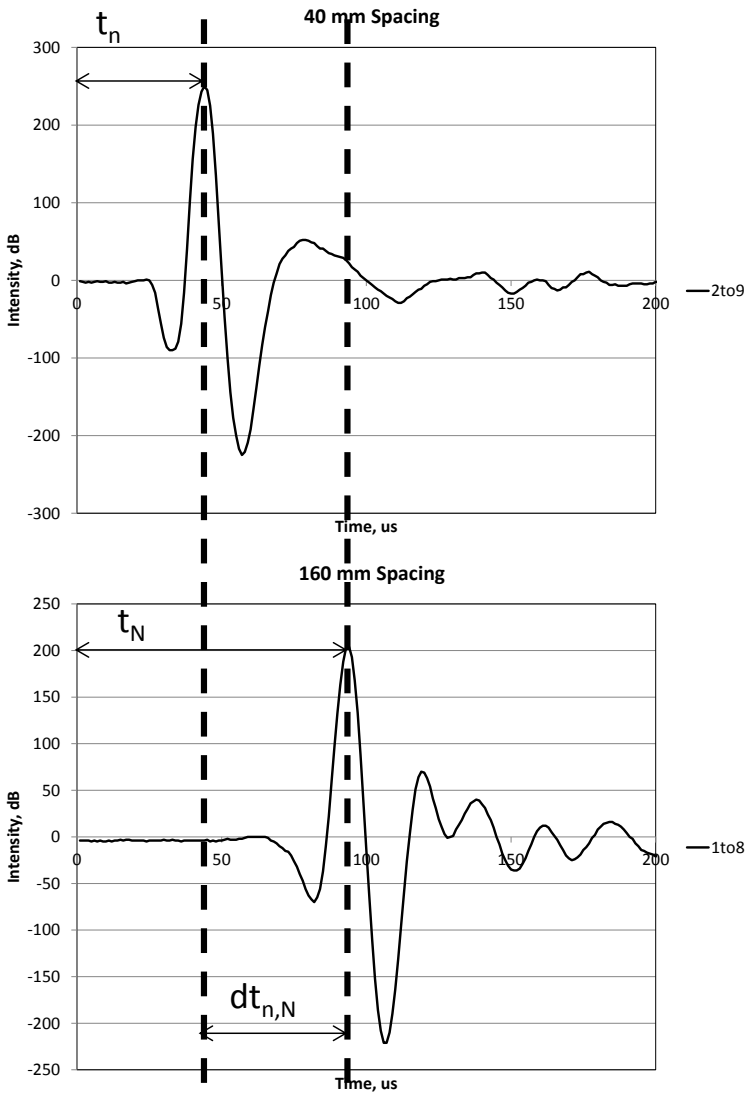

Figure 2-27. Plots showing effective time of flight calculation.

The velocity for the setup in this study can be calculated using equation 2.12 for a set of 3 transducers. Using multiple sets of 3 transducers and averaging the results increases the stability of the velocity calculations. Assuming there are a total of T transducer combinations, the calculated velocity is defined by equation 2.13:

$$C_S^{Avg} = \sum_{j=1}^{T} \frac{C_{S,j}^{dir}}{T} \qquad [2.13]$$

where j is the current combination of transducers.

As shown in equation 2.9, the impulse time history should be corrected so that high intensity impulse locations correspond to the arrival of the impulse in the time of flight analysis. Due to the same un-differentiable factors listed above dealing with velocity calculation (Graff, 1997), determination of the shift factor, t^{SHIFT}, should be accomplished by taking advantage of the redundancy of the ultrasonic linear array measurements. To allow for reconstruction analysis that focuses high reflectivity (changes in acoustic impedance) within the ROI to impulse peaks, the shift factor is determined using known spacing and associated impulse direct arrivals using the relationship given in 2.14:

$$t^{SHIFT} = \frac{1}{ER}\sum_{e=1}^{T-SP^{min}}\sum_{r=SP^{min}}^{T} t_{e,r}^{Max} - \frac{x'_{e,r}}{C_S^{Avg}} \qquad [2.14]$$

where $t_{e,r}^{Max}$ is the time associated with the maximum amplitude of the direct arrival and SP^{min} is the minimum spacing between transducers that allows for accurate detection of the peak, dependent on the sampling rate of the receiving transducer. Figure 2.28 shows an example transducer pair impulse response from the ultrasonic linear array system showing how to obtain $t_{e,r}^{Max}$.

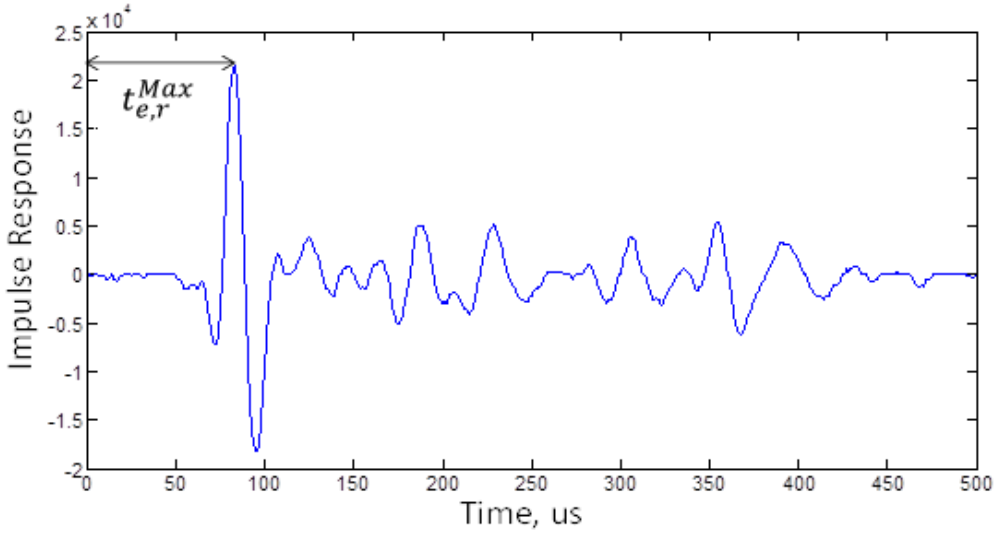

Figure 2-28. Determination of the time associated with the direct arrival.

For the ultrasonic linear array formulation, the impulse response time-histories are corrected by setting $t = t - t^{SHIFT}$ for each sending and receiving pair before it is applied to the reconstruction image.

2.4.4 Quantitative Analysis Methods

Quantitative signal interpretations can allow for more productive, and often more accurate diagnoses of the concrete pavement problems listed in section 2.1. For planar or systematic inclusions this type of analysis can be conducted using pattern recognition or layer boundary based techniques (Kausel, 1988; Kimoto et al., 2006; Kontoe et al., 2009). Identification of concrete flaws, which are stochastic in nature can be a more challenging problem. Schubert and Koehler applied a scheme for single pair impact-echo and pulse-echo data referred to as impact echo signature analysis (IESA). IESA proved to be useful for identification of these types of distresses (Schubert et al., 2001).

IESA utilizes Pearson's correlation for comparison of one-dimensional (1D) impact-echo signals with a reference signal in either the time or frequency domain. For time domain analysis, Pearson's correlation equation which was used for comparison of 1D impact-echo signals is shown below (Schubert et al., 2001):

$$C_{XY}^{j} = \frac{Cov[X, Y^{j}]}{\sqrt{Var[X]Var[Y^{j}]}} = \frac{\sum_{i=1}^{N}(x_i - x_{mean})(y_i^{j} - y_{mean}^{j})}{\sum_{i=1}^{N}(x_i - x_{mean})^2 \sum_{i=1}^{N}(y_i^{j} - y_{mean}^{j})^2} \quad [2.15]$$

Where *j* is the *j*-th signal, *i* is the *i*-th intensity value within a signal, X and Y^j are the intensity amplitude vectors of the reference and *j*-th IE scans, respectively; Cov and Var stand for the covariance and variance; x_i is the *i*-th intensity value within the reference signal and y_i is the *i*-th intensity value within the current signal, respectively; x_{mean} and y^j_{mean} are the mean intensity of the reference signal and current signal, respectively; N is the number of intensity values in each signal being compared; and C^j_{XY} is Pearson's correlation coefficient, which measures the strength of the linear dependence between IE

intensity measurements X and Y^j. Thus, a C^j_{XY} value of 0 would indicate no correlation, higher C^j_{XY} values indicate similar signals, and a C^j_{XY} value of one indicates that the two signals are related linearly.

In this method, a correlogram can be constructed of the correlation coefficients associated with each measurement location. By quantifying the similarity of the signal at each location with a reference acoustic signature representing a "damage-free" position, areas with low correlation coefficients would indicate the presence of scatterers. Through analysis of numerically simulated and laboratory test data, Schubert and Koehler concluded that the IESA method is an ideal extension to traditional evaluation procedures based on stationary reflections or resonances by large planar flaws. Figure 2.29 shows an example correlogram, where a dip in Pearson's correlation can be observed at the three simulated inclusions of a concrete plate.

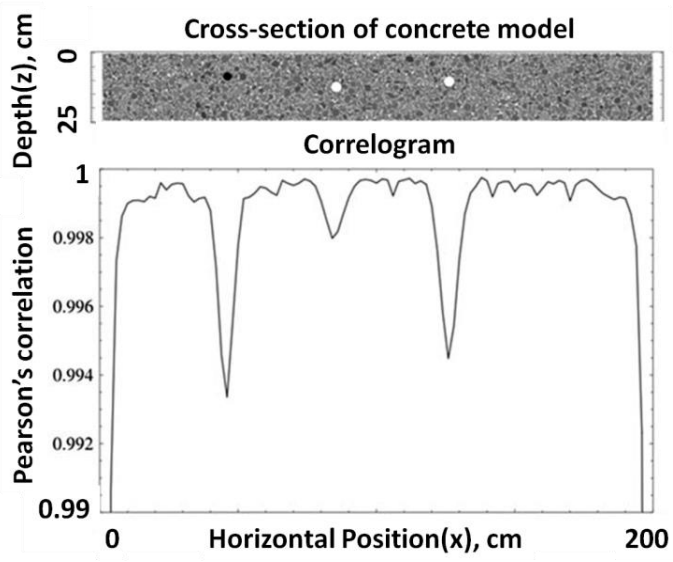

Figure 2-29. Example of an impact-echo correlogram based on Pearson's Correlation Coefficient (Schubert et al., 2001).

Schubert and Koehler also stated that a priori knowledge of a reference signal where no scatterers are present is not generally available. Further, they concluded that a 1D waveform is susceptible to misinterpretations (Schubert and Kohler, 2001). One potential misinterpretation when using this method is improper selection of the reference

signal. When evaluating 1D impulses, it can be difficult to differentiate the reflection amplitude levels caused by actual defects in the concrete from structural noise which can be caused by different aggregate types and air void distributions. In this thesis the IESA method was generalized for use with the linear array system and the reference signal issue is also considered with a proposed solution.

3 Interpretation and Analysis of Ultrasonic Linear Array Signals

This chapter describes the development of various reconstruction procedures for interpretation of the ultrasonic linear array signals. In addition, several pavement specific automation procedures were developed to increase productivity and accuracy in interpretation of a large number of reconstructions.

3.1 Reconstruction

The fundamental SAR and SAFT formulations given in section 2.4.2 were developed for interpretation of multiple signals with sending and receiving transducers at the same location. In this section, these formulations will be generalized for interpretation of signals with sending and receiving transducers located at different locations. Moreover, a signal sent from one location but received at various locations along the surface can be accounted for in this formulation.

Similar to the formulation for point source emission and reception at a single location described in section 2.4.5, the region of interest (ROI) below the testing aperture can be treated as a collection of point targets. The fundamental expression for SAR given in equation 2.7 is generalized for each emitting and receiving transducer pair positioned at $x_e'$and x_r', respectively, and can be represented as shown in equation 3.1:

$$s(x_e', x_r', t) = \int_x^{\cdot} \int_z^{\cdot} f(x,z) * \delta\big(t^*(t, x_e', x_r', x, z)\big) dz dx \qquad [3.1]$$

Where $s(x_e', x_e', t)$ is the received impulse due to emitted impulse $\delta\big(t^*(t, x_e', x_r', x, z)\big)$; $f(x,z)$ is the reflectivity function of the ROI; x and z are the horizontal and vertical positions in the ROI, respectively; and t^* is defined by the following relationship:

$$t^* = t - \frac{1}{c}\left(\sqrt{z^2 + (x - x_e)^2} + \sqrt{z^2 + (x - x_r)^2}\right) \qquad [3.2]$$

The impulse response received at the surface as a function of time, $s(x_e', x_r', t)$, is a combination of reflections from each position below the measurement as defined by the reflectivity function, $f(x, z)$. This function depends on the reflection coefficient of each of the potential point targets in the ROI as can be observed from equation 2.3. Since the reflection coefficients are determined by changes in acoustic impedance characteristics and thus contain the information about material changes in stiffness or density, this is the information of interest when creating the reconstruction images. Figure 3.1 shows a representation of potential contributing point sources for a single intensity value within $s(x_e, x_r, t)$ according to the fundamental SAR equation.

4

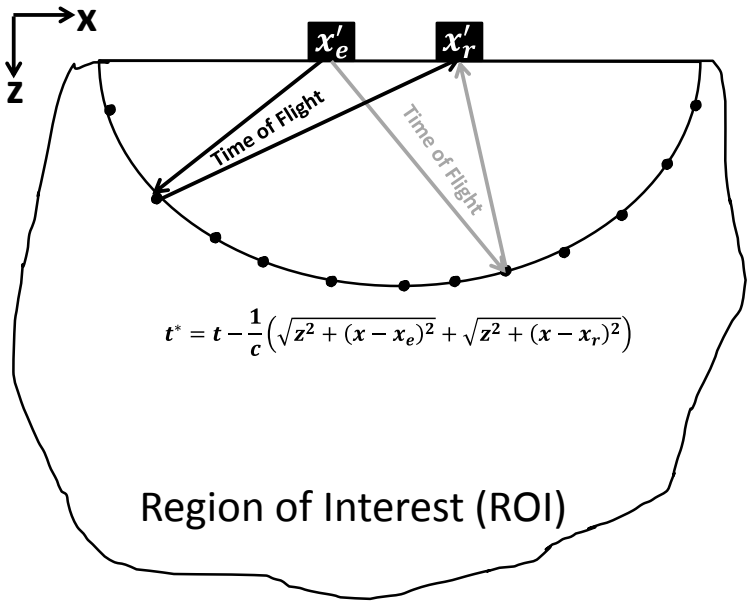

Figure 3-1. Representation of potential contributing point sources at a constant time (Roundtrip) from the emitting/receiving transducer according to the fundamental expression.

3.1.1 SAFT B-scan

The synthetic aperture focusing technique can be used for the ultrasonic linear array used in this study in a similar manner to that described for single sending and receiving pairs. To allow for integration over the various transducer locations, $\int_{x_e'}^{\cdot} dx_e' \int_{x_r'}^{\cdot} \dots dx_r'$, the impulses received at the surface versus time can be expressed in terms of distances. This can be accomplished by assuming a constant shear wave velocity, $C_S = C_S^{Avg}$, determined from equation 2.14. If the signals are emitted within interval $[x'_{emin}, x'_{emax}]$ and received within interval $[x'_{rmin}, x'_{rmax}]$, the reconstructed image at each point $\widehat{\boldsymbol{o}}(x, z)$ can be obtained by integrating over all possible transducer pair (impulse emit and receive) locations:

$$\widehat{\boldsymbol{o}}(x,z) = \int_{x'_{emin}}^{x'_{emax}} dx_e' \int_{x'_{rmin}}^{x'_{rmax}} \mathrm{A}(x_r', x_e', x, z) * s\left(x_r', x_e', \frac{1}{c}\left(\sqrt{z^2 + (x - x_e')^2} + \sqrt{z^2 + (x - x_r')^2}\right)\right) dx_r' \qquad [3.3]$$

Where $\mathrm{A}(x_r', x_e', x, z)$ is the apodization factor that is typically a function of the distance traveled, incident angle, and/or divergence of the reflection point location with respect to the emitted/received signal.

The measured signals for the setup in this study have $T = 10$ transducer locations at spacing $\Delta x' = 40mm$. Figure 3.2 shows an example linear array setup with x_1' being the leftmost transducer. For the ultrasonic linear array used in this study, the leftmost emitting transducer is located at the leftmost transducer location, $x'_{e1} = x'_1$, leftmost receiving transducer is located adjacent to the leftmost emitting transducer $x'_{r1} = x'_{e1} + \Delta x = x'_{e1+1}$, rightmost receiving transducer is located at the rightmost transducer location $x'_R = x'_T$, and rightmost emitting transducer is located adjacent to the rightmost receiving transducer location $x'_E = x'_R - \Delta x = x'_{T-1}$.

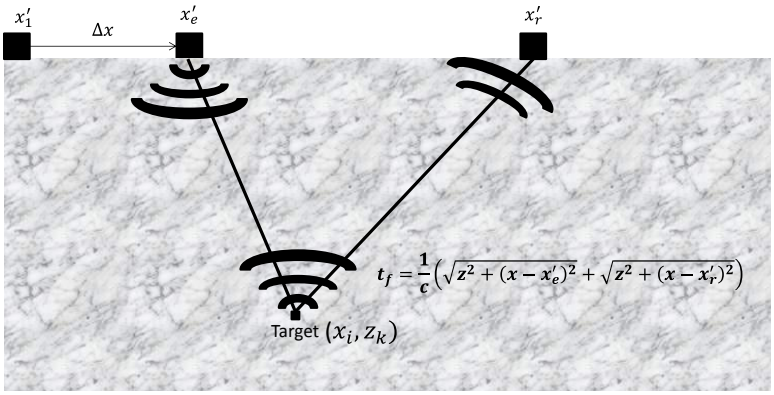

Figure 3-2. Linear array representation.

After applying the shift factor from equation 2.14 the reconstructed image is obtained at discrete points by summing over all possible transducer pair locations using the following relationship for the ultrasonic linear array in this study:

$$\widehat{\boldsymbol{o}}_{i,k} = \sum_{e=1}^{T-1} \sum_{r=e+1}^{T} \mathrm{A}(x_r, x_e, x_i, z_k) \Psi_{e,r}(x_i, z_k) \quad [3.4]$$

where,

$$\Psi_{e,r}(x_i, z_k) = s\left(x_r, x_e, \frac{1}{c}\left(\sqrt{{z_k}^2 + (x_i - x_e)^2} + \sqrt{{z_k}^2 + (x_i - x_r)^2}\right)\right) \quad [3.5]$$

where $\widehat{\boldsymbol{o}}_{i,k}$ is the image reflectivity assigned to each position within the ROI, T is the number of transducer locations, e and r are the indexes for the emitting and receiving transducers, and i and k are the indexes for the horizontal and vertical positions of the ROI.

If the ROI has W indexes in the horizontal direction and D indexes in the vertical direction, the following matrix formalization can be used to represent SAFT reconstructed image, $[\widehat{\boldsymbol{O}}]$:

$$[\hat{O}] = \begin{array}{|c|c|c|c|c|} \hline \hat{o}_{1,1} & \hat{o}_{2,1} & \cdots & \cdots & \hat{o}_{W,1} \\ \hline \hat{o}_{1,2} & \cdots & \cdots & \cdots & \cdots \\ \hline \cdots & \cdots & \hat{o}_{i,k} & \cdots & \cdots \\ \hline \cdots & \cdots & \cdots & \cdots & \cdots \\ \hline \hat{o}_{1,D} & \cdots & \cdots & \cdots & \hat{o}_{W,D} \\ \hline \end{array} \quad [3.6]$$

The apodization factor accounts for incident angle and other traits of the signal and tested medium as explained in Chapter 2. For the ultrasonic linear array used in this study for testing of concrete pavement, the apodization factor given in equation 3.7 was used:

$$A(x_r', x_e', x_i, z_k) = \alpha_e(x_e', x_i, z_k) * \alpha_r(x_r', x_i, z_k) \quad [3.7]$$

Where:

$$\alpha_e(x_e', x_i, z_k) = \frac{z_k}{\sqrt{(x_i - x_e')^2 + {z_k}^2}}$$

$$\alpha_r(x_e', x_i, z_k) = \frac{z_k}{\sqrt{(x_i - x_r')^2 + {z_k}^2}}$$

An example of typical data from the ultrasonic linear array on a continuously reinforced concrete pavement (CRCP) is given herein. Figure 3.3 shows a schematic of the CRCP structure at the example scan location. It can be observed that there is a set of three longitudinal reinforcements represented by black circles in the schematic within the ROI where the measurement was taken.

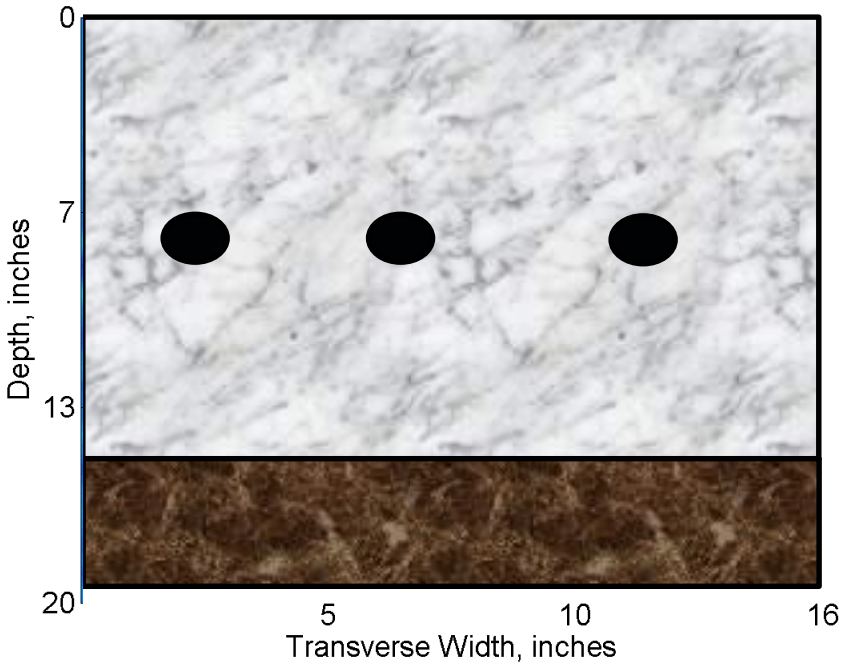

Figure 3-3. Schematic of the CRCP subsurface at the example scan location.

Figure 3.4 shows 3 example impulse responses, $\Psi_{1,6}(t), \Psi_{2,5}(t), \Psi_{3,4}(t)$ of the total 45 emitting and receiving pairs comprising the example scan. It can be observed that there are peaks in amplitude at certain locations within the time histories in addition to the direct arrival positions. While these spikes in amplitude are associated with reflectivity within the ROI, such as reinforcements and layer boundaries, the location of the cause of these reflections are difficult to interpret.

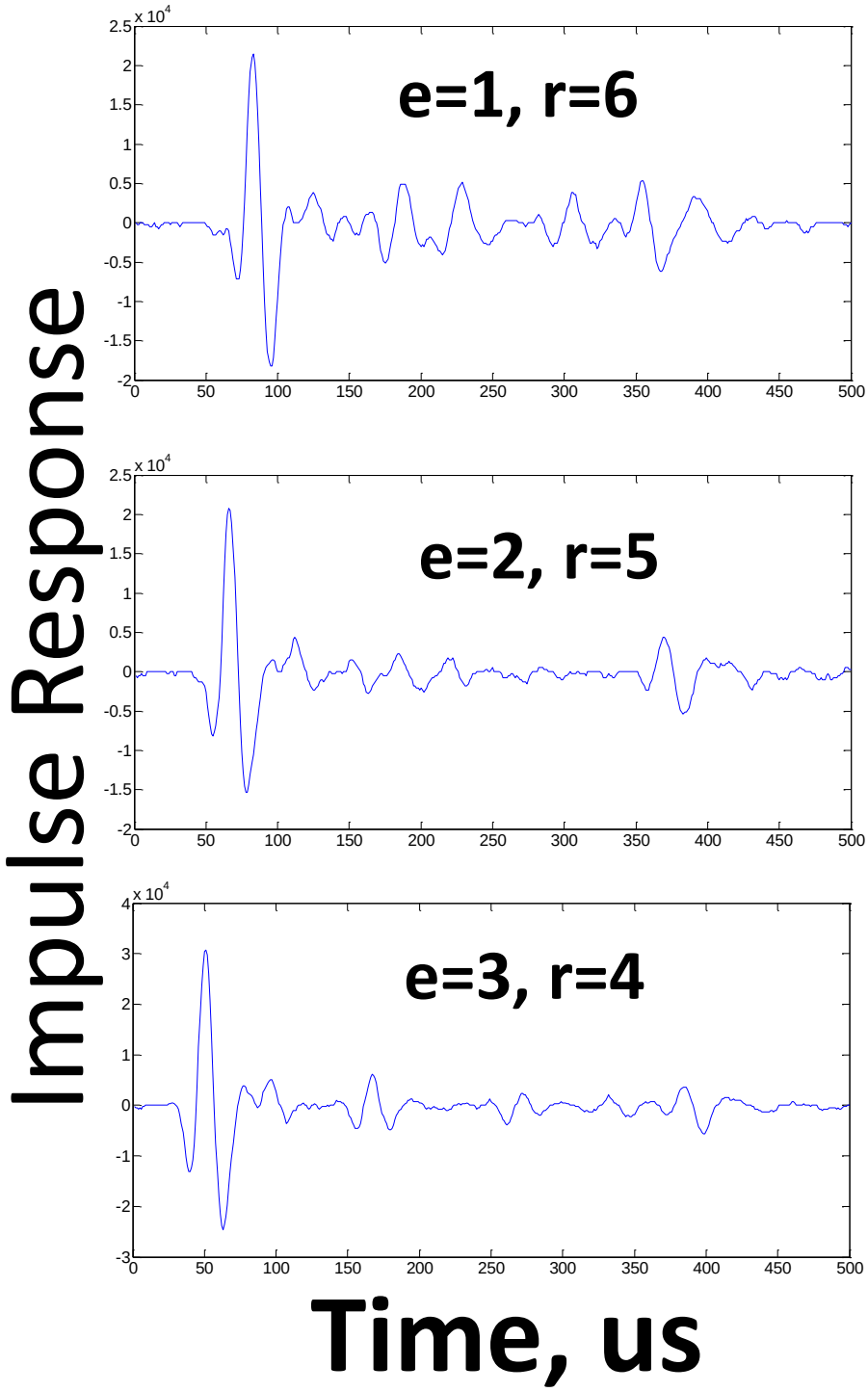

Figure 3-4. Example emitting-receiving pairs from a ultrasonic linear array scan.

Figure 3.5 shows the resulting SAFT reconstructions after using equation 3.4 to reconstruct all 45 impulse pairs, $\Psi_{e,r}(t)$. Figure 3.5(a) was reconstructed using an apodization factor of 1, and the apodization factor defined in equation 3.7 is used in figure 3.5(b). Both reconstructions give more information about the subsurface of the structure than the individual impulses. The high reflectivity locations in the SAFT reconstructions indicate the location of changes in acoustic impedance such as the reinforcements and the layer boundary. It can also be observed that the structural noise observed in figure 3.5(a) in the sound concrete portions is not present in figure 3.5(b). This illustrates that the use of the apodization factor defined in equation 3.7 improves the focusing capabilities of the SAFT reconstruction and eliminates some of the structural noise such as direct arrival intensities that do not represent the reflectivity of the ROI.

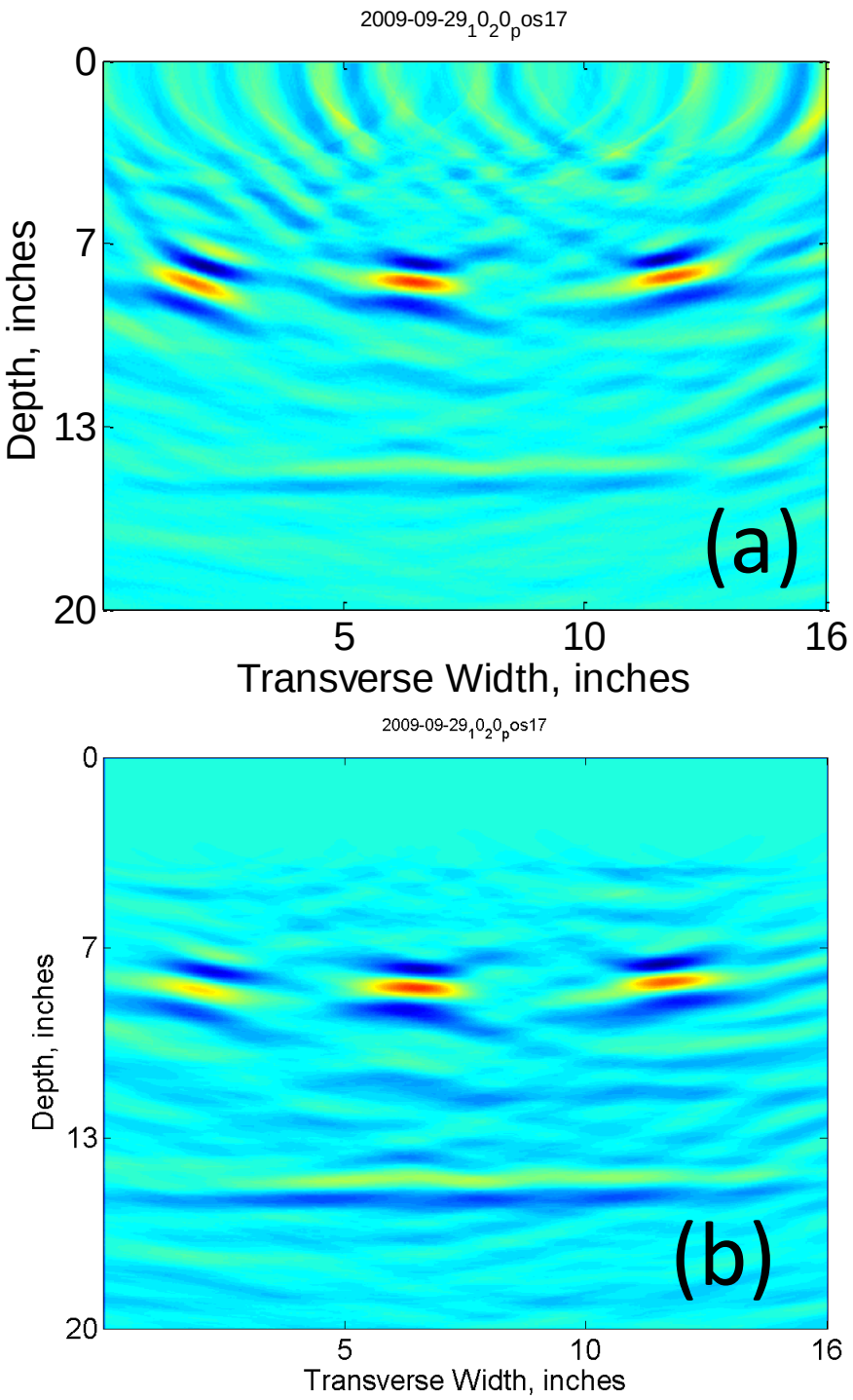

Figure 3-5. Example SAFT reconstruction with the apodization factor equal to (a) 1 and (b) defined by equation 3.7.

3.1.2 Instantaneous Amplitude SAFT B-scan (SAFT-IA)

In most cases, the reconstruction analysis for concrete pavement applications is concentrated on identifying the source of the changes in acoustic impedance in the subsurface. Further focusing of the reconstruction can be achieved by analyzing changes in instantaneous amplitude within the ROI. The Hilbert transform is useful in calculating instantaneous attributes of a time series, especially the amplitude and frequency (Hahn, 1996; Huang, 2005; Kschischang, 2006; Todoran et al., 2008; Marple, 1999; Gold, 1969; Oppenheim et al., 1989). The Hilbert transform, $\Upsilon(z)$, of a given function, $\chi(z)$, is defined by the following equation:

$$\Upsilon(z) = \frac{1}{\pi}\, P \int_{-\infty}^{\infty} \frac{\chi(s)}{z-s}\, ds \qquad [3.8]$$

Where P is the principal value of the singular integral in equation 3.8.

And the complex analytic signal, $Z(z)$, is given by:

$$Z(z) = \chi(z) + j\, \Upsilon(z) \qquad [3.9]$$

Since the reconstruction analysis in this study is based on focusing high reflectivity (changes in acoustic impedance) within the ROI with high magnitude pulse amplitudes, calculation of instantaneous amplitudes during the SAFT analysis can give higher resolution reconstructions. Since the Hilbert Transform envelope will be used during the reconstruction process, a slight change in the determination of the shift factor calculation from equation 2.15 must be applied. Equation 3.10 is used to calculate the instantaneous amplitude of each individual transducer pair impulse time history.

$$\Psi_{e,r}^{IA}(t) = \sqrt{\left(\Psi_{e,r}(t)\right)^2 + \left(\frac{1}{\pi} P \int_{-\infty}^{\infty} \frac{\Psi_{e,r}(s)}{t-s}\, ds\right)^2} \qquad [3.10]$$

Where $\Psi_{e,r}^{IA}(t)$ defines the instantaneous amplitude envelope of time history pair, $\Psi_{e,r}(t)$, and P is the principal value of the singular integral in equation 3.10.

Use of the instantaneous amplitude, $\Psi_{e,r}^{IA}(t)$, permits a modification of equation 2.15, which was based on the raw impulse time-history signal. The instantaneous amplitude-based shift factor, $t^{SHIFT,Hilb}$, for each signal is given in equation 3.11:

$$t^{SHIFT,Hilb} = \frac{1}{ER}\sum_{e=1}^{T-SP^{min}}\sum_{r=SP^{min}}^{T} t_{e,r}^{MaxH} - \frac{x'_{e,r}}{C_S^{Avg}} \qquad [3.11]$$

Where $t_{e,r}^{MaxH}$ is the time of flight to the maximum instantaneous amplitude of each $\Psi_{e,r}^{IA}$. Figure 3.6 shows the same example transducer pair impulse response, $\Psi_{e,r}$, given in figure 2.28 (top) and corresponding instantaneous amplitude envelope, $\Psi_{e,r}^{IA}$, illustrating the process of obtaining $t_{e,r}^{MaxH}$(bottom).

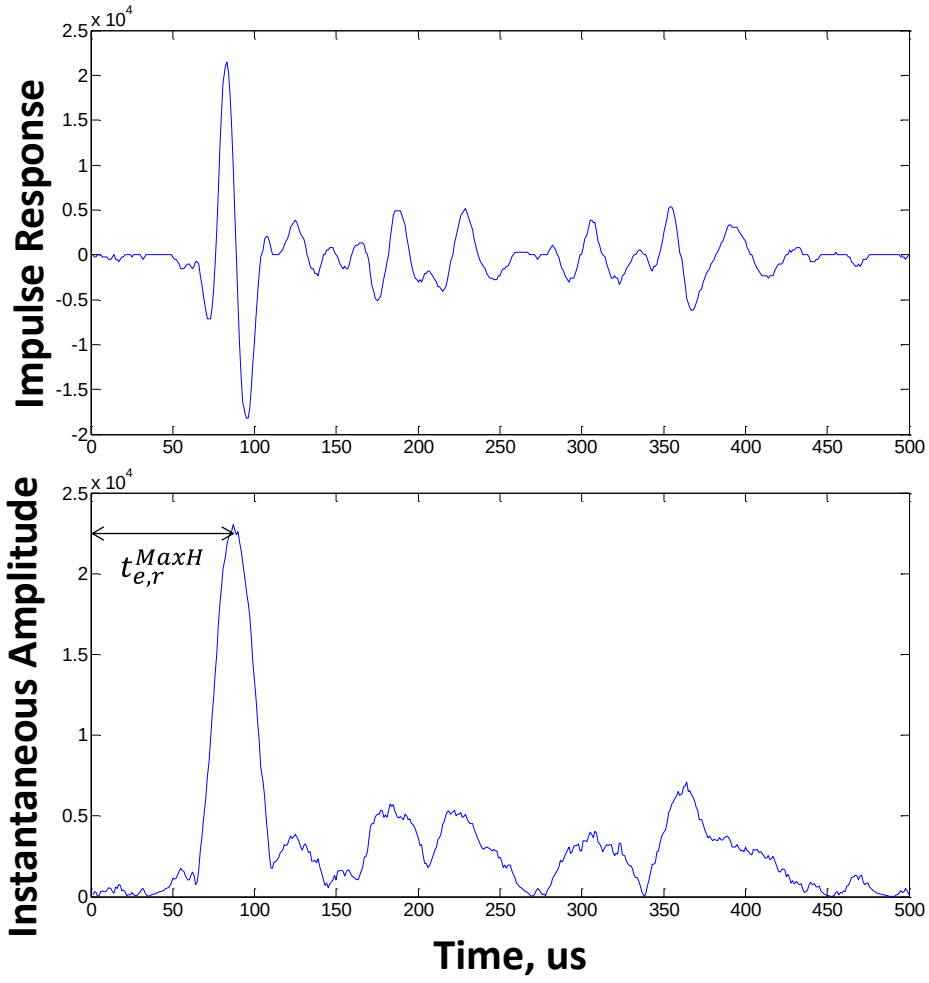

Figure 3-6. Determination of the direct arrival peak using the instantaneous amplitude envelope.

The full-waveform impulse responses are corrected by setting $t = t - t^{SHIFT,Hilb}$ for each sending and receiving pair before it is applied to the SAFT-IA B-scan reconstruction.

Similarly, for the ultrasonic linear array SAFT reconstructions based on the Hilbert transform, we are interested focusing the instantaneous amplitude within the ROI to changes in acoustic impedance. Therefore, the Hilbert transform is performed for each horizontal coordinate SAFT reconstruction in a similar manner to equation 3.10 as follows:

$$\hat{o}^{IA}(x,z) = \sqrt{\left(\hat{o}(x,z)\right)^2 + \left(\frac{P}{\pi}\int_{-\infty}^{\infty}\frac{\hat{o}(x,s)}{z-s}ds\right)^2} \quad [3.12]$$

Where $\hat{o}^{IA}(x,z)$ defines the instantaneous amplitude-based SAFT reconstruction and P is the principal value of the singular integral in equation 3.12. If the ROI is represented by a $W \times D$ set of points located in W columns, equally spaced in the horizontal direction, and D rows equally spaced in the vertical direction, the following matrix formalization can be used to represent SAFT-IA reconstructed image, $[\hat{O}]^{IA}$:

$$[\hat{O}]^{IA} = \begin{bmatrix} \hat{o}^{IA}_{1,1} & \hat{o}^{IA}_{2,1} & .... & .... & \hat{o}^{IA}_{W,1} \\ \hat{o}^{IA}_{1,2} & .... & .... & .... & .... \\ .... & .... & \hat{o}^{IA}_{i,k} & .... & .... \\ .... & .... & .... & .... & .... \\ \hat{o}^{IA}_{1,D} & .... & .... & .... & \hat{o}^{IA}_{W,D} \end{bmatrix} \quad [3.13]$$

Figure 3.7 shows the SAFT reconstruction from section 3.1.2 from a scan on reinforced concrete along with a column of the matrix data along the edge of a reinforcement.

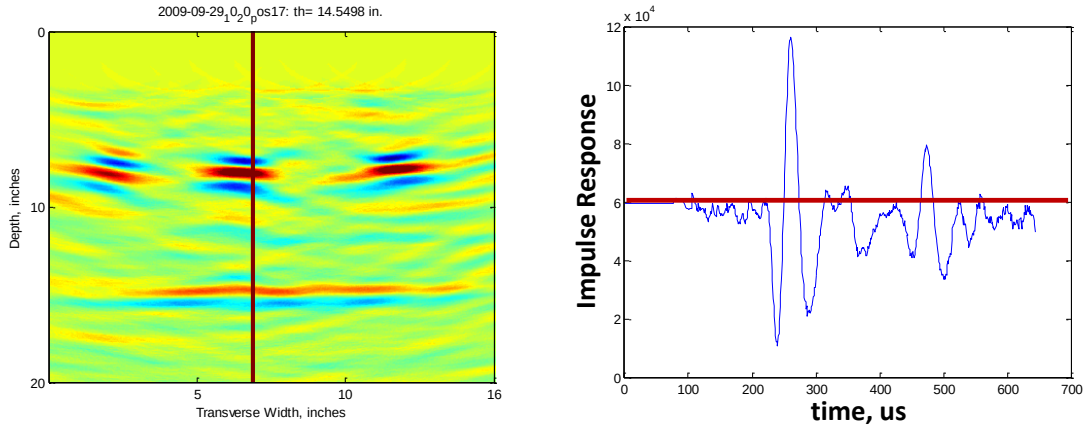

Figure 3-7. SAFT reconstruction and example column data.

Figure 3.8 shows the SAFT-IA reconstruction after taking the Hilbert transform given in equation 3.12 as well as the column representation of reflectivity along the same edge of the reinforcement, $\hat{o}_{i,k}^{IA}$. It can be observed that the high reflectivity in the SAFT-IA reconstruction better indicates the location of the reinforcement and layer boundary than the original SAFT reconstruction.

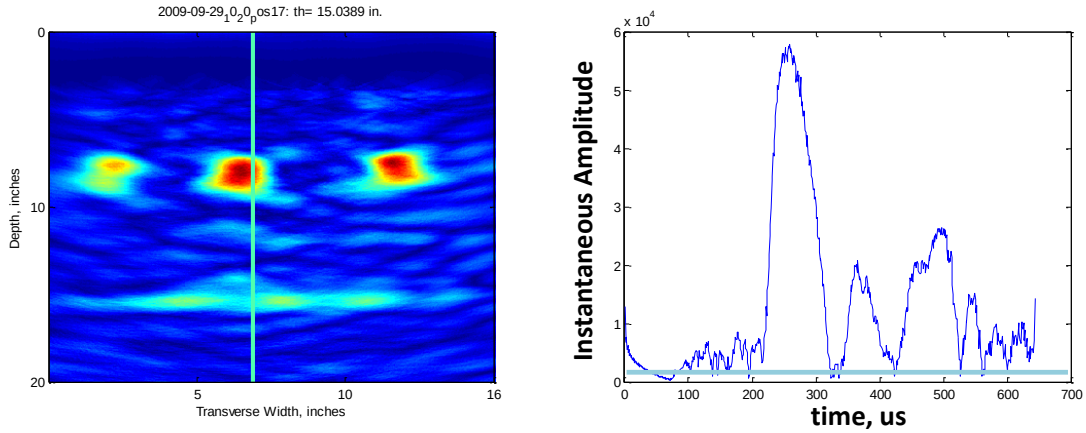

Figure 3-8 SAFT-IA reconstruction and example column data.

Furthermore, the use of the Matlab[tm] two dimensional smoothing function ('disk' filtering) allows for additional elimination of structural noise in the reconstruction (Matlab, 1998). Figure 3.9 illustrates the resulting filtered SAFT-IA B-scan of the forensic verification of the reinforcement location. It can be observed that the depth of the reinforcement corresponds to the higher instantaneous amplitude region within the SAFT-IA B-scan reconstruction.

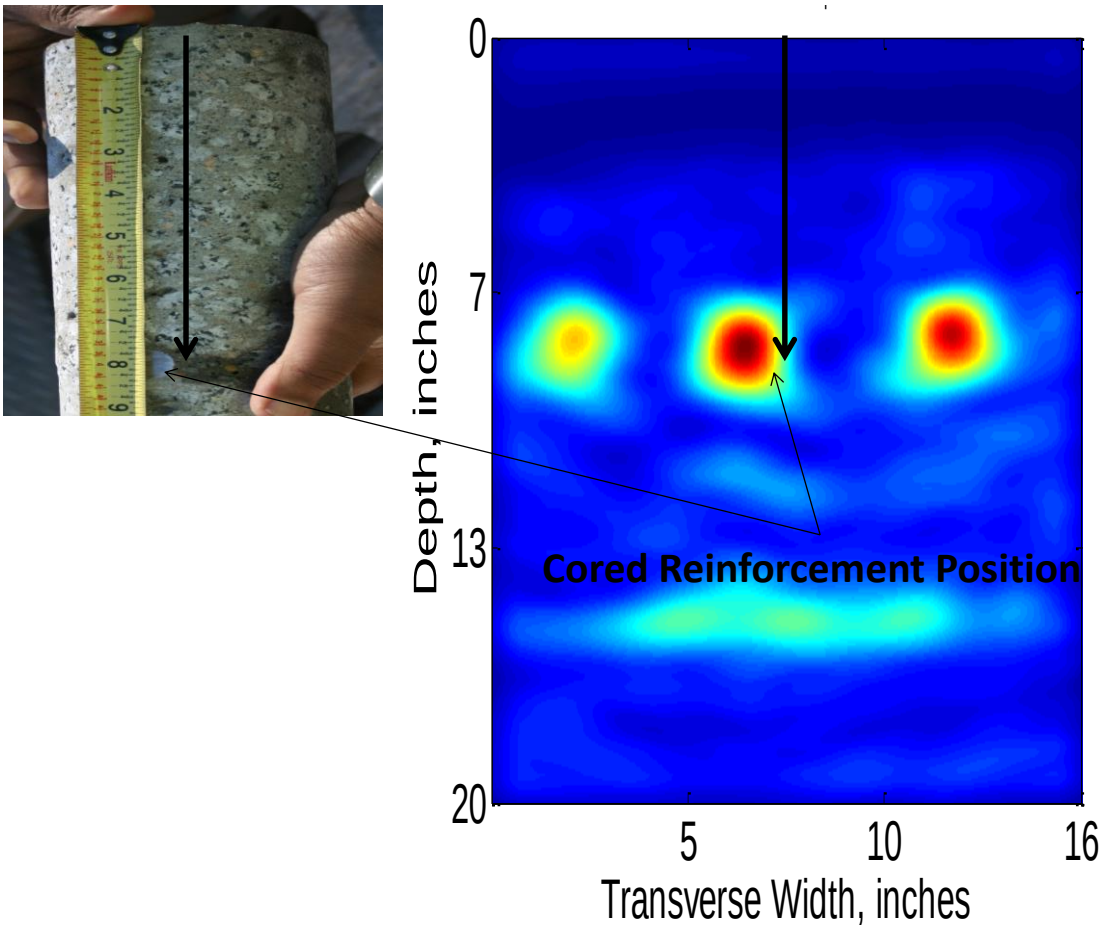

Figure 3-9. Forensic verification of the focused reinforcement location within the SAFT-IA B-scan.

3.1.3 SAFT-3D

Three-dimensional reconstruction of subsurface characteristics can simplify interpretation of multiple ultrasonic array scans. SAFT 3-dimensional reconstructions (SAFT-3D) can be achieved using various interpolation and filtering techniques. Figure 3.10 shows the SAFT-IA B-scan from figure 3.9 as well as ten additional measurements at 50 mm step sizes in the longitudinal direction.

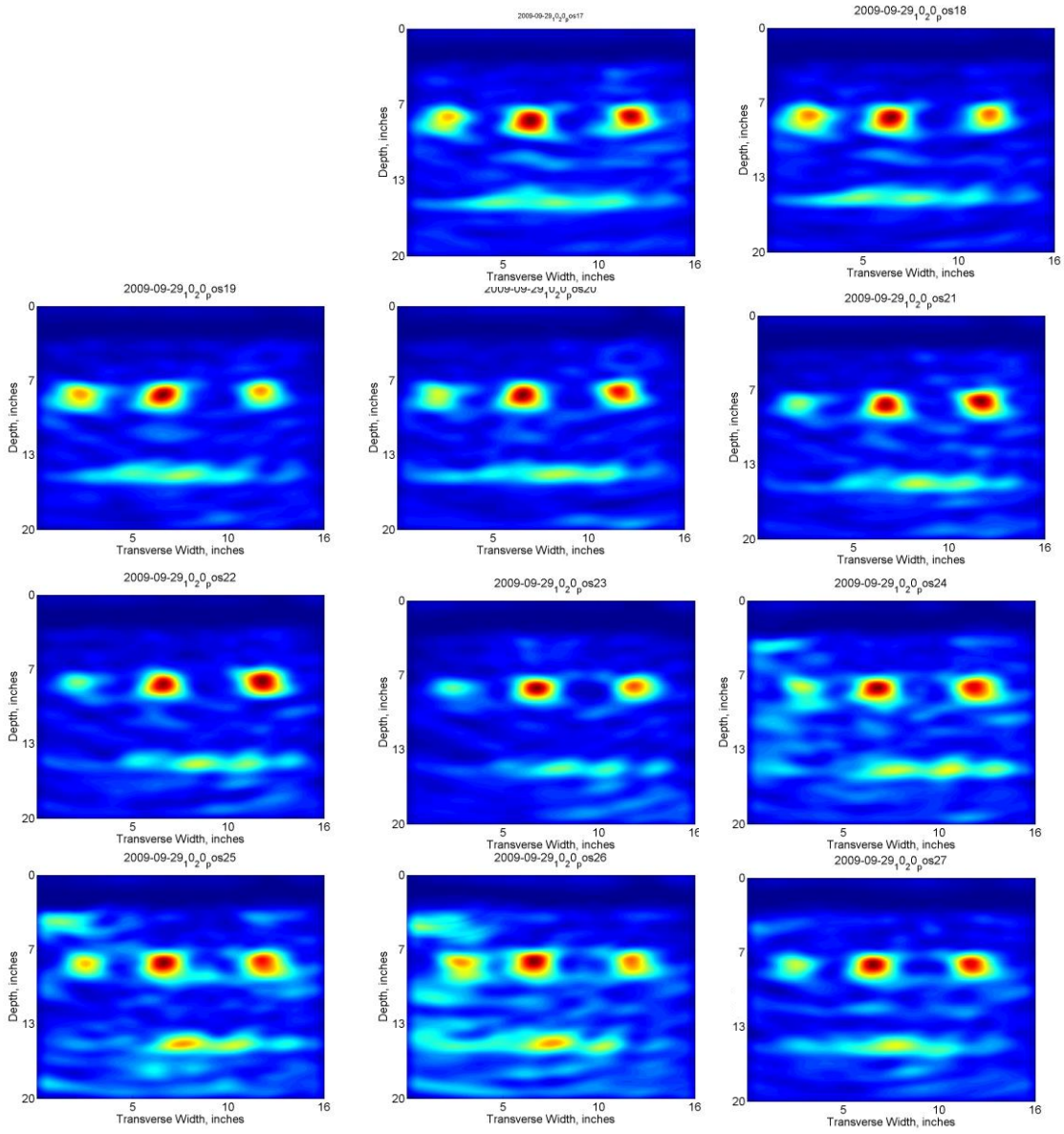

Figure 3-10. SAFT-IA B-scans from the cored location as well as 10 subsequent scans in the longitudinal direction.

These scans were used to create the remaining length of the cored reinforcement as well as the reinforcement to the right of the cored reinforcement in a three-dimensional reconstruction (SAFT-3D). Figure 3.11 shows a schematic of the SAFT-3D reconstruction process where scans are taken in step sizes in the longitudinal direction and interpolation techniques are used to create the continuous 3D image of the ROI. The process of creating the SAFT-3D reconstruction included selecting an optimal threshold,

using the same 'disk' filtering function for each SAFT-IA B-scan, a MATLAB™ 3D matrix smoothing function ('smooth3'), and a MATLAB™ interpolation function ('isosurface') within the volume of the reconstruction (Matlab Guide, 1998).

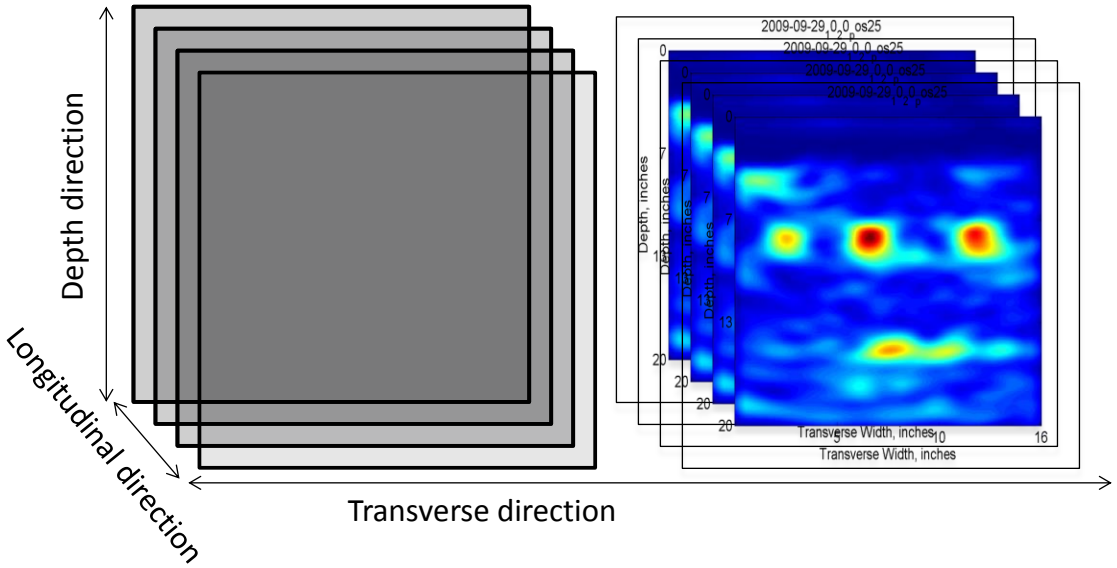

Figure 3-11. Schematic representation of the process of creating SAFT-3D reconstructions.

The SAFT-3D reconstruction of 300 mm of depth within the concrete layer of a 500 mm longitudinal (850 mm to 1350 mm) by 400 mm transverse location is given in figure 3.12. The reinforcement on the left side at 850 mm in the longitudinal direction corresponds to the cored location. This type of SAFT 3D reconstruction can be useful for getting relational information about the high intensity reflections to determine if the reflection is caused by an as designed inclusion or damaged concrete.

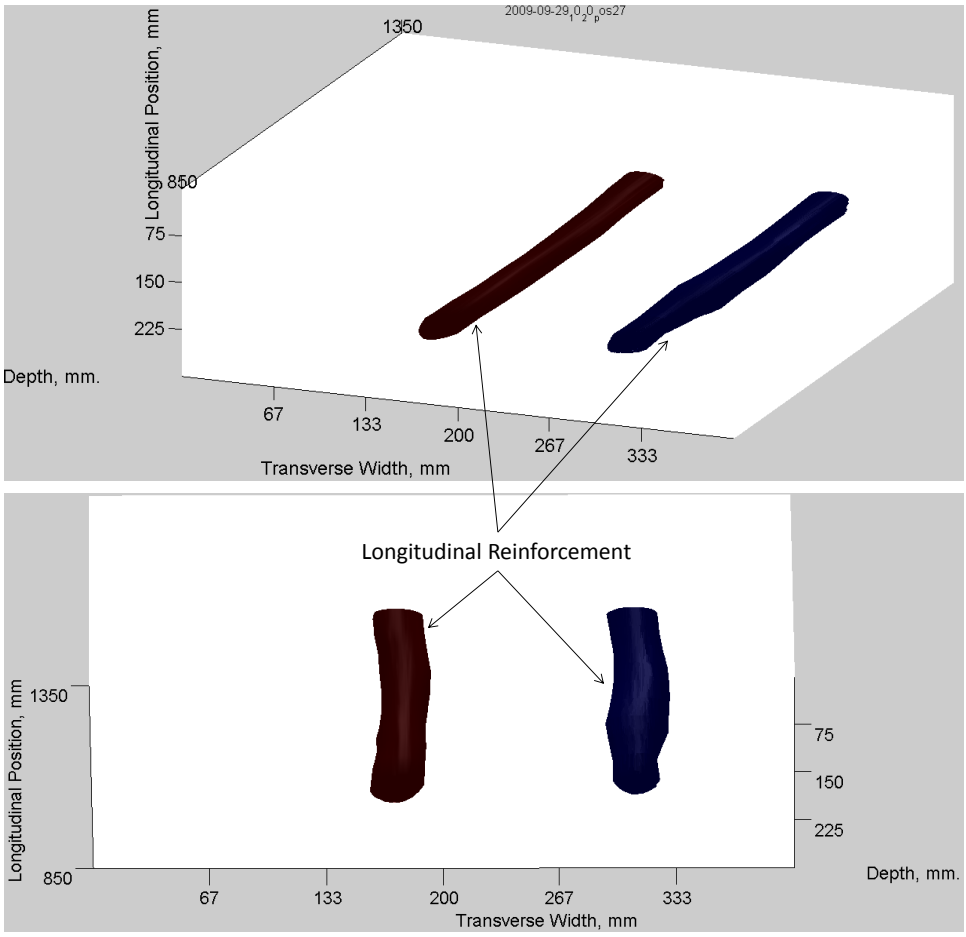

Figure 3-12. SAFT 3D reconstruction using the SAFT-IA B-scan reconstructions shown in Figure 3.10.

3.1.4 SAFT Panoramic

While the SAFT and SAFT-IA B-scans are useful for diagnostics of various problems, there are limitations to the use of SAFT B-scans in analysis of some important practical problems. Often the desired ROI is larger than the resulting SAFT B-scan reconstruction from a single set of measurements within the self-contained array allows. As explained by Shouki et al. (2011, 2012), the limited aperture can create situations where "measurements may be inconclusive if the array is located directly above an edge of a defect." To increase the effective aperture and add more redundancy in the measurements, the following procedure was developed to create large panoramic cross sections with increased resolution.

Each SAFT-IA B-scan, $\widehat{\boldsymbol{O}}_{k,i}^{m}$ is converted to the dimensions of the larger region of interest, ROI_{PAN}, where m is an index of the current SAFT-IA B-scan. The vertical dimensions of the new ROI_{PAN} and ROI of each SAFT-IA B-scan $\widehat{\boldsymbol{O}}_{k,i}^{m}$ are the same while the horizontal dimensions are increased. Let the leftmost (lowest) horizontal coordinates of the m-th SAFT-IA B-scan, x_1, correspond to the x_{i^*} coordinate within the panoramic reconstruction. In this case all intensity values of the original SAFT-IA B-scan within the new ROI_{PAN} are placed according to their physical location with zeros padding any location where no intensity value applies. Each padded SAFT B-scan, $\widehat{\boldsymbol{O}}_{k,i}^{PAN,m}$, is created according to the following relationship for all $\widehat{\boldsymbol{O}}_{k,i}^{m}$ horizontal positions within the ROI_{PAN}:

$$\widehat{\boldsymbol{O}}_{k,i}^{PAN,m} = \widehat{\boldsymbol{O}}_{k,i-i^*+1}^{m} \; for \; i^* \leq i \leq i^* + W - 1$$

$$\widehat{\boldsymbol{O}}_{k,i}^{PAN,m} = 0 \; for \; i < i^* \; or \; i \geq i^* + W \qquad [3.14]$$

Equation 3.15 shows the matrix representation of an example panoramic form, $\left[\widehat{\boldsymbol{O}}\right]^{PAN,m}$, of the m-th applied SAFT-IA B-scan.

$$\left[\widehat{\boldsymbol{O}}\right]^{PAN,m} = \begin{array}{|c|c|c|c|c|c|c|} \hline \mathbf{0} & \mathbf{0} & \widehat{\boldsymbol{o}}_{i^*,1}^{PAN,M} & \cdots & \widehat{\boldsymbol{o}}_{i^*+W-1,1}^{PAN,M} & \mathbf{0} & \mathbf{0} \\ \hline \mathbf{0} & \mathbf{0} & \cdots & \widehat{\boldsymbol{o}}_{i,k}^{PAN,M} & \cdots & \mathbf{0} & \mathbf{0} \\ \hline \mathbf{0} & \mathbf{0} & \cdots & \cdots & \cdots & \mathbf{0} & \mathbf{0} \\ \hline \mathbf{0} & \mathbf{0} & \widehat{\boldsymbol{o}}_{i^*,D}^{PAN,M} & \cdots & \widehat{\boldsymbol{o}}_{W,D}^{PAN,M} & \mathbf{0} & \mathbf{0} \\ \hline \end{array} \qquad [3.15]$$

After this procedure the individual scans can be combined into a single panoramic representation, SAFT-Pan, using the following rule:

$$\widehat{\boldsymbol{O}}_{k,i}^{PAN} = \max_{m}\left(\widehat{\boldsymbol{O}}_{k,i}^{EPAN,m}\right) \; for \; all \; k \; and \; i \; in \; the \; ROI_{PAN}$$

Where $\left[\widehat{\boldsymbol{O}}\right]^{PAN}$ is the matrix form of the SAFT-Pan.

To illustrate the use of the SAFT-IA Panoramic method (SAFT-Pan), a series of scans at a PCC joint with embedded dowels is presented. The SAFT-Pan reconstructions show high levels of reflection intensity at lateral and depth locations where there is a change in acoustic impedance such as a dowel inclusion or at the interface between the concrete and base material. Figure 3.13 shows nine SAFT-IA B-scans each centred approximately 5 in. from a transverse joint with 12 in. thickness and 1.5 in. diameter dowels inserted at the mid-depth of the pavement. It can be observed that round high intensity reflections (red) are located at about half the depth of the more oblong high intensity reflection (red) at a greater depth. The round reflections indicate the lateral location and depth of the dowels while the oblong reflection indicates the depth of the PCC pavement layer. It can be observed that locations other than the doweled locations or PCC depth have a low intensity of reflection indicating low reflectivity (sound) surrounding concrete.

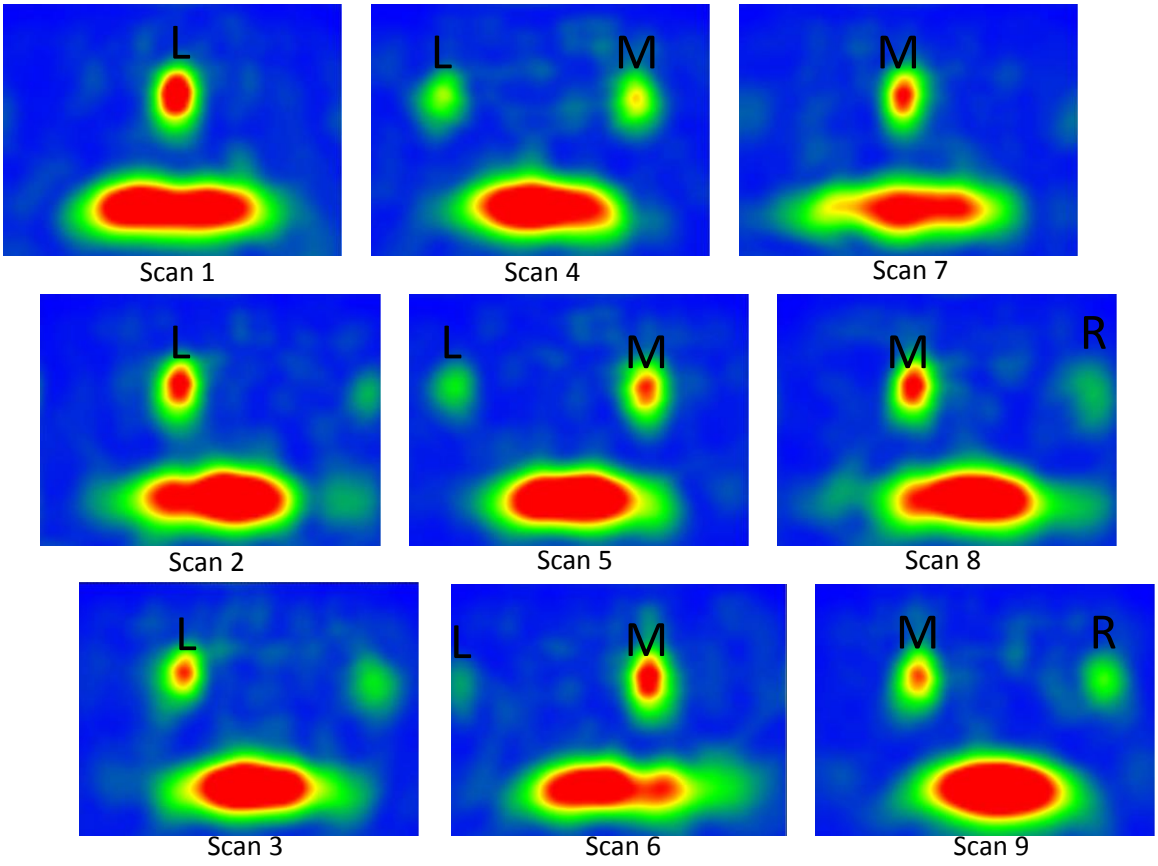

Figure 3-13. Example set of 9 overlapping SAFT-IA B-scans used to create a SAFT Panoramic.

Figure 3.14 shows the SAFT-Pan reconstruction resulting from the 9 overlapping SAFT-IA B-scans taken in 2 inch step sizes after they have been fused together. The resulting panoramic tomography indicates the subsurface condition of a 3 ft wide section of the pavement. Analysis of figure 3.14 indicates an low reflectivity (relatively sound) condition where the only high intensity of reflection occurs due to features that were as designed including the slightly less than 1 ft concrete depth reflection and circular reflections at the depth and lateral location of the dowels. The lack of reflection (blue) at the remaining locations indicates undamaged concrete. This illustrates that SAFT-Pan reconstructions can create a clearer picture of inclusions and their relative positions than individual SAFT-IA reconstructions. SAFT-Pan reconstructions can be used to create SAFT-3D Reconstructions using the same process described in section 3.1.3.

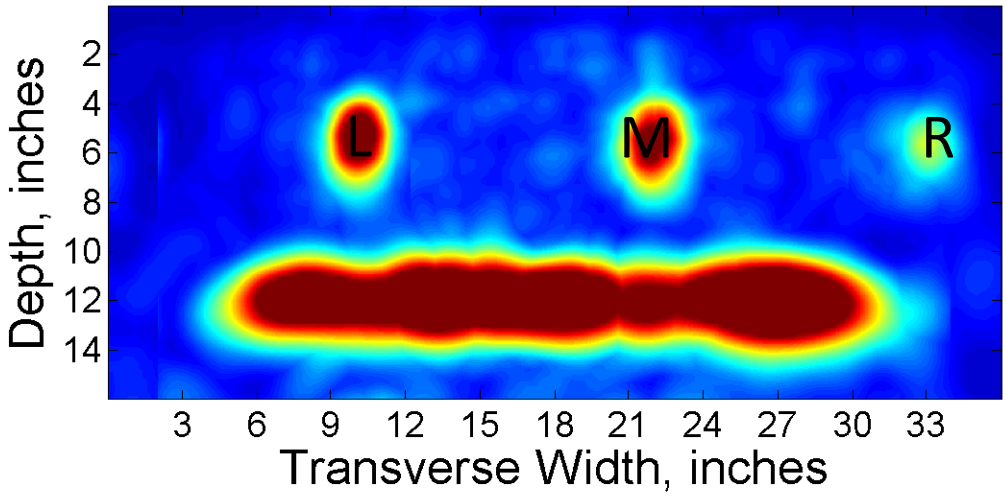

Figure 3-14. Five SAFT-Pan examples at a PCC joint.

3.2 Automated Data Interpretation for Concrete Pavements

While the Kirchoff-migration based SAFT reflectivity reconstructions discussed in section 3.1 create an intuitive focused image of subsurface reflectivity in pavements, qualitative analysis methods require expertise and can be time consuming. Quantitative

methods can be useful to create automated analysis of specific pavement-related problems to increase productivity while often improving the accuracy and reliability of the interpretation.

3.2.1 Direct Reflection Automation

The method used for direct reflection quantification should be capable of identifying the characteristics of the object of interest (e.g. reinforcement location, pavement thickness interface, delamination, etc.). This can be done with the following general algorithm:

- Run the applicable SAFT analysis described in section 3.1 to estimate the reflectivity function of the region
- Identify threshold value that will separate high intensity of reflection areas from low intensity of reflection areas
- Identify characteristics of the type of reflection caused by the specific object of interest
- Use shape recognition schemes to decide if the identified areas are in fact the object of interest based on the identified characteristics
- Determine the location (depth and lateral position) of the center of the object of interest
- Eliminate false positives through a check with one or multiple adjacent scans
- Output the results to a spreadsheet along with information about the scan locations

The general outline given above was used to develop an algorithm capable of finding depth of reinforcements or any round inclusion in concrete pavements. Figure 3.15 shows the steps (left top to bottom, then right top to bottom) in identifying 2 longitudinal rebars in an example SAFT B-scan similar to the example described in section 3.1. The figure illustrates the use of circularity criteria to identify longitudinal rebar reflections. After a threshold value of 0.80 of the maximum intensity is applied, the two central reflections are identified as reinforcement, while the left and right reflections are rejected because their characteristics could not be determined reliably. Thus, in this case, the

concrete cover for the identified center two reflections would be output to the spreadsheet.

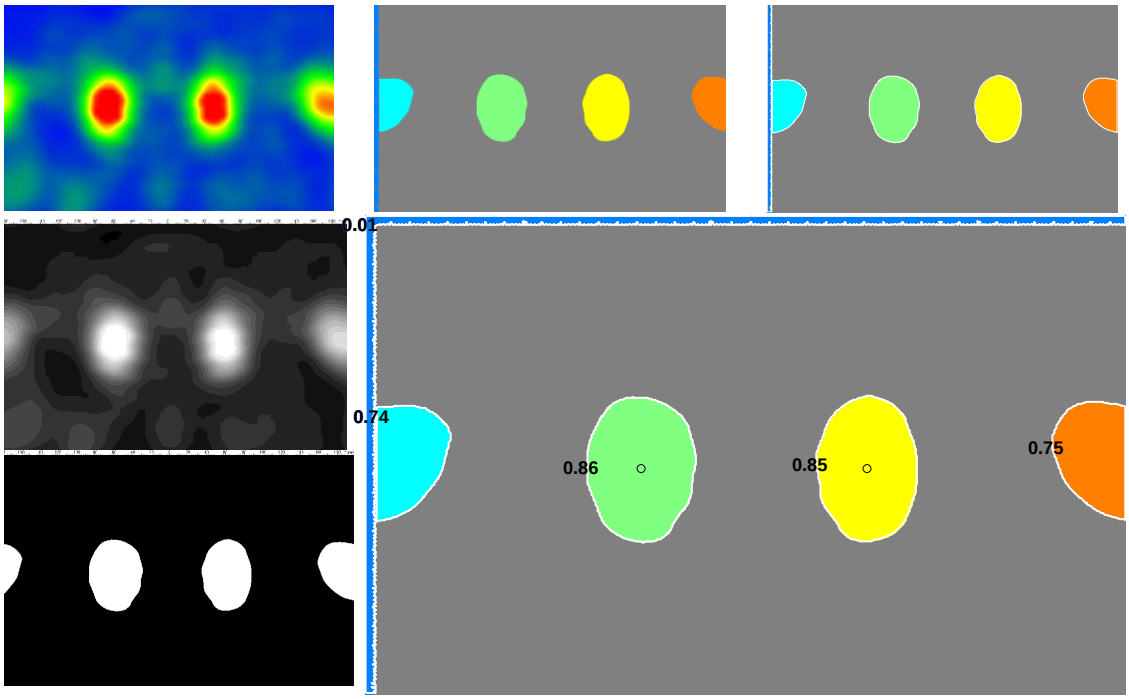

Figure 3-15. Progression in identifying the centroid of reflections caused by round inclusions.

The same general procedure was used to develop an algorithm for automated layer boundary depth detection. In this case the depth of the reflecting interface was determined by choosing the highest average reflectivity of the rows in the reconstruction. The horizontal portion to be included within each row can be predefined based on the characteristics of the layer boundary.

3.2.2 Flaw Detection

As discussed in section 3.2.1, identification of inclusions and layer boundaries in concrete from SAFT reconstructions can be automated using shape recognition and absolute maxima techniques. These methods were feasible because the geometry of the area of interest was known within each scan and in relation to adjacent scans. However, flaws in concrete such as improper concrete consolidation are generally non-uniform and

a priori knowledge of the reflector type and dimension is not available. Automated detection of these types of defects, which are stochastic in nature, requires a method that does not rely on shape recognition.

To accomplish this task, the impact-echo signature analysis (IESA) method (Shubert et al., 2001) described in section 2.4.4, was modified for the reconstruction methods used in this study. While Schubert and Koehler stated that *a priori* knowledge of a reference signal where no scatterers are present is not generally available, the Kirchoff migration methods described in section 3.1 in this thesis provide intuitive reference scans. It is proposed to generalize the IESA method for use with SAFT reconstructions that are obtained from the ultrasonic linear array or other tomography reconstructions. This can be accomplished by generalizing the IESA into a two dimensional ultrasonic tomography signature analysis method (2D-UTSA or UTSA). Pearson's correlation coefficient is adapted for comparison of reconstructed intensity matrices as follows using the SAFT-IA B-scan variables introduced in section 3.1.2:

$$C^{IA,m} = \frac{Cov\left[[\hat{\boldsymbol{o}}]^{IA,ref},[\hat{\boldsymbol{o}}]^{IA,m}\right]}{\sqrt{Var\left[[\hat{\boldsymbol{o}}]^{IA,ref}\right]Var\left[[\hat{\boldsymbol{o}}]^{IA,m}\right]}} = \frac{\sum_{i=1}^{W}\sum_{k=1}^{D}\left(\hat{\boldsymbol{o}}_{i,k}^{IA,ref}-\hat{\boldsymbol{o}}_{mean}^{IA,ref}\right)\left(\hat{\boldsymbol{o}}_{i,k}^{IA,m}-\hat{\boldsymbol{o}}_{mean}^{IA,m}\right)}{\sum_{i=1}^{W}\sum_{k=1}^{D}\left(\hat{\boldsymbol{o}}_{i,k}^{IA,ref}-\hat{\boldsymbol{o}}_{mean}^{IA,ref}\right)^{2}\sum_{i=1}^{W}\sum_{k=1}^{D}\left(\hat{\boldsymbol{o}}_{i,k}^{IA}-\hat{\boldsymbol{o}}_{mean}^{IA}\right)^{2}} \quad [3.16]$$

where $\left[\hat{\boldsymbol{O}}\right]^{IAref}$ and $\left[\hat{\boldsymbol{O}}\right]^{IA,m}$ are the matrices of reflection intensity for the reference SAFT-IA B-scan and m-th SAFT-IA B-scan, respectively; $\hat{\boldsymbol{o}}_{i,k}^{IA,ref}$ and $\hat{\boldsymbol{o}}_{i,k}^{IA}$ are the single intensity values of the reference signal and m-th reconstruction, respectively, with depth below the measurement location increasing with k and the location along the horizontal direction of the scan increasing with i; $\hat{\boldsymbol{o}}_{mean}^{IA,ref}$ and $\hat{\boldsymbol{o}}_{mean}^{IA}$ are the mean intensities of the reference scan and m-th scan, respectively; W and D are the number of width and depth intensity values in the depth and device aperture direction, respectively; and $C^{IA,m}$ is Pearson's correlation coefficient, which measures the strength of the linear dependence between $\left[\hat{\boldsymbol{O}}\right]^{IAref}$ and $\left[\hat{\boldsymbol{O}}\right]^{IA,m}$.

Thus, if a SAFT-IA B-scan taken on relatively sound concrete with similar structural geometry is used as the reference scan, flawed concrete locations can be identified. On the extremes, a $C^{IA,m}$ value of 0 would indicate no correlation and a $C^{IA,m}$ value of 1 would indicate that the two SAFT-IA B-scans are related linearly. Therefore, a higher $C^{IA,m}$ would indicate that the m-th SAFF-IA B-scan was taken on sound concrete, and a significant decrease in the correlation coefficient would indicate non-uniform SAFT-IA B-scans, or flawed concrete, especially if observed in a group of adjacent scans. This type of analysis will be referred to as the 2D-UTSA method.

In addition to making the method applicable for the type of data gathered by the study, the use of the expanded Pearson's correlation for 2D comparison improves the method by correcting the issues of the IESA technique in selecting the reference signal. As explained in section 3.1.2 the SAFT-IA reconstruction creates a relatively intuitive reconstructed image of the ROI reflectivity function. Therefore, selection of a damage free reference scans is possible based on past experience with signal interpretation of SAFT reconstructions (Hoegh and Khazanovich, 2011; Hoegh et al., 2012a; Hoegh et al., 2012b) and the misinterpretations associated with the IESA method can be mitigated. When necessary, coring should be conducted to verify that the reference scan is indeed damage free.

Furthermore, subsurface damage in concrete is generally entropic in that there is little variation between SAFT-IA B-scans of concrete in relatively good condition at different locations if the same instrument settings are used, while there is a significant variation between scans where flaws are present at different locations (Lin et al., 2011). Therefore, sound concrete will have similar levels of correlation with the reference SAFT-IA B-scan, whereas the correlation of scans with flaws at different locations will fluctuate. Therefore, a procedure where the reference scan is taken as the average of all of the SAFT-IA B-scans in the set is introduced. It is expected that sound concrete may not necessarily have as high of a correlation with the generated reference scan as is the case for a manually selected reference scan. However, if a significant portion of measurements are made on sound concrete, the sound concrete locations should result in

similar correlation values, while unsound concrete will result in lower values due to the randomness of flaws. Thus, decreases are still present in the correlogram even when the reference scan includes contributions from the flawed concrete locations. As will be discussed in Chapter 4, this method is not overly sensitive to selection of the reference scan, and can be generally applied to locate areas of flawed concrete.

3.2.3 SAFT Panoramic-Enhanced

While SAFT-Panoramic analysis is useful for many applications, there are some situations where the physical location of each SAFT-IA B-scan is not known to the desired accuracy of the reconstruction. In this case, the SAFT-Pan procedure described in section 3.1.4 can introduce significant error. Figure 3.16 shows an example of a SAFT-Pan reconstruction which combines nine individual SAFT-IA reconstructions. The target step size of 2 in. is used in SAFT-Pan development which resulted in a blurred reflectivity in the region of the center dowel due to imprecise step size inputs.

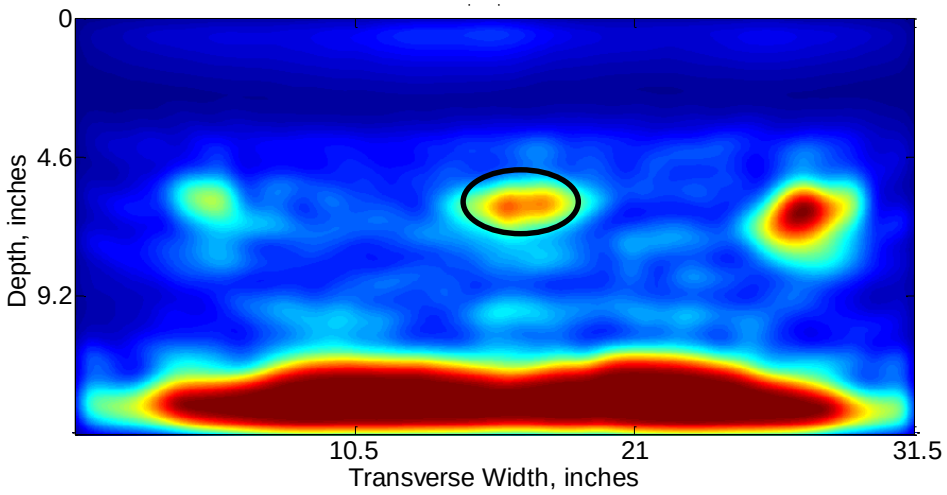

Figure 3-16. SAFT-Pan reconstruction with imprecise step size input.

To address this problem, an iterative procedure for enhanced panoramic reconstruction was developed. First, each SAFT-IA B-scan is numbered according to increasing coordinate in the horizontal direction. Then, the individual SAFT-IA B-scans are added sequentially. The procedure is based on the concept that the same position within the

region of interest should result in similar relative reflectivity, regardless of the location of the scan, assuming the effect of limited aperture is taken into account.

Denote $\left[\widehat{\boldsymbol{O}}\right]^{EPAN,m}$ as the panoramic reconstruction after the m-th SAFT-IA B-scan, $\left[\widehat{\boldsymbol{O}}\right]^{IA,m}$, is added and $W^{EPAN,m}$ is the number of columns. Naturally, $\left[\widehat{\boldsymbol{O}}\right]^{EPAN,1} = \left[\widehat{\boldsymbol{O}}\right]^{IA,1}$ and $W^{EPAN,1} = W$ where, as defined earlier, W is the number of columns in the individual SAFT-IA B-scan reconstructions. Unlike section 3.1.4, the exact difference in positions of adjacent positions, ΔS, is not known, but is assumed to be within a certain range defined by equation 3.17:

$$\iota_1 \Delta x \leq \Delta S \leq \iota_2 \Delta x \qquad [3.17]$$

where ι_1 and ι_2 are integers and Δx is the difference in horizontal position between two adjacent columns in the reconstruction. This means that the difference in adjacent positions can be expressed in terms of number of additional columns, ι. For each ι within the range $[\iota_1, \iota_2]$ a similarity between portions of the overlapping regions within $\left[\widehat{\boldsymbol{O}}\right]^{EPAN,m}$ and $\left[\widehat{\boldsymbol{O}}\right]^{IA,m+1}$ is determined. To account for the effect of limited aperture, the first W_1 columns of $\left[\widehat{\boldsymbol{O}}\right]^{IA,m+1}$ and last W_1 columns of $\left[\widehat{\boldsymbol{O}}\right]^{EPAN,m}$ are not considered in determining similarity. In many cases, the stability of the process is improved if only a portion of the reconstruction in the vertical direction$[\ D_1, D_2]$ is included in the comparison. Figure 3.17 illustrates the process of determining overlapping regions used in the similarity analysis.

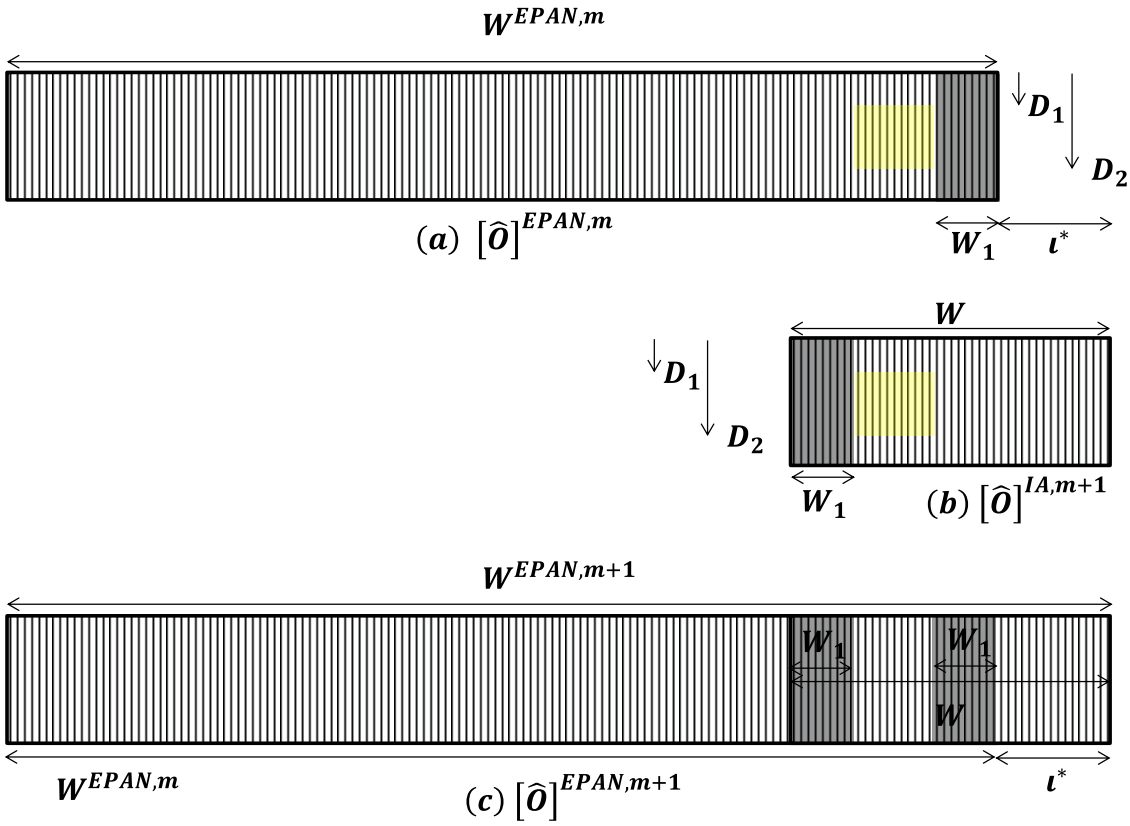

Figure 3-17. Determination of overlapping regions between the reconstructions and determination of the next panoramic reconstruction

The degree of similarity of the overlapping regions, $H(\iota)$, is determined based on Pearson's Correlation as follows:

$$H(\iota) = \frac{\sum_{i=W_1+1}^{W-W_1-\iota}\sum_{k=D_1}^{D_2}\left(\hat{o}^{EPAN,m}_{W^{EPAN,m}-W+\iota+i,k}-\hat{o}^{EPAN,m}_{mean}\right)\left(\hat{o}^{m+1}_{i,k}-\hat{o}^{m+1}_{mean}\right)}{\sum_{i=W_1+1}^{W-W_1-\iota}\sum_{k=D_1}^{D_2}\left(\hat{o}^{EPAN,m}_{W^{EPAN,m}-W+\iota+i,k}-\hat{o}^{EPAN,m}_{mean}\right)^2\sum_{i=W_1+1}^{W-W_1-\iota}\sum_{k=D_1}^{D_2}\left(\hat{o}^{m+1}_{i,k}-\hat{o}^{m+1}_{mean}\right)^2} \quad [3.18]$$

Where

$$\hat{o}^{EPAN,m}_{mean} = \frac{\sum_{i=W^{EPAN,m}-W+\iota+W_1+1}^{W^{EPAN,m}-W_1}\sum_{k=D_1}^{D_2}\hat{o}^{EPAN,m}_{i,k}}{(W-2W_1-\iota)(D_2-D_1+1)}$$

$$\hat{o}^{m+1}_{mean} = \frac{\sum_{i=W_1+1}^{W-W_1-\iota}\sum_{k=D_1}^{D_2}\hat{o}^{m+1}_{i,k}}{(W-2W_1-\iota)(D_2-D_1+1)}$$

The ι that results in the maximum value of function $H(\iota)$ on the interval $[\iota_1, \iota_2]$ is denoted as the optimal shift factor, ι^*. Then the next SAFT-EPAN reconstruction, $\left[\hat{O}\right]^{EPAN,m+1}$, is defined as follows:

$$\widehat{\boldsymbol{O}}_{i,k}^{EPAN,m+1} = \widehat{\boldsymbol{O}}_{i,k}^{EPAN,m} \; for \; i < W^{EPAN,m} - W + \iota^* + W_1 \qquad [3.19]$$

$$\widehat{\boldsymbol{O}}_{i,k}^{EPAN,m+1} = max\left(\widehat{\boldsymbol{O}}_{i,k}^{EPAN,m}, \widehat{\boldsymbol{O}}_{i-W^{EPAN,m}+W-\iota^*,k}^{m+1}\right)$$

for $W^{EPAN,m} - W + \iota^* + W_1 \leq i \leq W^{EPAN,m}$

and

$$\widehat{\boldsymbol{O}}_{i,k}^{EPAN,m+1} = \widehat{\boldsymbol{O}}_{i-W^{EPAN,m}+W-\iota^*,k}^{m+1}$$

for $W^{EPAN,m} < i \leq W^{EPAN,m+1}$

where, $W^{EPAN,m+1}$ is the width of the new SAFT-EPAN as defined:

$$W^{EPAN,m+1} = W^{EPAN,m} + \iota^*$$

Each subsequent SAFT panoramic reconstruction, $\left[\widehat{\boldsymbol{O}}\right]^{EPAN,m+1}$, is obtained from addition of $\left[\widehat{\boldsymbol{O}}\right]^{EPAN,m}$ and the next SAFT-IA B-scan, $\left[\widehat{\boldsymbol{O}}\right]^{IA,m+1}$. The additional number of columns in the new reconstruction, ι^*, is determined by comparing the similarity between portions of the overlapping regions within $\left[\widehat{\boldsymbol{O}}\right]^{EPAN,m}$ and $\left[\widehat{\boldsymbol{O}}\right]^{IA,m+1}$. The additional columns, ι^*, are chosen from within the range of potential shift factors $[\iota_1, \iota_2]$.

Figure 3.18 illustrates the similarity of overlapping scans as a function of possible shift factors, $H(\iota)$, used for fusing of the nine scans from this example. The plot is given on an x-axis scale where columns are converted to inches and the target shift factor of 2 in. is marked by the black vertical line. The column range, $[\iota_1, \iota_2]$ used for determination of the optimal shift factor, ι^*, is equivalent to a range of 1.4 inches to 2.6 inches. It can be observed that the optimal step sizes, as determined by the ι resulting in the peak of the $H(\iota)$ curves, are significantly different than the target shift factor at various locations. Smaller than target shift factors, ι^*, were used for placement of $m = 2,4,6,8$ SAFT-IA

scans, $[\widehat{\boldsymbol{O}}]^{IA,m}$, while larger than target shift factors, ι^*, were used for placement of $m = 3,5,7,9$ SAFT-IA scans, $[\widehat{\boldsymbol{O}}]^{IA,m}$ into each iterative formulation of the SAFT-Epan, $[\widehat{\boldsymbol{O}}]^{EPAN,m}$.

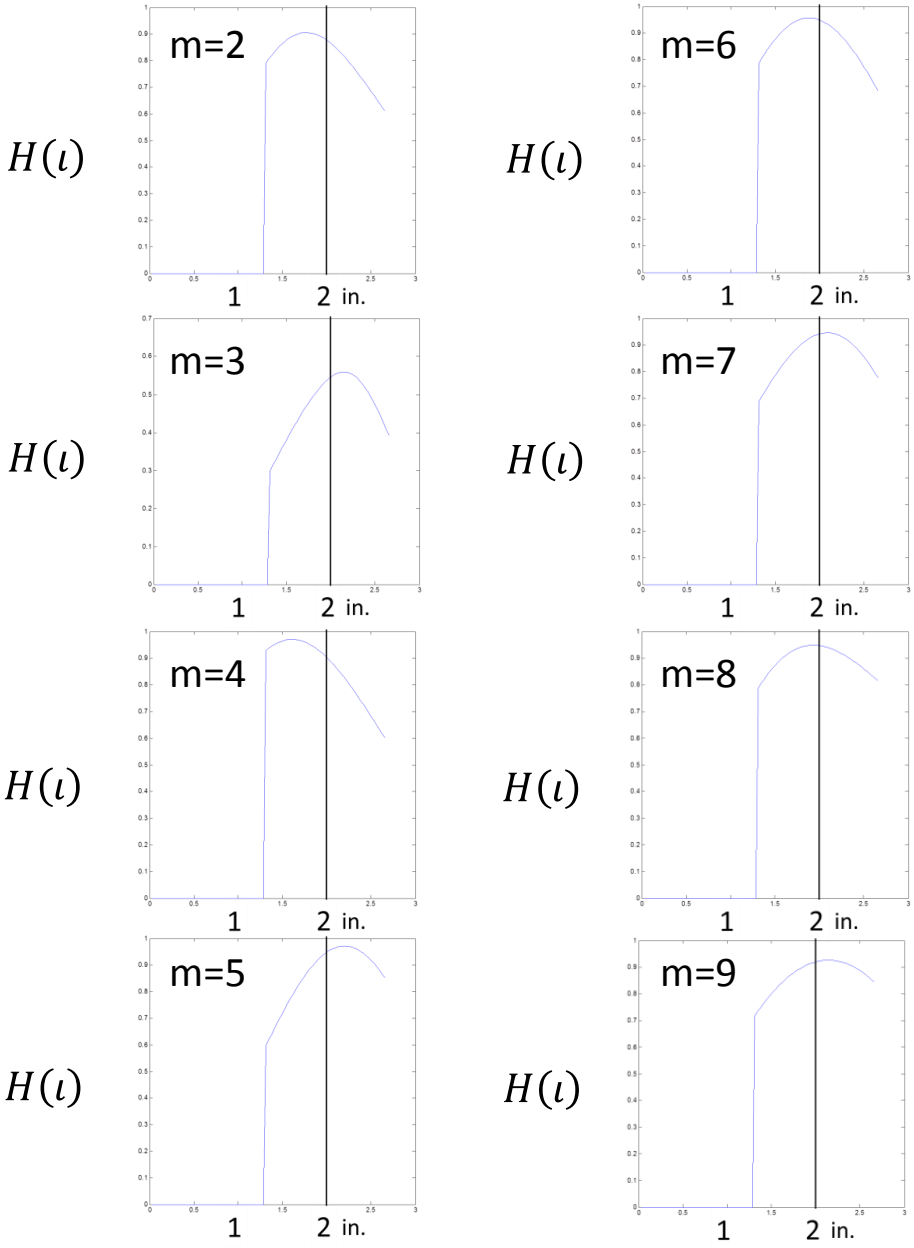

Figure 3-18. Similarity of overlapping region curves used for placement of SAFT-IA reconstructions into the SAFT-EPan reconstruction.

Figure 3.19 shows the (a) original SAFT-Pan reconstruction and (b) SAFT-EPan reconstruction both obtained from the same nine individual SAFT-IA scans in this example. It can be observed that the blurry oblong reflection at the center dowel in the SAFT-Pan is a more focused circular reflection when using the SAFT-EPan reconstruction. Correcting for some of the uncertainty in the measurement process by placing the scans based on similarity of overlapping regions allows for a more focused reconstruction that is consistent with the reflectivity in the region.

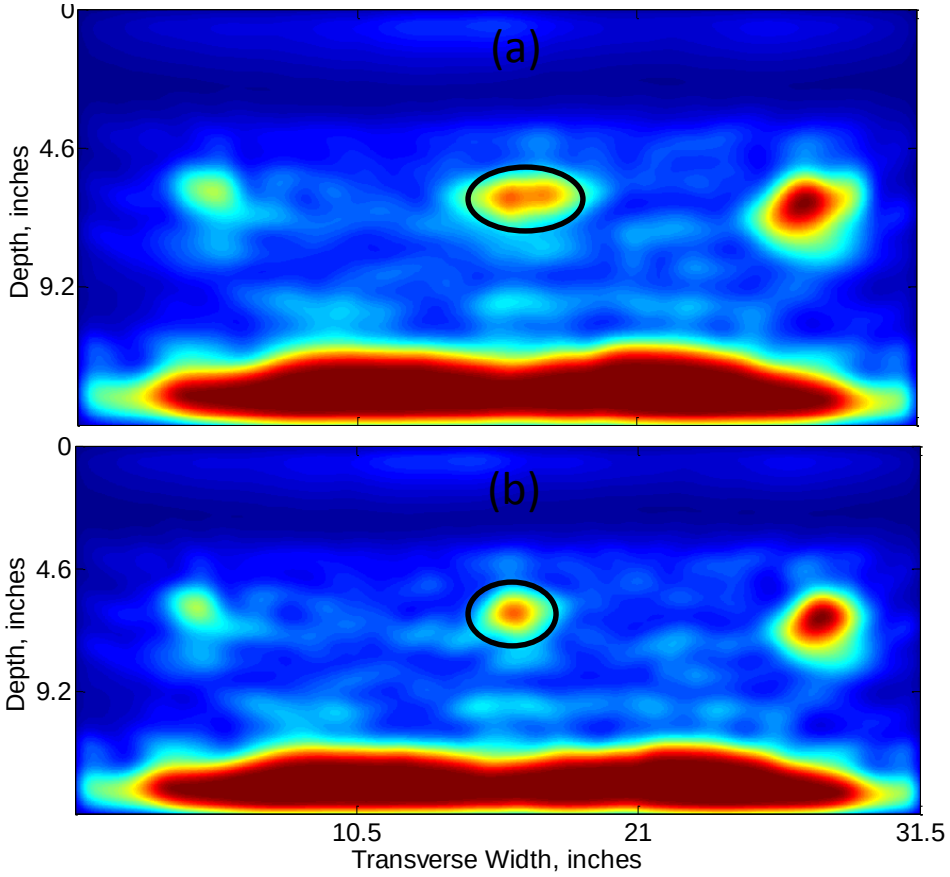

Figure 3-19. Reconstruction of 9 overlapping scans over 3 dowels to create (a) SAFT-Pan and (b) SAFT-EPan reconstructions.

4 Validation of Signal Processing Techniques

The reconstruction and automated analysis techniques developed as a part of this thesis were validated with a variety of laboratory and in-situ testing measurements. In these cases, ground truth comparison was available for validation of the various techniques.

4.1 SAFT – Instantaneous Amplitude

As explained in detail in section 3.1 of Chapter 3, Kirchoff migration was generalized for focusing of sending and receiving pairs at spatially diverse locations. This allowed for reconstruction of the relative reflectivity amplitude within the region of interest (ROI) using the 45 impulse time-histories from each ultrasonic linear array scan at various incident angles using the instantaneous amplitude-based synthetic aperture focusing technique (SAFT-IA). The accuracy of the assumptions and reconstruction concepts were validated for various concrete pavement nondestructive evaluation needs.

4.1.1 PCC Slab Thickness

Concrete pavement slabs are often placed on an un-bonded granular base that has significantly lower acoustic impedance than the concrete layer. Identification of the PCC slab thickness using ultrasonic linear array scans involves determination of the highest reflectivity row, and corresponding physical depth, within the reconstructed image. The simple geometry of this structure does not require precise focusing capability of the reconstruction algorithm. However, the accuracy highly depends on the accuracy of the parameter determination such as pulse velocity, C_S, and shift factor, t^{shift} which were introduced in section 2.4.3. The top layer thickness for various laboratory and field testing locations were used for validation of these parameters.

As explained in Chapters 2 and 3, the shift factor and velocity calculations for each of the reconstruction procedures were based on the objective of matching the highest amplitude of the pulse to the highest reflectivity locations in the ROI. Thus, verification of the automated layer boundary depth detection consisted of comparing the depth of the

highest reflectivity within the SAFT-IA reconstruction with the interface between the PCC layer and the underlying base (highest change in acoustic impedance in the subsurface structure). These locations correspond to the SAFT-IA measured PCC thickness and forensic measured PCC thickness, respectively. Figure 4.1 shows a comparison of thickness measurements from various locations such as the Minnesota Road Research Facility (MnROAD), the National Airport Testing Facility (NAPTF), Engineering Research and Development Center (ERDC) facility in Vicksburg, MS, as well as various in service pavements using the automated layer boundary depth as compared to the core measurements in the same location. It can be observed that there is a very good agreement between the ultrasonic linear array (MIRA) SAFT-IA reconstruction measured thickness and forensic (core) measured thickness ($R^2 = .997, slope = 0.988$). These comparisons of the PCC layer thickness detection with ground truth data validate the calculation procedures for reconstruction parameters such as velocity and shift factor.

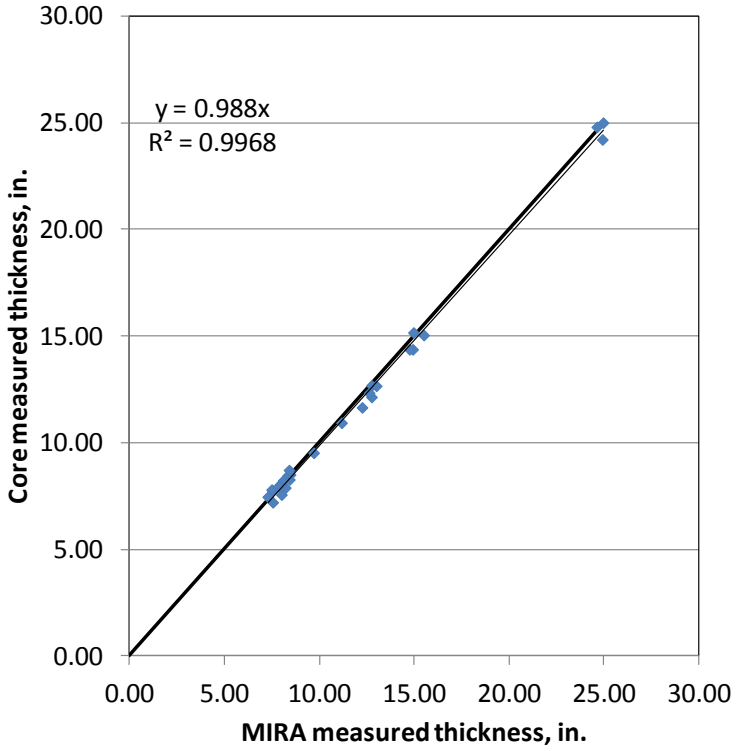

Figure 4-1. Comparison of the core measured thickness versus the automated layer boundary depth measurements.

Figure 4.2 shows undulations of pavement thickness of a newly constructed highway pavement as detected using the automated layer boundary algorithm (blue) along with the core measured thickness at the typical MnDOT specified thickness quality assurance distances. It can be observed that many of the locations where the pavement thickness was significantly above or below the nominal 9 in. thickness were not captured using the limited amount of data that coring provides. Therefore the simple automated thickness procedure can provide valuable additional information for quality assurance and design of concrete pavements.

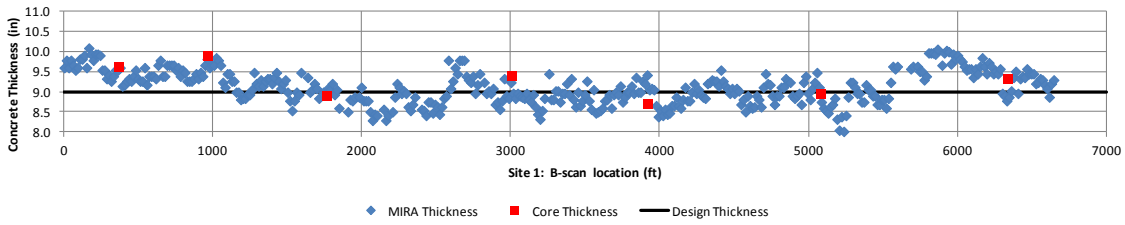

Figure 4-2. Automated thickness measurements showing undulations of the pavement thickness (blue) along with core thickness measurements of a newly constructed pavement.

4.1.2 Reinforcement Location

The depth and lateral location of strong reflections within the PCC layer can be evaluated using the various SAFT analysis methods described in Chapter 3 to determine the location of reinforcements. Figure 4.3 shows ultrasonic linear array measurements that were analyzed using the automated reinforcement location software versus core measured concrete cover. It can be observed that using an automated procedure to identify the centroid of high reflectivity regions in the reinforcement vicinity of the ROI not only allows for productive analysis, but the calculated concrete cover corresponds well with core measurements (R^2 = 0.997, slope = 0.985). As will be discussed in more detail in Chapter 5, this accuracy significantly exceeded the accuracy of the conventionally used methods for this application.

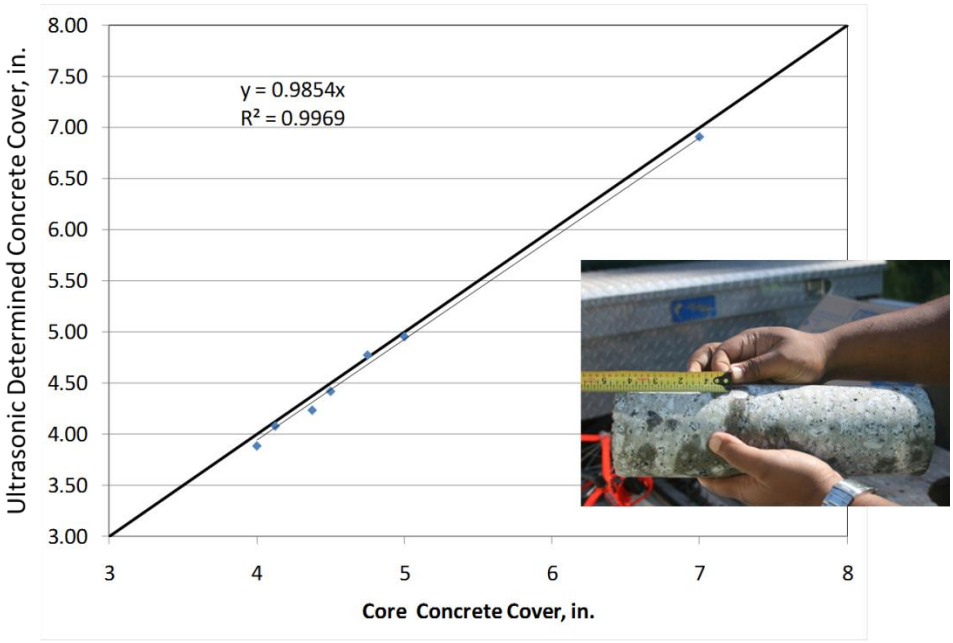

Figure 4-3. MIRA measured and software analyzed concrete cover versus core measured.

4.1.3 Delamination Detection

A comparison of high reflectivity regions with the expected inclusion or layer boundary locations gives information about the condition of the surrounding concrete in a pavement structure. If no high reflectivity locations are observed within the concrete layer other than at as designed inclusions or layer boundary positions, this indicates a sound concrete condition. Figure 4.4 shows an example SAFT-IA reconstruction from a scan location on a CRCP pavement in Antwerpen, Belgium where direct circular reflection locations indicate the position of the as designed longitudinal reinforcement locations. The lack of direct reflections at the locations between the reinforcement indicates a sound concrete condition.

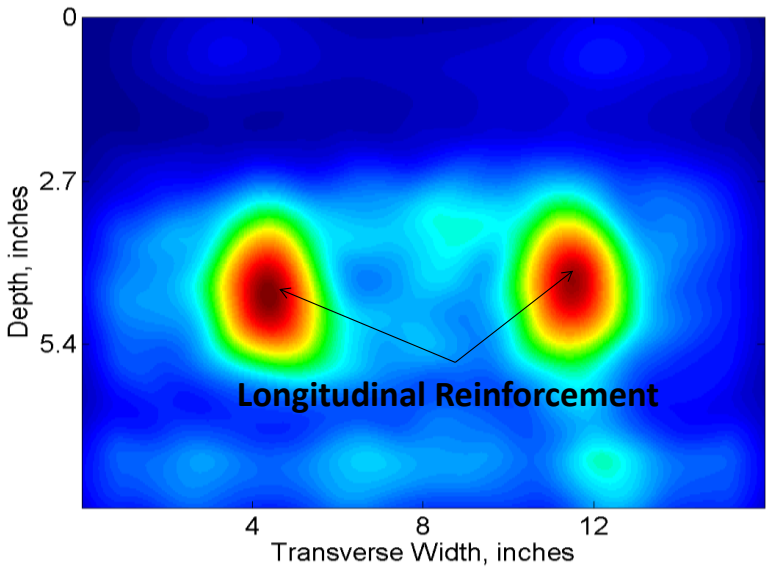

Figure 4-4. SAFT-IA reconstruction indicating the location of reinforcement and sound concrete condition.

Figure 4.5 shows the forensic verification of the sound concrete condition at the ultrasonic scan location. It can be observed that the direct reflection results were used to mark the location of the reinforcements prior to coring. The red circle mark was made between the reinforcement locations and a core was taken to verify the sound concrete condition. It can be observed from the core that the concrete is in relatively sound condition.

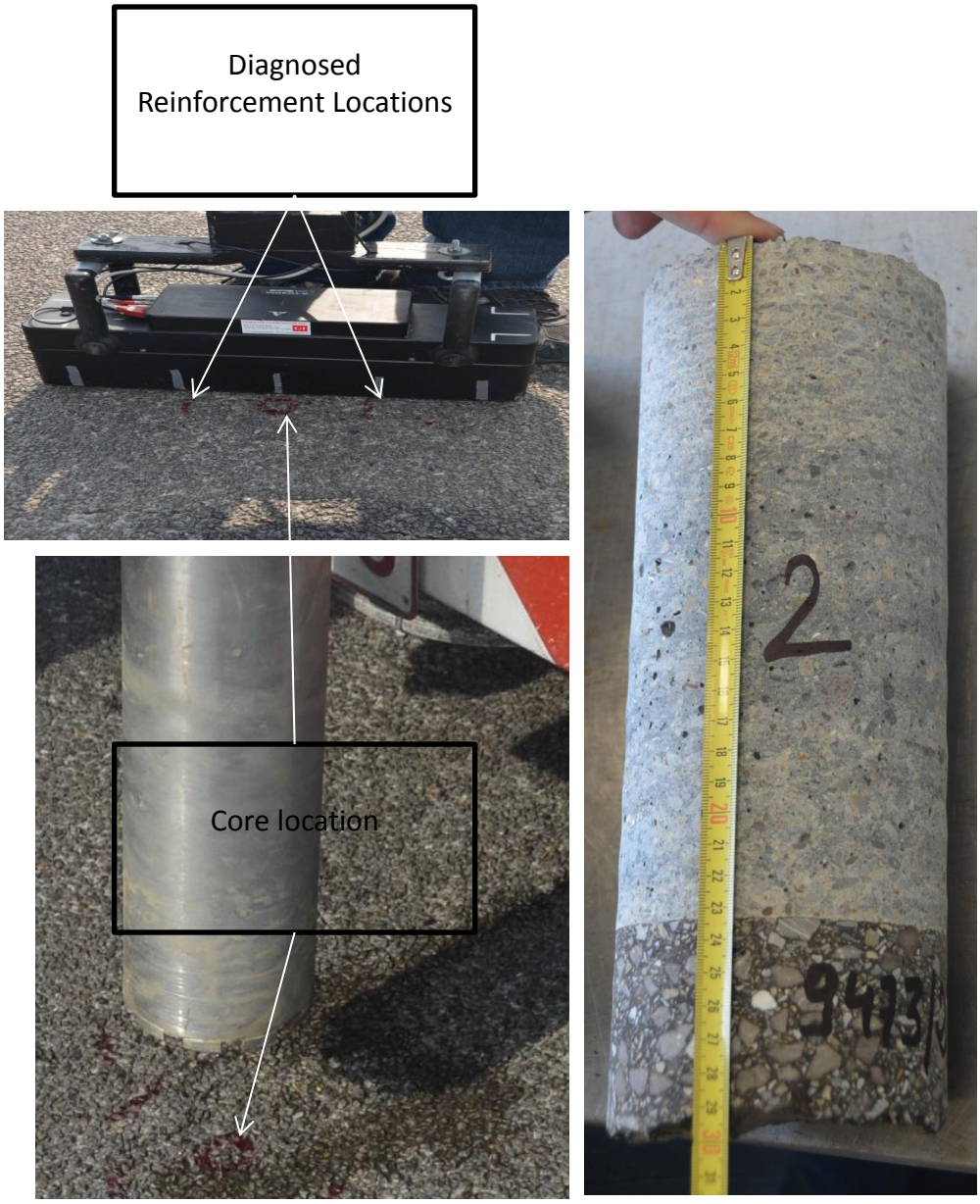

Figure 4-5. Forensic verification of the sound concrete condition.

Locations within the reconstructions where high intensity reflections are observed other than locations were designed inclusions or layer boundaries are present are indicative of a certain extent of damage. Figure 4.6 shows a SAFT-IA reconstruction with a strong oblong reflection at a location indicating damage at the level of the reinforcements at different location in the same CRCP pavement. It can be observed that there is an oblong high intensity reflection connecting the locations were the reinforcement is located where

no designed layer boundary should be expected. This indicates the presence of delamination of the concrete at the level of the reinforcement.

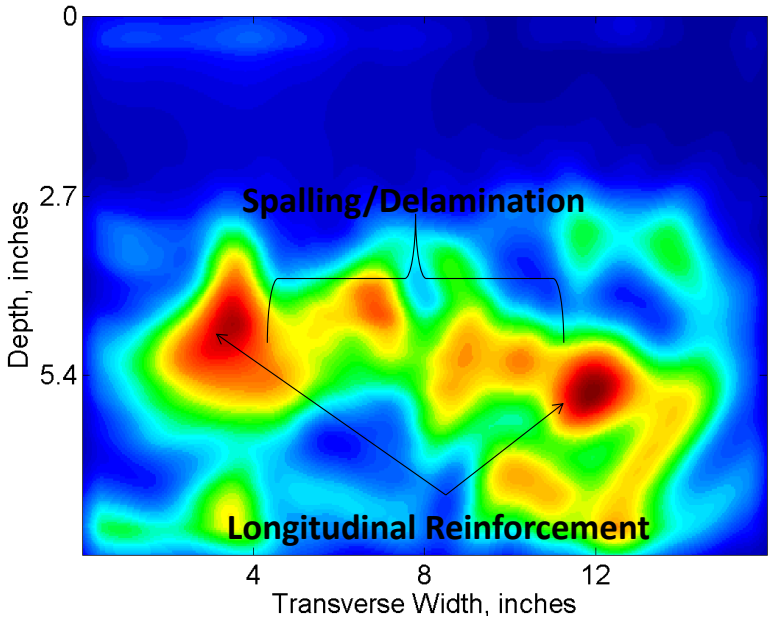

Figure 4-6. Direct reflection indicating a damaged concrete condition at the depth of the CRCP reinforcement.

Figure 4.7 shows the forensic validation of the damaged concrete condition. It can be observed that the high reflectivity results were used to mark the location of the damage prior to coring. The red circle mark was made adjacent to the reinforcement location so a core could be taken to verify the delamination initiating at the reinforcement. It can be observed from the core that the concrete is delaminated at the depth of the reinforcement as SAFT-IA analysis suggested. The bottom of figure 4.7 shows the delamination at the reinforcement.

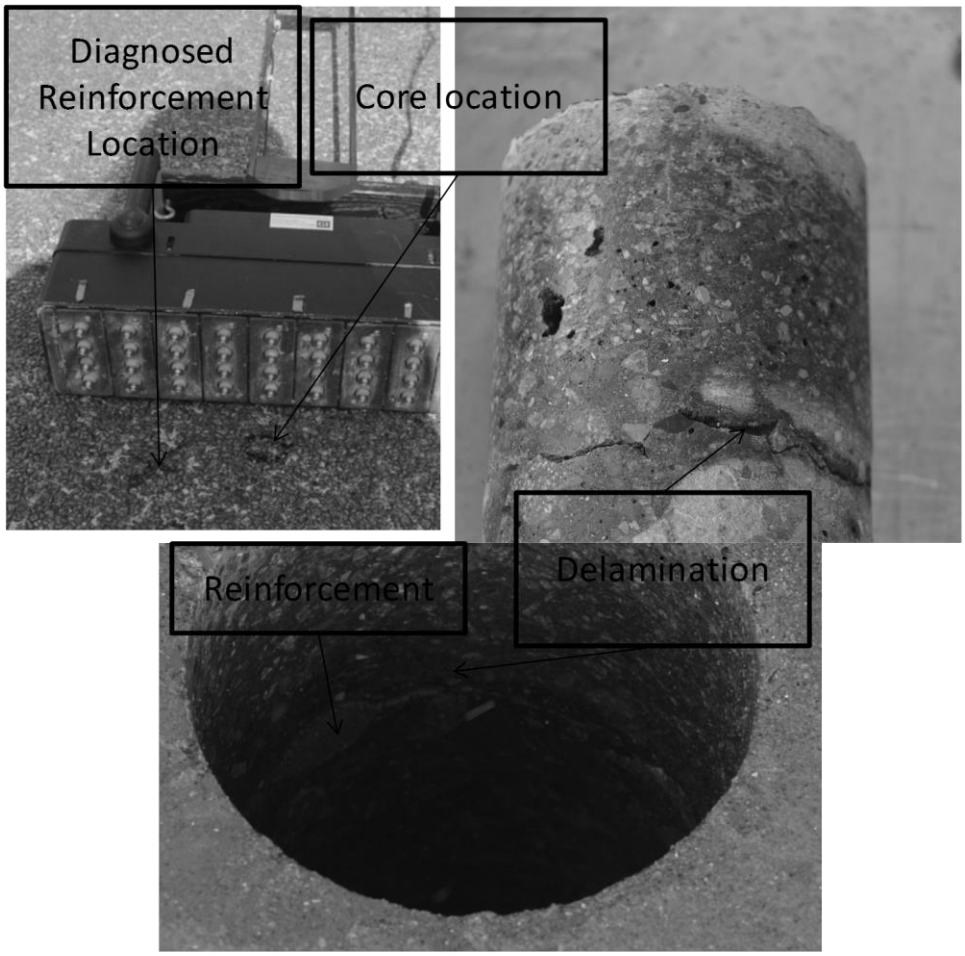

Figure 4-7. Forensic verification of the delaminated concrete condition.

4.1.4 Defect Inclusions

Changes in acoustic impedance in the form of inclusions result in strong reflections within the PCC layer at the depth and lateral location of the inclusion when evaluating the relative reflectivity within the SAFT-IA reconstructions. Figure 4.8 shows the SAFT-IA reconstruction as well as embedded plastic wrapped porous concrete inclusion. This object, along with other fabricated inclusions, was embedded in a test pavement at MnROAD to simulate poor consolidation/foreign particle inclusions in the PCC layer. High reflectivity within the ROI at the location of the inclusion can be observed indicating its presence. Inclusion identification validation is discussed in more detail in section 4.4.

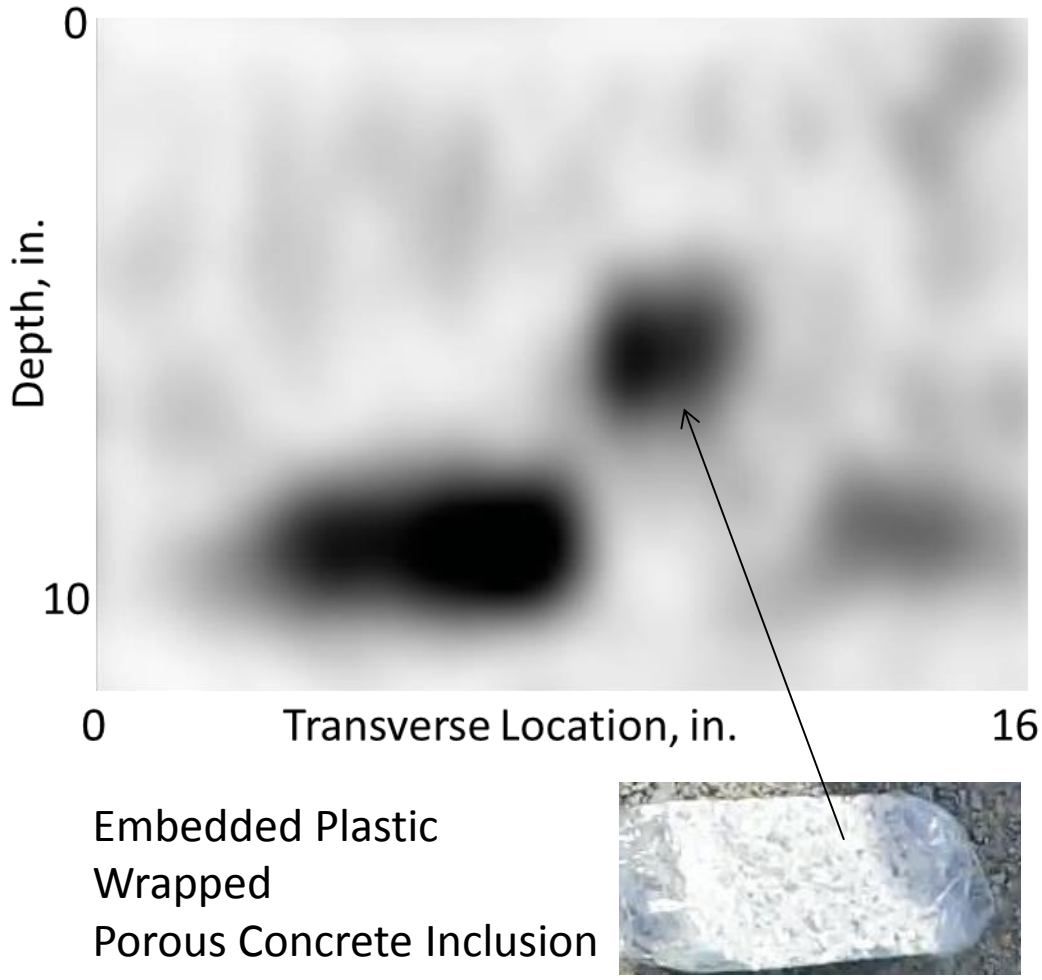

Figure 4-8. SAFT-IA reconstruction with indicating the location of an embedded porous concrete inclusion.

4.1.5 Deterioration

In addition to circular and horizontally oriented cracking and inclusions within the concrete layer, vertical or angled cracking and deterioration of the subsurface of the concrete can also be evaluated using SAFT-IA reconstructions. In this case, while large changes in acoustic impedance are present in the ROI, the incidence angle does not always result in high amplitude reflections back to the surface. Thus, high reflectivity within the reconstruction is not always observed in the region of these changes in acoustic impedance within the ROI. However, these types of distresses can often be identified by shadowing, where the pulse does not transmit through the boundary created

by the distress. While this type of indirect analysis is best identified using the UTSA analysis discussed in section 3.2.2, an example of shadowig analysis for flaw detection using SAFT-IA analysis can be observed below. Ultrasonic scans and resulting SAFT-IA reconstructions from a different location in the CRCP section in Antwerpen, Belgium used in section 4.1.2 are shown in figures 4.9 and 4.10.

Figure 4.9 shows a progression of SAFT B-scans taken at a transverse crack. Scans were taken with MIRA centered 4 in. to the left of the crack, 2 in. to the left of the crack, and centered on the crack shown from left to right, respectively. It can be observed from the direct reflections that there is delamination at the depth of the reinforcement. However, the gap in the reflectivity at the delamination level corresponds to the location of the measurement in relation to the vertical transverse crack. This indicated that the vertical crack propagated at least to the depth of the horizontal delamination. However, high reflectivity at the vertical crack location was not observed, rather by the gap in the reflectivity at the delaminated level caused by the lack of a transmitted pulse trough the vertical crack boundary. The core shown in Figure 4.10 shows the validation of the horizontal delamination as well as the full depth propagation of the vertical crack.

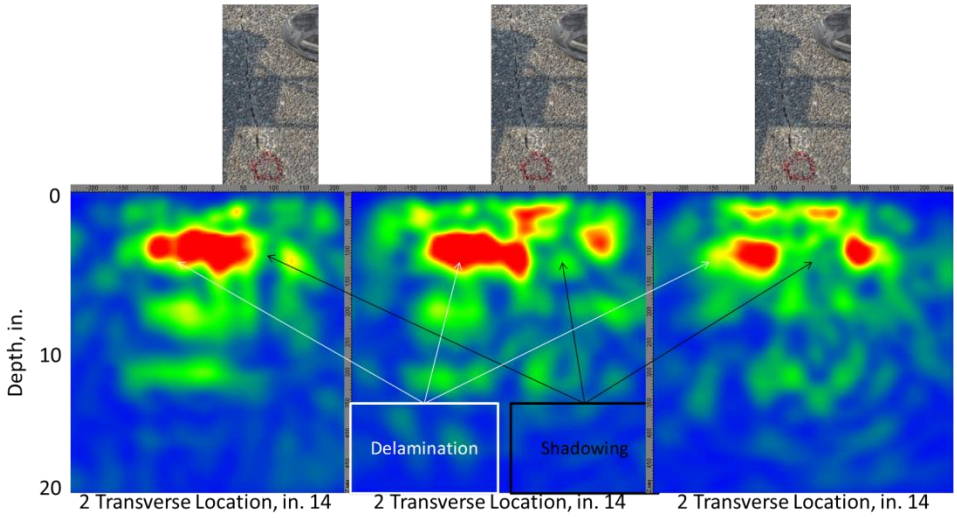

Figure 4-9. SAFT-IA reconstructions indicating the presence of a vertical and horizontal crack.

Figure 4-10. Forensic verification of the delaminated concrete condition with vertical crack.

4.2 SAFT Panoramic and Enhanced Panoramic Reconstruction

As explained in Chapter 3, the assumptions and parameters for the SAFT-Pan and SAFT-EPan methods are similar to SAFT-IA analysis in that they are determined based on creating a relative reflectivity reconstruction that matches changes in acoustic impedance within the ROI. An example of each of these reconstructions versus forensic results is given herein.

4.2.1 SAFT Panoramic

Figure 4.11 shows the starting and stopping point of overlapping ultrasonic linear array scans taken at a MnROAD concrete pavement transverse joint(top), the resulting SAFT-Pan reconstruction (middle), as well as the forensic verification (bottom). The orange box around the SAFT-panoramic reconstruction corresponds to the orange box around

the cross section of the pavement at that scanned location as revealed by trenching the joint.

It can be observed that the mid-depth of the high intensity reflection on the left of the SAFT-Pan is approximately 9 inches in depth, which corresponds to the PCC slab thickness and indicates sound concrete. Forensics confirms this assessment as shown on the left side of the interface in figure 4.12. A shallower high intensity reflection can be observed on the right side of the SAFT-panoramic reconstruction. The mid-depth of this reflection is approximately at 4.5 in. This corresponds with the depth of the delamination that can be observed at about 4.5 in. depth on the right side of the forensic interface validating the SAFT-Pan reconstruction of the relative subsurface reflectivity in the example cross-section of the pavement. Although this is a fairly straight forward diagnosis using ultrasonic linear array scans with SAFT-Pan analysis, this subsurface distress was not identified by other state of the art and conventional nondestructive evaluation methods, as will be explained in more detail in the case study given in Chapter 5.

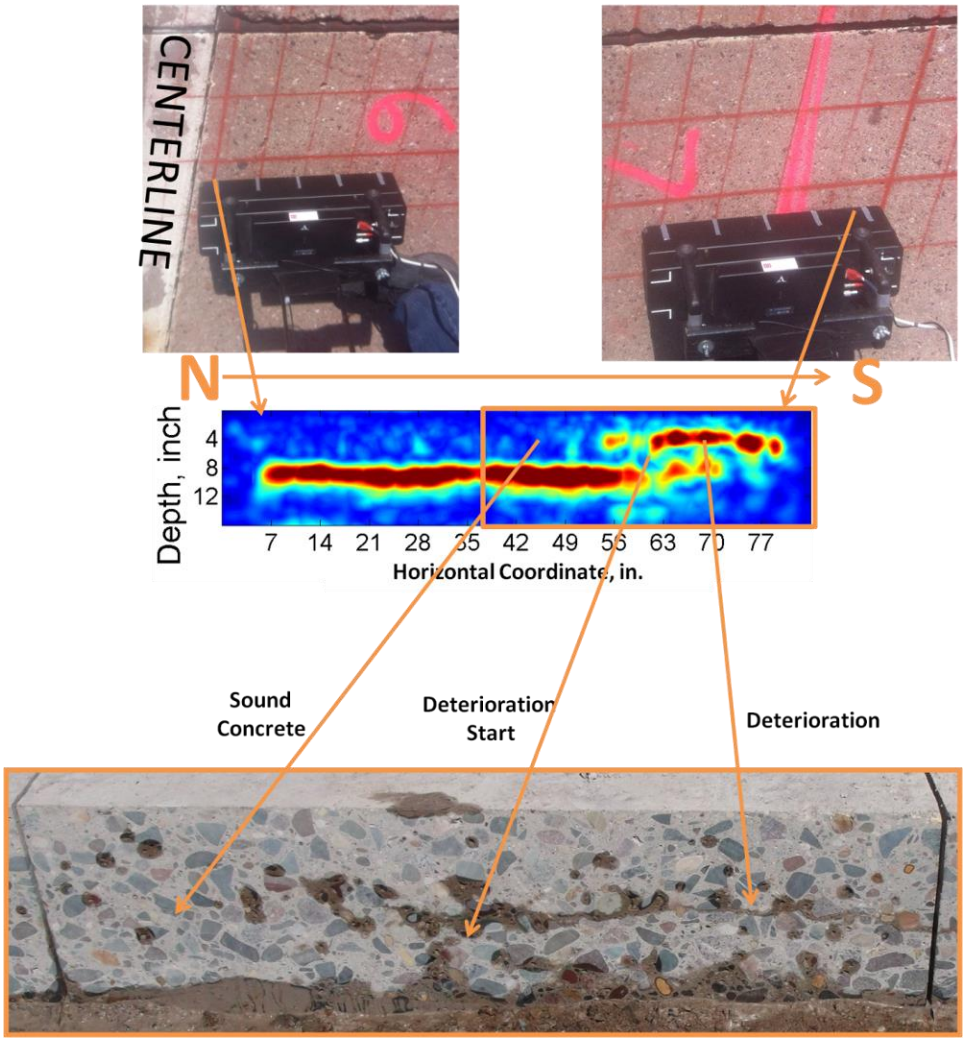

Figure 4-11. SAFT-Pan reconstruction and comparison with the actual delamination crack path at a MnROAD concrete pavement transverse joint.

4.2.2 Enhanced Panoramic Reconstruction

As discussed in section 3.2.3, there are situations where the physical location of each SAFT-IA B-scan used to create a panoramic reconstruction is not known to the desired accuracy. This can potentially introduce significant error in the SAFT-Pan reconstruction described in section 3.1.4 which is based on using pre-defined locations when applying SAFT-IA scans. Figure 4.12 shows an example of a SAFT-Pan reconstruction which combines three individual SAFT-IA reconstructions using a target 2.5 inch shift factor. This type of blurred reflection is inconsistent with the reflectivity of a round metal dowel

surrounded by sound concrete. This type of reflection may indicate presence of damage of the concrete around the dowel.

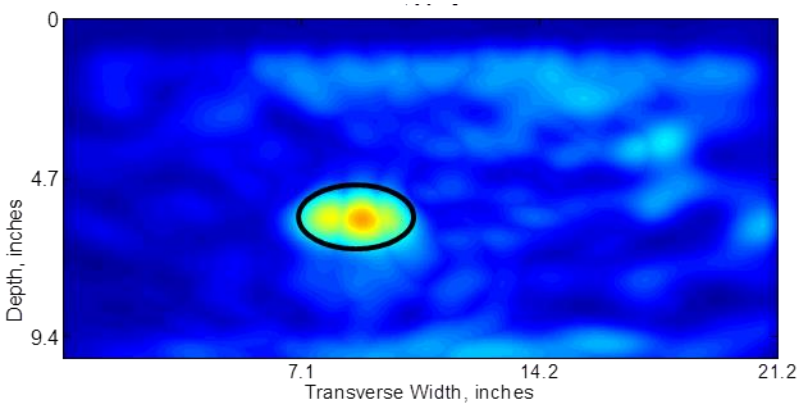

Figure 4-12. SAFT-Pan reconstruction with imprecise step size input.

To investigate the cause of the blurred reflectivity in the area of the dowel, the SAFT-EPan reconstruction procedure was employed. Figure 4.13(a) shows the SAFT-EPan reconstruction obtained from the same three individual SAFT-IA scans. The shift factors were determined by using the highest similarity of overlapping regions using the procedure described in section 3.2.3 resulting in shift factors significantly less than the 2.5 inch target shift factors, equal to 1.8 in. and 1.7 in. when placing the $m = 2$ and $m = 3$ SAFT-IA reconstructions, respectively.

It can be observed that the new shift factors, determined using the enhanced panoramic reconstruction procedure, resulted in focusing of the reflectivity reconstruction in the area of the dowel. This type of focused reflectivity in the reconstruction should be expected at a round steel reinforcement embedded in sound surrounding concrete.

A core at the doweled transverse location is also shown in figure 4.13(b) indicating a single dowel with relatively sound surrounding concrete. This validates that the blurred reflectivity in the region of the dowel was caused by the difference between the actual scan locations and the pre-defined 2.5 in. shift factors used in the SAFT-Pan reconstruction. This also validates that the SAFT-EPan reconstruction correctly focused

the reflectivity to the actual change in acoustic impedance to the region of the embedded dowel.

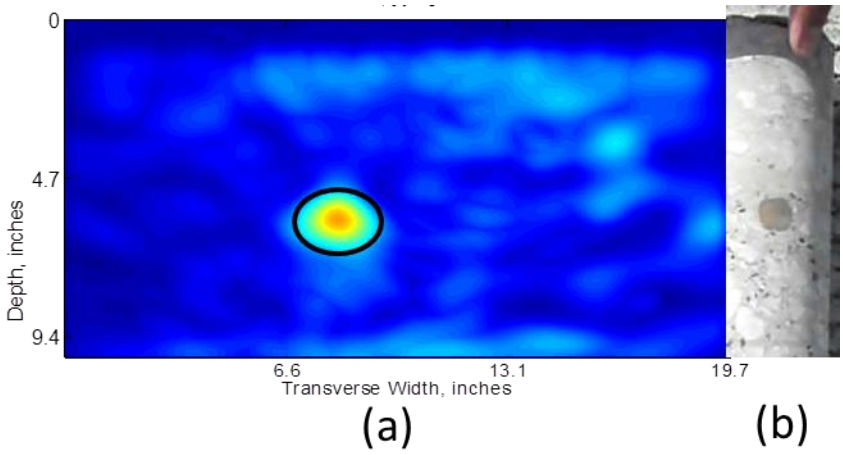

Figure 4-13. SAFT-EPan reconstruction and subsequent forensics at the example overlapping scans location.

4.3 SAFT Phase Analysis

As discussed in section 3.1.2, the SAFT reconstructions can be used to represent the reflectivity of the ROI more effectively when using the instantaneous amplitude to represent the signals. While this allows for focused reconstruction, the phase information of the impulse is lost when converting from the raw impulse data to the instantaneous amplitude. While this is rarely a concern in concrete pavement evaluations, there are certain cases where the phase information of the raw impulse data should be preserved during the reconstruction process. One example where phase information can be useful in pavement nondestructive evaluation includes analysis of the concrete bond condition around two major types of reinforcement in concrete pavements (rebar and dowels, respectively).

Rebar is typically designed to resist horizontal movements. Tie bars are a type of rebar used in jointed plain concrete pavement (JPCP) that is designed to restrict horizontal movements of longitudinal joints. Mesh grid rebar are used in CRCP to restrict crack

opening. This type of reinforcement is designed to have a full bond with the surrounding concrete.

Dowels are designed restrict differential vertical movements in JPCP transverse joints to provide vertical load transfer across the joint without restricting horizontal movements. These reinforcement types typically are fabricated with an epoxy coating and/or greasing agent applied during placement to break the bond between the dowel and the surrounding concrete. A properly functioning dowel should not be bonded to the concrete allowing for concrete shrinkage and thermal expansion and contraction of the concrete pavement.

Figure 4.14 illustrates an example SAFT reconstruction from a scan taken on a newly constructed concrete pavement on top of (a) a dowel in a transverse joint and (b) a tie bar in a longitudinal joint. It can be observed that in both cases, there are high amplitude reflections in the vicinity of the ROI where the reinforcement is embedded. However, the polarity of the pulse reflected from the different reinforcement locations has a different pattern. The pulse from the location of the dowel (circled in black in figure 4.14(b)) is similar to the direct arrival polarity pattern shown in figure 2.7, or reflection at the concrete layer depth as shown in figure 3.5 below 13 inches, where a highly positive magnitude is followed by highly negative amplitude. The pulse from the location of the tie bar (circled in black in figure 4.14(a)) is similar to the polarity pattern shown in figure 3.5 at the CRCP rebar locations just below 8 inches in depth, where a highly negative magnitude is followed by highly positive amplitude.

Based on the functionality of the reinforcement types described above, and by referencing equation 2.3, it follows that a properly functioning rebar should have the opposite polarity pattern of a properly functioning dowel. The reflections associated with the tie bar in figure 4.14(a) and CRCP rebar locations in 3.5 should experience a π phase shift when reflecting from a bonded higher acoustic impedance interface such as bonded steel in concrete. In the other cases, including the greased and un-bonded condition around the dowel, the reflecting interface (air in the case of the un-bonded dowel) does not cause a phase change in the pulse.

Figure 4.14 shows the bond condition of the concrete around the (a) tie bar and (b) dowel. While it is difficult to observe the different concrete bond conditions visually, it is clear from the designed functionality and differences in phase in the SAFT reconstructions that there is a difference in bond condition. While the bond condition, and thus phase of the SAFT reconstructions, is variable, these are the general phase differences observed consistently between these two types of reinforcement when applying the SAFT reconstruction to linear ultrasonic array signal pairs. This validates the ability of SAFT reconstruction in differentiating bond condition based on phase of the reflected pulse.

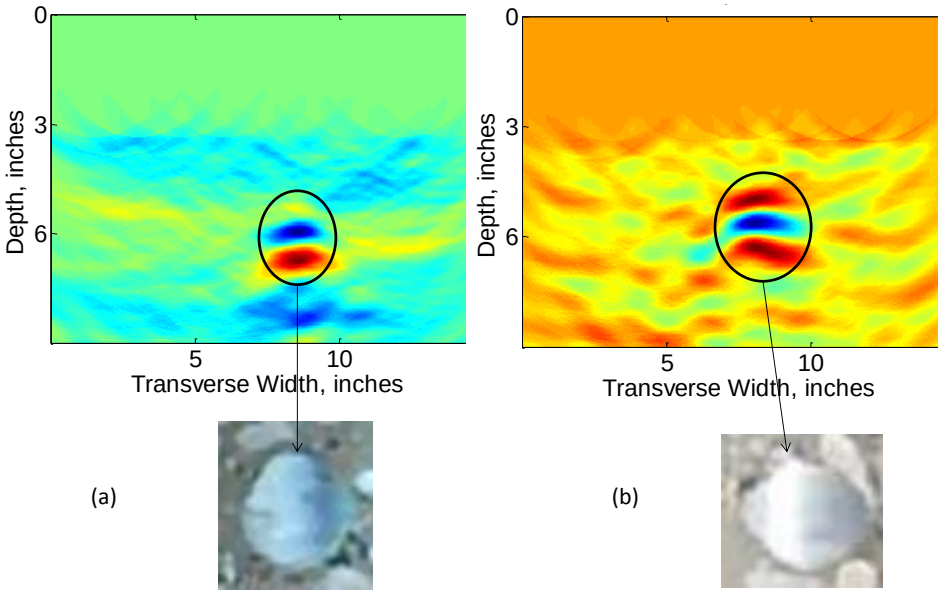

Figure 4-14. SAFT reconstruction and reinforcement/concrete bond condition for an (a) tie bar, and (b) dowel.

4.4 Signature analysis

As discussed in section 3.2, the manual data interpretation of the Kirchoff migration based reconstructions for various pavement nondestructive evaluations can be time consuming and labor intensive. The automated 2D-UTSA procedure and process of selecting a reference signal is discussed in this section.

4.4.1 Defect Detection

To evaluate the robustness of the UTSA method in identifying subsurface distresses, a series of tests were conducted. This included testing at the Minnesota Road Research Facility (MnROAD) and the Federal Aviation Administration's National Airport Pavement Test Facility (NAPTF) (Hoegh and Khazanovich, 2012).

The ultrasonic linear array testing at MnROAD was conducted to verify the robustness of the UTSA method for locating defects with known dimensions and locations. To accomplish this, various defects were fabricated and embedded in the concrete at a fully bonded two-lift concrete pavement construction test site. The defects were fabricated to represent random "honeycombing" flaws in the concrete. The three defects embedded in the concrete included plastic wrapped aggregate in the center of the slab, a plastic wrapped porous concrete semi-cylinder on the left side of the slab, and a porous concrete semi-cylinder on the right side of the slab. Figure 4.15 shows the fabricated inclusions.

Figure 4-15. Fabricated inclusions: (a) a plastic-wrapped porous concrete semi-cylinder, (b) plastic-wrapped aggregate, and (c) a porous concrete semi-cylinder.

The testing involved 41 adjacent ultrasonic linear array scans taken in 3 in. (76 mm) increments moving toward the right above the fabricated inclusions. Using this type of testing procedure, it would be expected that the relative reflectivity in the SAFT-IA reconstructions from each of the embedded inclusions should move toward the left side

of the reconstruction as the device is moved to the right as the relative position of the change in acoustic impedance is moving to the left.

Testing at the NAPTF was conducted to verify the 2D-UTSA technique in a situation where the presence or type of damage was unknown. Testing was conducted on a slab exposed to a potassium acetate deicer. As indicated in Figure 4.16, cores taken at a location in this slab prior to ultrasonic linear array testing showed little to no damage. Analysis of SAFT-IA B-scans was conducted to verify that the "damage free" core was representative of the rest of the pavement. The testing procedure was similar to that conducted at MnROAD with 3 in. (76 mm) increments between adjacent scans. However, the scanning step size direction was perpendicular to the length of the device rather than along the length.

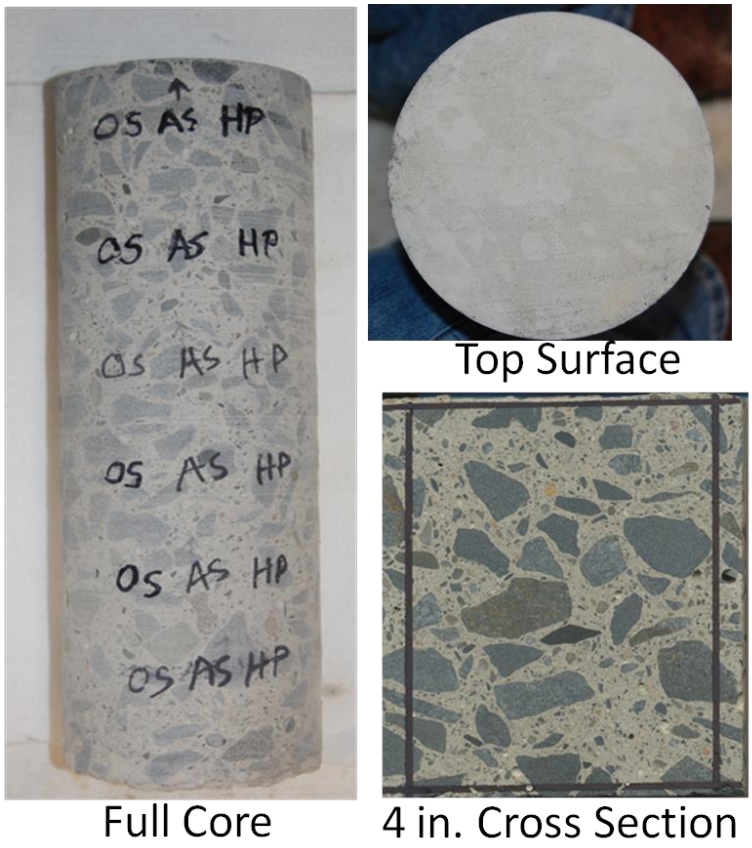

Figure 4-16. Core indicating "damage free" concrete at the NAPTF slab location.

The UTSA correlogram for ultrasonic linear array scans taken at MnROAD locations without fabricated distresses are shown in Figure 4.17. It can be observed from this figure that there is a small amount of variation in Pearson's coefficient at these locations, ranging from 0.90 to 0.93. Scatter of this magnitude is on the order of that which could be caused by structural noise from the variable aggregate and air void distribution. When analyzing the presence of flaws or inclusions in concrete, this type of scatter in Pearson's coefficient should be ignored.

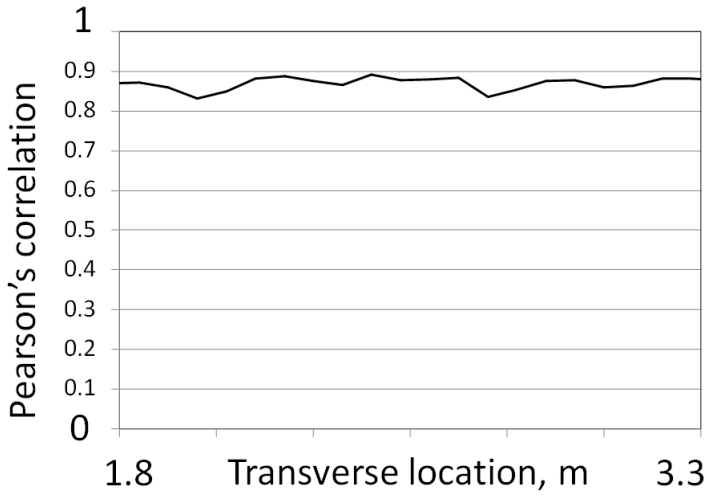

Figure 4-17. Correllelogram of concrete without an embedded inclusion, indicating the absence of a subsurface defect.

Figure 4.18 shows the 2D-UTSA correlogram of the scans obtained above of the artificial defects using a manually selected reference scan representing "damage free" concrete. Decreases in Pearson's correlation can be observed in three locations that are much larger than that which would be expected from structural noise. These decreases in Pearson's correlation coefficient correctly indicated the presence of the fabricated defects, and are similar to decreases in the IESA analysis of the simulated defects shown in Figure 2.29.

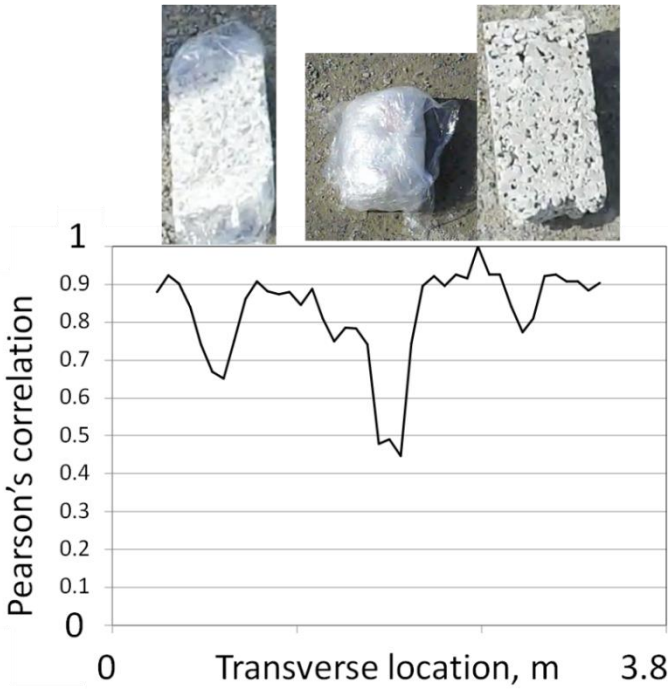

Figure 4-18. Correlogram from 41 adjacent measurements above the fabricated distresses.

A zoomed-in view of the leftmost artificial defect and corresponding correlogram dip, as well as sample SAFT-IA scans resulting in the drop in Pearson's correlation, are shown in Figure 4.19. In this case, observations of the various SAFT-IA scans indicate the presence of the distress by the high reflectivity in the inclusion vicinity of the ROI. Shadowing of the backwall reflection at the concrete depth interface below the artificial defect can also be observed. While, in this case, the defect could be identified by visual inspection of the SAFT-IA scan, use of the UTSA method mitigates this need for engineering judgment, and can be used as a more efficient and objective analysis method for larger scale cases where it is not feasible to manually evaluate each scan in detail. This MnROAD example provided validation of the UTSA procedure with regard to identifying typical subsurface defects in preparation for applications where the presence, type, and location of any possible defects are unknown.

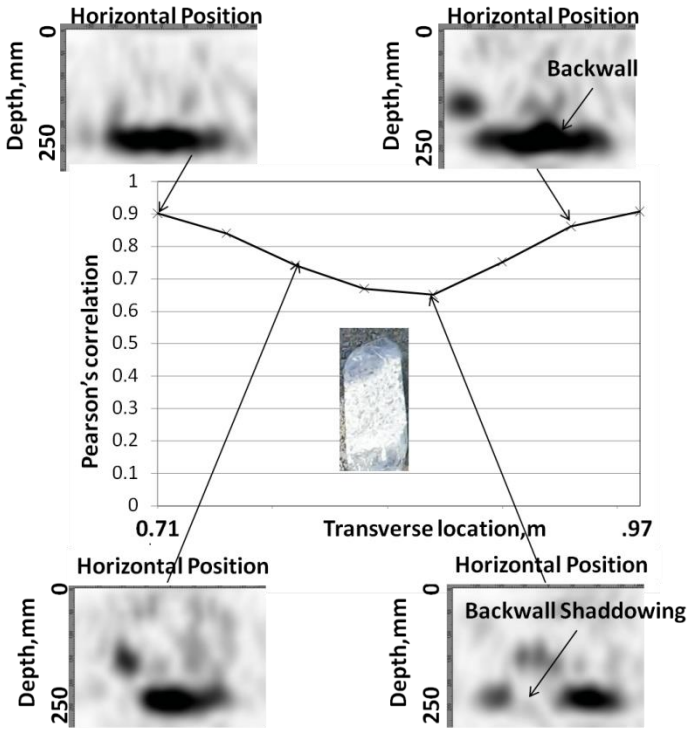

Figure 4-19. Zoomed-in view of the leftmost fabricated defect, corresponding dip in the correlogram, and sample SAFT-IA scans indicating the presence of the defect.

The verified UTSA method was then applied to the NAPTF concrete pavement section. A trend similar to that shown in Figure 4.17 was observed at most locations, confirming that the "damage free" cores were representative of most of the pavement area. However, in one location, a decrease in the Pearson's correlation similar to that seen in Figure 4.18 was observed in the correlogram. The SAFT-IA scans adjacent to, as well as directly at the locations of decreased correlation, are shown in Figure 4.21. A shallow, approximately 4 in. (~100 mm) deep reflection can be observed in addition to shadowing of the backwall reflection at locations A through D corresponding to the dip in the correlogram. A core was taken at the location of the observed dip in the correlogram. Figure 4.20 shows the presence of a horizontal delamination, as well as some poor consolidation in the core. Forensic analysis of the cross-section of the core and pavement interface where the core was taken also identified that the delamination covered a smaller portion of the MIRA aperture at locations A and D from Figure 4.20, while locations B

and C correspond to scans taken directly above the delamination. This validated that the UTSA identification of a subsurface defect was indeed correct.

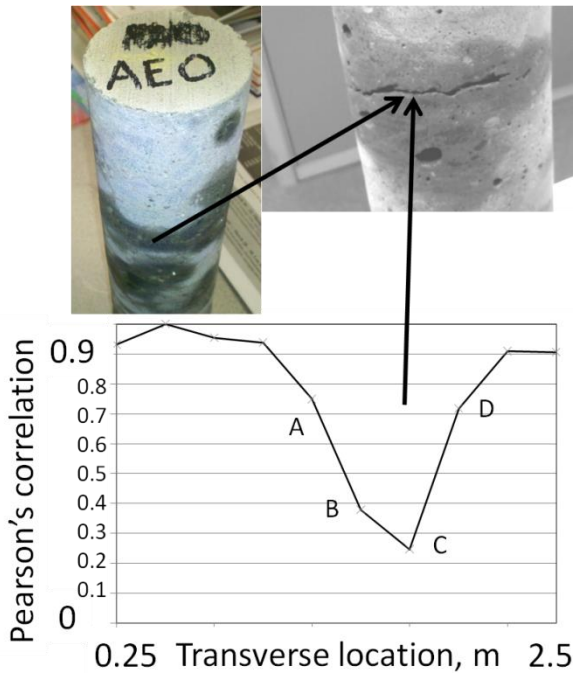

Figure 4-20. Correlogram indicating a subsurface defect at the NAPTF site using a manually selected reference scan.

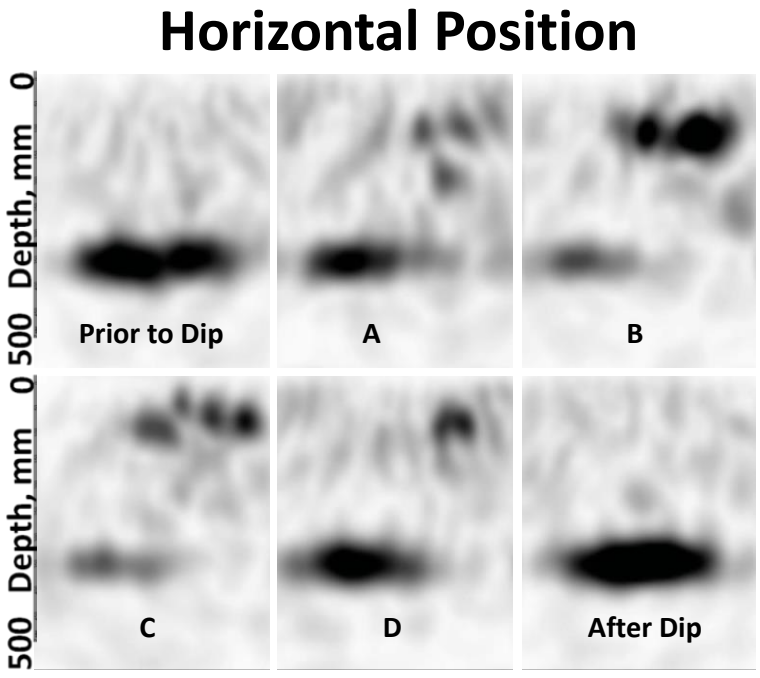

Figure 4-21. SAFT-IA reconstructions at locations A,B,C,D as shown in Figure 4.20.

4.4.2 Reference Signal Determination

The robustness of the UTSA method is evaluated below by replacement of the manually selected reference SAFT-IA B-scan with an averaged reference SAFT-IA B-scan. Figure 4.22 shows a correlogram created using the average of all scans as the reference scan representing the same MnROAD area shown in Figure 4.18. It can be observed that the use of the averaged reference scan results in lower correlations than those obtained from the manually selected reference scan. However, correlogram dips are observed at the same locations as in the correlogram generated using the manually selected reference scan. Thus, the 2D-UTSA analysis using the averaged reference scan method also resulted in detection of the fabricated defects.

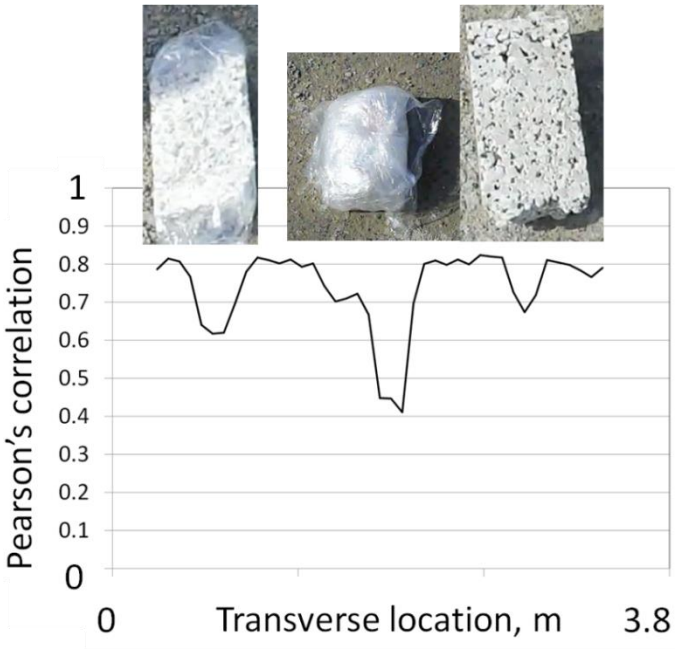

Figure 4-22. Correlograms from 41 adjacent measurements above the fabricated distresses using the averaged reference scan.

The averaged reference scan approach was also applied for 2D-UTSA analysis on the NAPTF slab. Figure 4.23 shows the correlogram generated using the averaged reference scan for the same location where a subsurface defect was identified. This analysis was conducted in an area where 40 percent (4 of 10 scans) of the scans were taken in the vicinity of the subsurface defect. It can be observed that even in this challenging case,

the decrease in the Pearson's correlation is observed when using the averaged reference scan. However, locations A and D were not identified as having any distresses below the scanning location. This validates that, even for a reference scan which is not completely representative of sound concrete, the 2D-UTSA analysis is capable of damage detection if a significant portion of the scans are taken on sound concrete. However, proper selection of the reference scan increases the resolution of UTSA analysis.

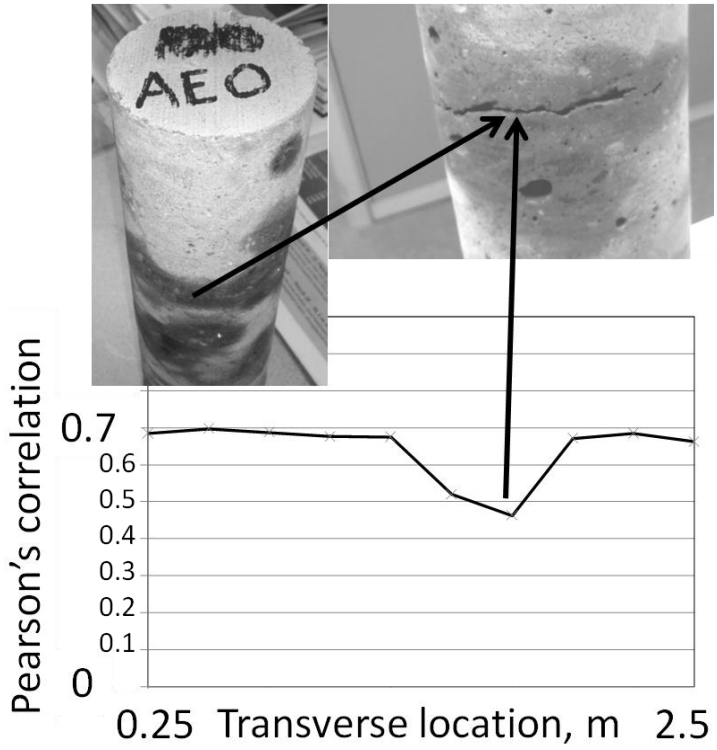

Figure 4-23. Correlogram indicating subsurface defect at the NAPTF test slab, as compared to the averaged reference scan.

5 Case Studies

The ultrasonic linear array signal processing techniques were used to investigate several practical engineering problems at in-service concrete pavements. This included reinforcement and thickness detection as well as bond evaluation and subsurface deterioration.

5.1 Georgia CRCP

Ultrasonic linear array (MIRA) testing was conducted to determine concrete cover and pavement thickness. MIRA testing of continuously reinforced concrete pavement (CRCP) was conducted on I-85 near Atlanta, GA for project NHS-M002-00(434)01, Coweta county. Ultrasonic linear array diagnosed longitudinal bar depths and concrete thicknesses results are presented along with a comparison with convention nondestructive testing (pachometer) results and subsequent core measurements. In addition, the measurement process and data interpretation method are detailed.

5.1.1 Testing Procedure

Testing was conducted after the construction process, but prior to opening to traffic, at several sections of CRCP pavement on I-85 in Atlanta. The testing was initiated due to suspected variability in concrete thickness as well as cover between the reinforcement bars and surface and/or base. Ultrasonic linear array testing was conducted on these sections to estimate the variability in construction, as other conventional nondestructive techniques such as the pachometer proved to be inconsistent for this application. Measurements were taken in 50 ft intervals of northbound I-85 from stations 145+00 to 324+00 (excluding the bridge section) as well as southbound shoulder I-85 from stations 360+00 to 430+00. Figure 5.1 illustrates the general layout of the tested sections with northbound I-85 lanes on top in Figure 5.1a and the southbound lane on the bottom in Figure 5.1b (not to scale/proportional).

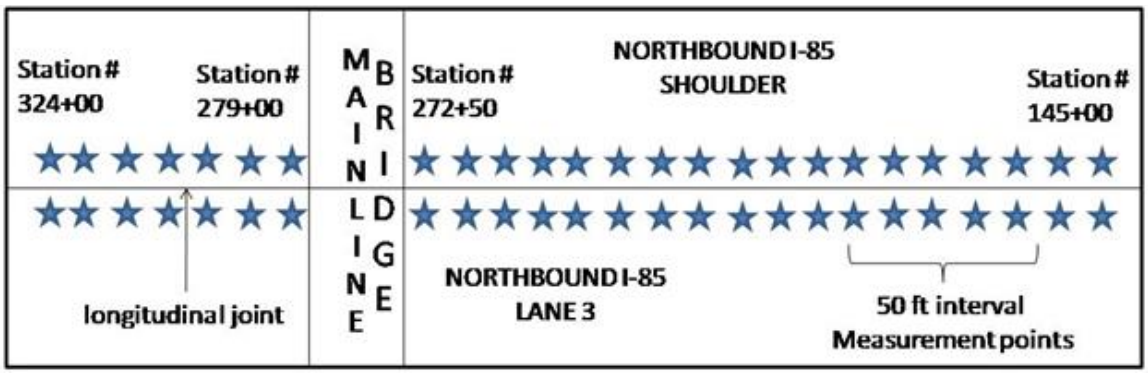

5.1a. Northbound Lane 3 and shoulder general layout.

5.1b. Southbound shoulder general layout.

Figure 5-1. Illustration of the general layout of testing (not to scale/proportional).

Seven cores were taken at the center of the lanes for calibration/verification purposes (2 in the northbound lane, 2 in the shoulder of the northbound lane, and 3 in the southbound shoulder). Measurements were centered approximately 18 in. from the longitudinal joint with the long portion of the device aperture perpendicular to the direction of traffic and the right side of the device and corresponding right side of the resulting SAFT-IA reconstructions closest to the longitudinal joint.

Figure 5.2 shows an example of the orientation of the device aperture with respect to the lane. The southbound lane measurements were made in closer proximity to the edge as shown in figure 5.3. This was done for comparison with the visible interface at the longitudinal joint as no pachometer markings were present for comparison. The concrete cover of the rebars closer to the center of the lane was not measured in this study except for the core location measurements for calibration purposes. At the calibration locations in lane 3 of northbound I-85, 28 scans were taken leading up to and beyond the 50 ft interval marking with the measurement directly over the marking between the 15th and

17th scans. Five scans were taken on all locations between calibration points with the 3rd scan directly over the marking.

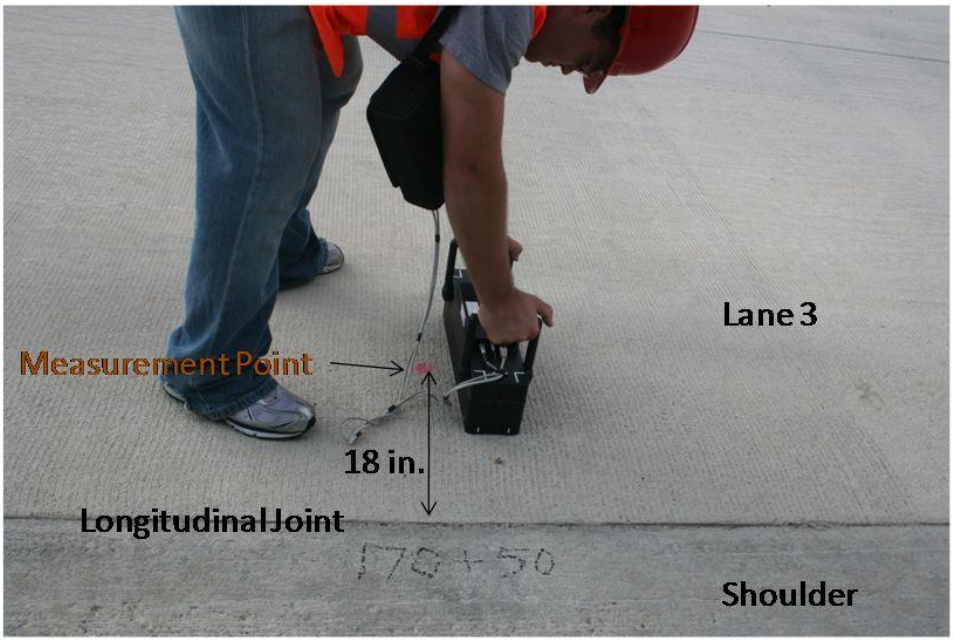

Figure 5-2. Orientation of the ultrasonic linear array device in lane 3 of northbound I-85.

Figure 5-3. Orientation of the device for measurements of the southbound I-85 lane.

Figure 5.4 shows an example calibration point where 28 measurements were taken at 20 mm intervals (measurement 16 is directly over the top of the 50 ft interval marking in this case). In the shoulder of northbound I-85, 3 scans were taken at each location with the 2nd scan directly over the marking. In some locations (<5%) the surface was too rough or uneven for proper coupling of all 40 transducers of the device aperture. In these locations, the aperture was moved to a location in close proximity where proper coupling could be achieved, or no measurement was given in that location. Figure 5.5 shows an example location where the surface was rough/uneven so the measurement was moved closer to the center of the lane. In the southbound lane, 6 scans were taken at each measurement location with the 4th scan corresponding to the center of the measurement point.

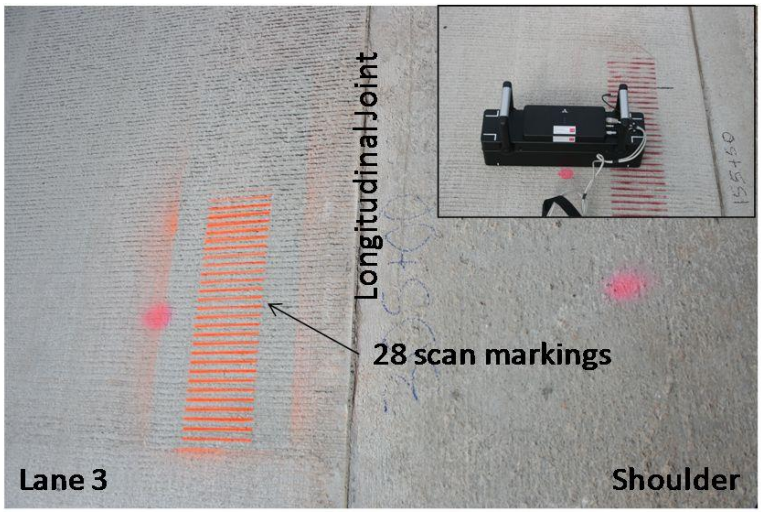

Figure 5-4. Calibration location in lane 3 where 28 scans were made with the 16th scan located directly over the measurement location.

Figure 5-5. Example of a rough surface that required the device to be move to the left for proper coupling of the transducers.

5.1.2 Analysis and Results

In each ultrasonic linear array SAFT-IA reconstruction, the presence of two or three longitudinal bars could be identified, and their depths measured. Figures 5.6(a) and 5.6(b) show typical output displays showing 2 and 3 longitudinal bars within the aperture, respectively. Figure 5.6c shows a SAFT-IA reconstruction with high reflectivity in the region of the reinforcements as well as the PCC thickness interface. SAFT-IA reconstructions were used along with the automated analysis methods described in section 3.2.1 to determine the depth of the reinforcement and pavement thickness.

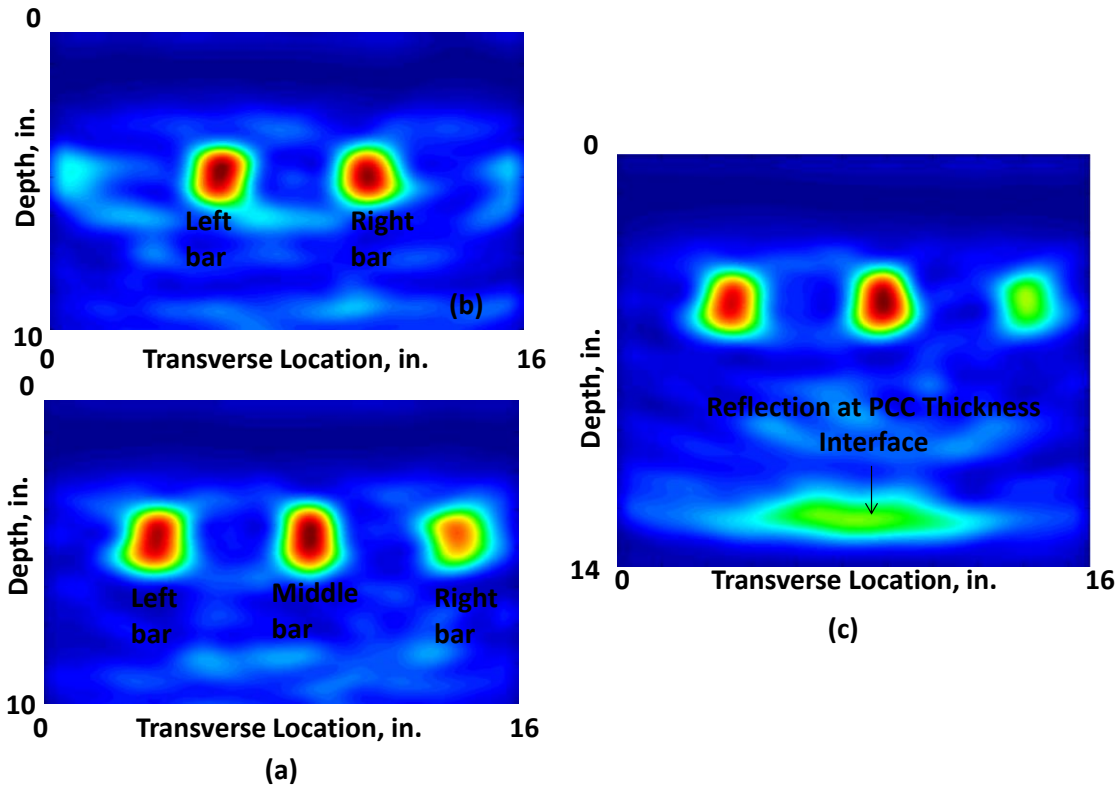

Figure 5-6. Examples of SAFT-IA reconstructions with reinforcement and PCC bottom surface reflections.

In one output method the concrete cover of each longitudinal bar in the device aperture, called "all bars", is presented where the concrete cover of the left and right bars, or left, middle, and right bars were all estimated depending on if there were 2 or 3 bars in the aperture, respectively. Another output called "shallowest bar" was used to estimate the concrete cover of only the shallowest bar within the device aperture. For example, in the "shallowest bar" method, only the middle bar would be estimated in figure 5.6b as the center of the middle high reflectivity region (longitudinal bar reflection) is shallower than the center of the high reflectivity regions (longitudinal bar reflections) on the left and right within the device aperture.

Figure 5.7 shows the ultrasonic linear array estimated concrete cover for "all bars" within the device aperture for stations 145+00 through 238+50, and for the "shallowest bar" for

all stations greater than 238+50 of northbound lane 3. Even for the "shallowest bar" method, the position of the shallowest bar is still labeled in the plot. These measurements were taken at 50 foot intervals centered 18 in. from the longitudinal joint in northbound lane 3. In northbound lane 3 the right part of the aperture is closest to the lane edge and the left part is toward the center of the lane, as is the case for all measurements.
The ultrasonic linear array measured concrete covers ranged from 2.63 in. to 5.64 in. The FHWA, GA Division provided the concrete cover specifications. It can be observed that a significant amount of concrete cover measurements were above (28%) or below (25%) the specified upper limit and lower limits of concrete cover of 4.25 in. and 3.5 in. respectively.

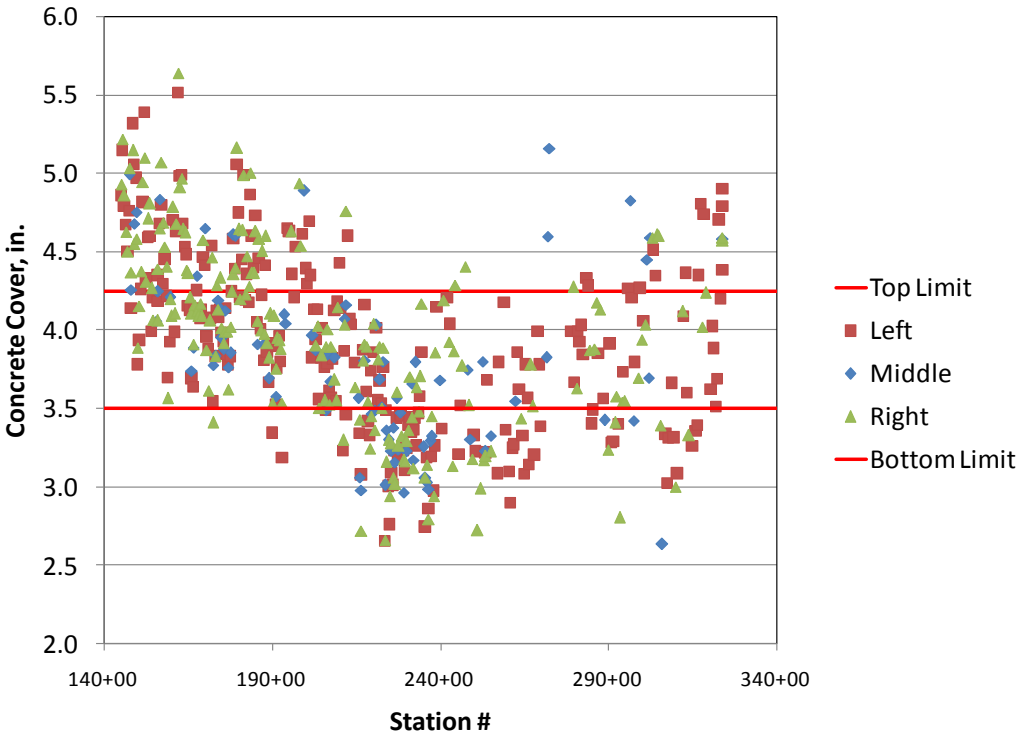

Figure 5-7. Concrete cover measurements for northbound lane 3 including all bars within the ultrasonic linear array device aperture.

Figure 5.8 shows the ultrasonic linear array measured concrete cover for "all bars" within the device aperture for stations 223+00 through 228+00 of northbound lane 3. This zoomed in view of some of the data presented in figure 5.7 shows the slight variation (in

some cases up to ~0.4 in.) in concrete cover of adjacent longitudinal bar depths even within the same longitudinal line. It can also be observed that most of the concrete cover measurements were below the specifications.

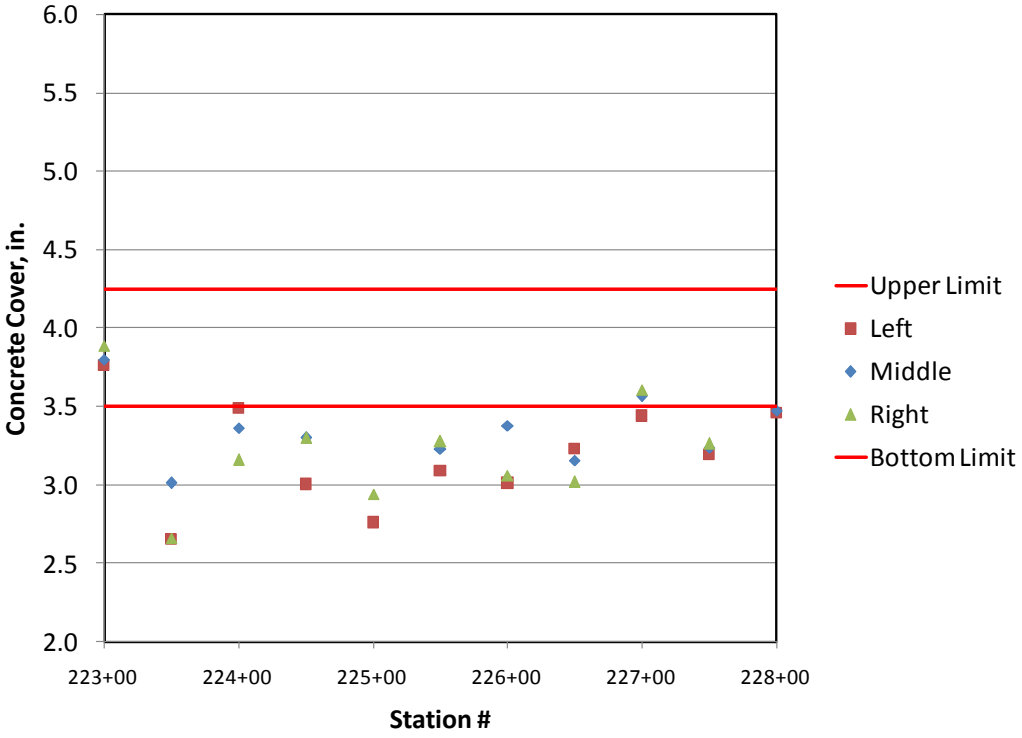

Figure 5-8. Ultrasonic linear array concrete cover "all bars" measurements for northbound lane 3 zoomed in to station numbers 223+00 through 228+00.

Figure 5.9 shows the ultrasonic linear array measured concrete cover for the "shallowest bar" from 145+00 to 250+00 and "all bars" measured in stations 250+50 through 321+50 of the northbound shoulder. It can be observed that a most of the concrete cover measurements were above (75%) the specified upper limit. Only 4% of the concrete cover measurements were below the specified concrete cover lower limit, and only 21% of the concrete cover measurements were within the specified limits. The ultrasonic linear array measured concrete covers ranged from 3.20 in. to 6.87 in.

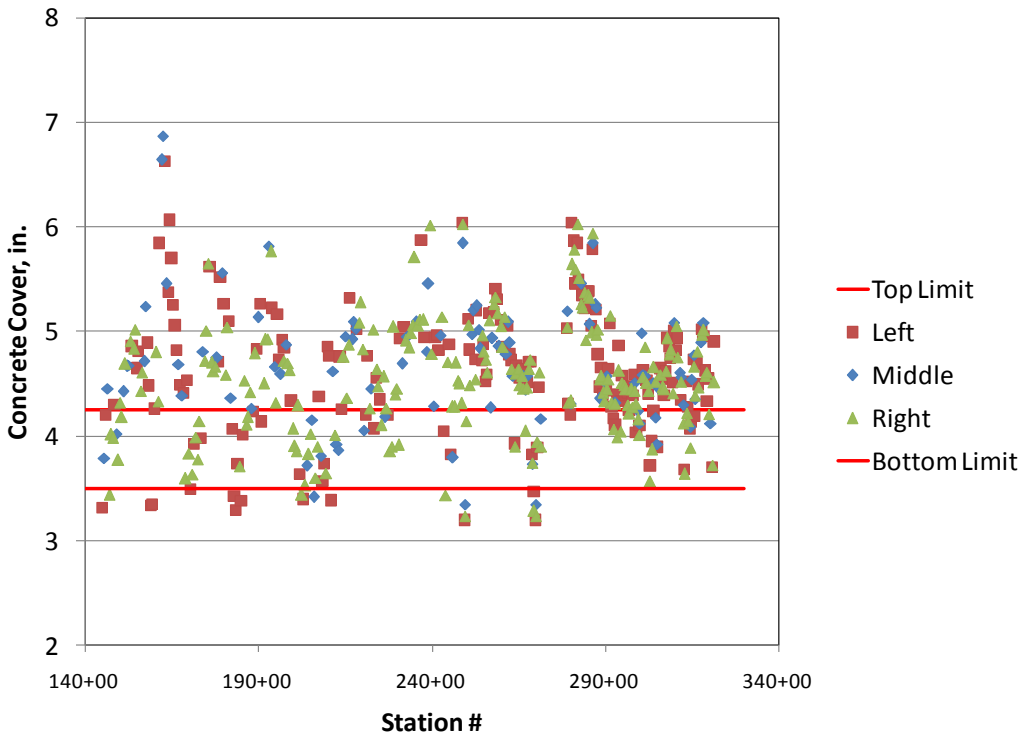

Figure 5-9. Concrete cover measurements for northbound shoulder between 145+00 and 321+50.

Figure 5.10 shows the ultrasonic linear array estimated concrete cover for the "shallowest bar" in stations 360+82 through 430+19 of the southbound lane. It can be observed that most of the concrete cover measurements were below (51%) the specified lower limit. There was also a significant amount of concrete cover measurements (18%) with below 2.5 in. of concrete cover. A small amount (16%) of the concrete cover measurements were above the specified concrete cover upper limit, and only 33% of the concrete cover measurements were within the specified limits. The ultrasonic linear array measured concrete covers ranged from 1.53 in. to 5.37 in.

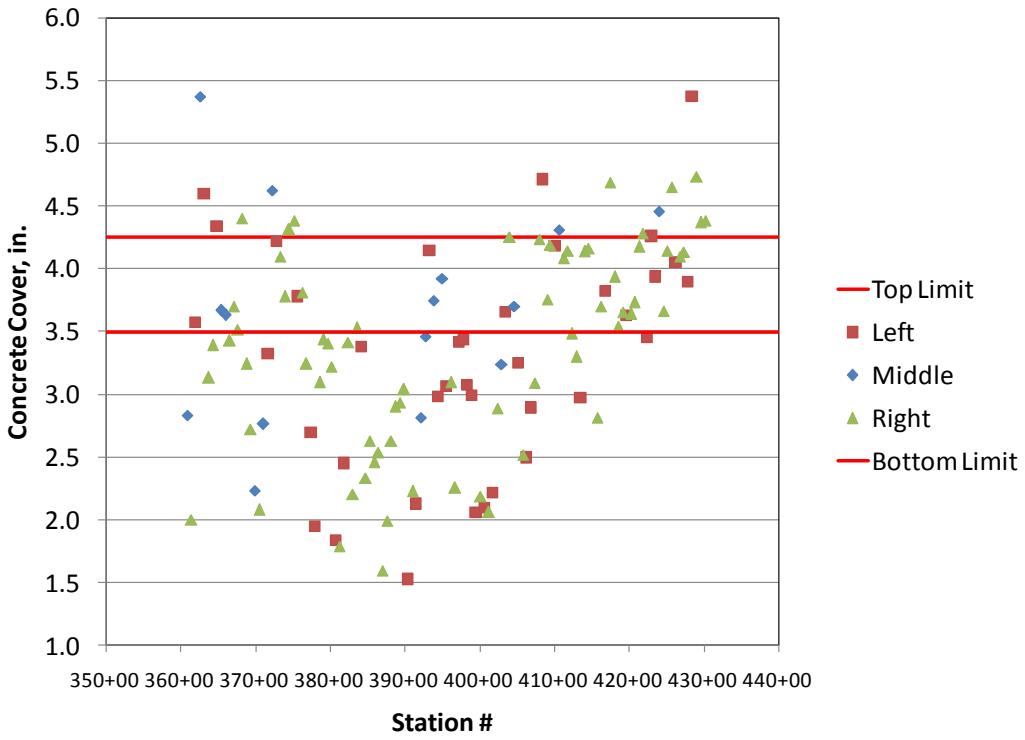

Figure 5-10. Critical bar concrete cover (southbound).

Figure 5.11 shows the ultrasonic linear array estimated thicknesses at locations along the southbound lane from stations 360+82 through 430+19. It can be observed that the ultrasonic linear array measured concrete thickness ranged from 9.20 in. to 12.60 in.

.

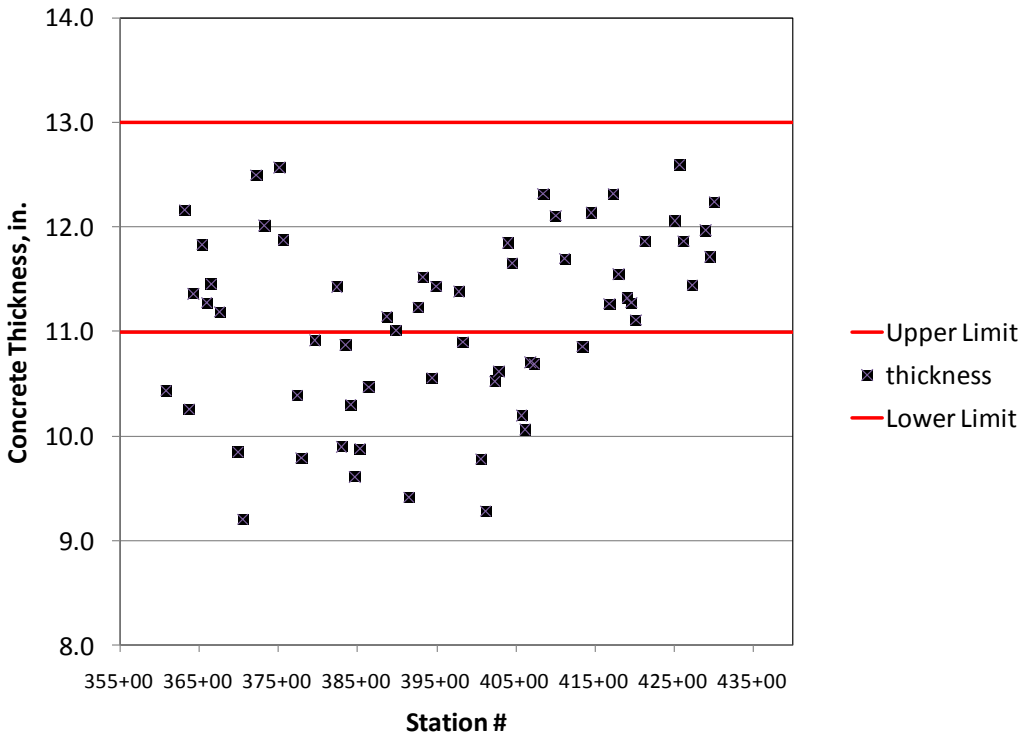

Figure 5-11. Southbound I-85 ultrasonic linear array results for concrete thickness.

Figure 5.12 shows the ultrasonic linear array versus core measured concrete cover for north and southbound core locations. It also shows a linear regression assuming a y-intercept of 0. An R-squared of 0.991 suggests that the regression explains more than 99% of the variation. It also shows that ultrasonic linear array measurements underestimate the concrete cover by a slight amount (3%) compared to core measurements. It should be noted that this is comparable with the accuracy of the core measurements themselves.

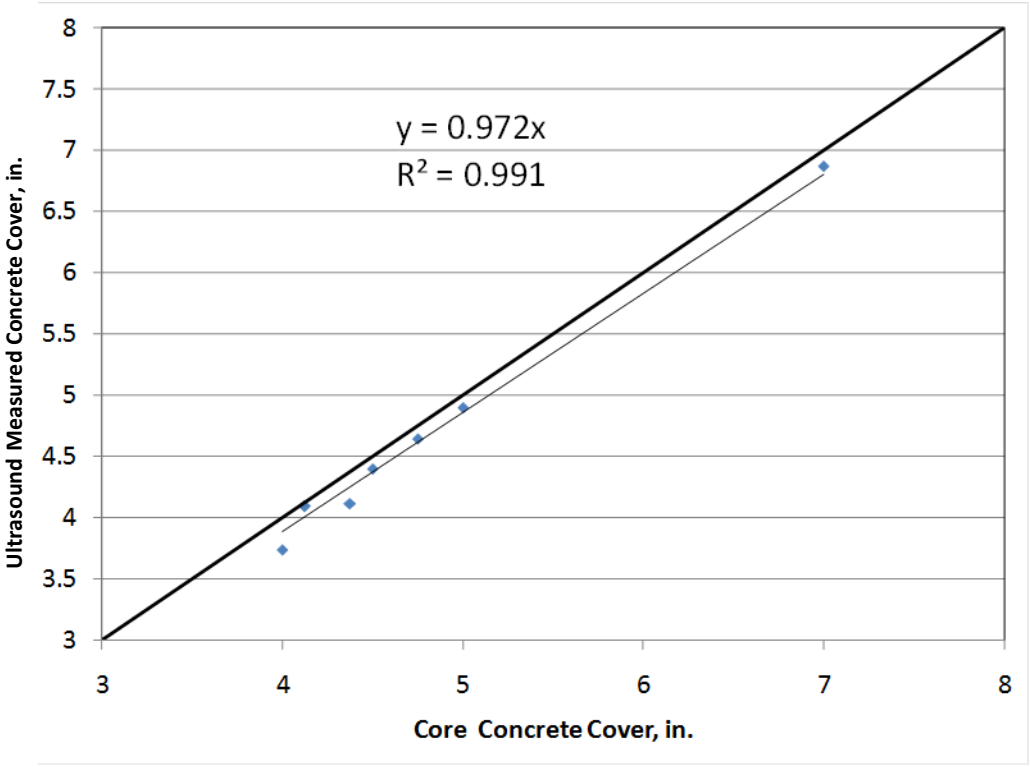

Figure 5-12. Northbound and Southbound ultrasonic linear array versus core concrete cover measurements.

A comparison of the ultrasonic linear array results with pachometer measurements conducted at the same locations of northbound lane 3 was also conducted. Figure 5.13 shows the core measured versus pachometer measured concrete cover for north and southbound I-85 data. There is a low correlation ($R^2 = 0.186$) between the core measured concrete cover and pachometer measurements.

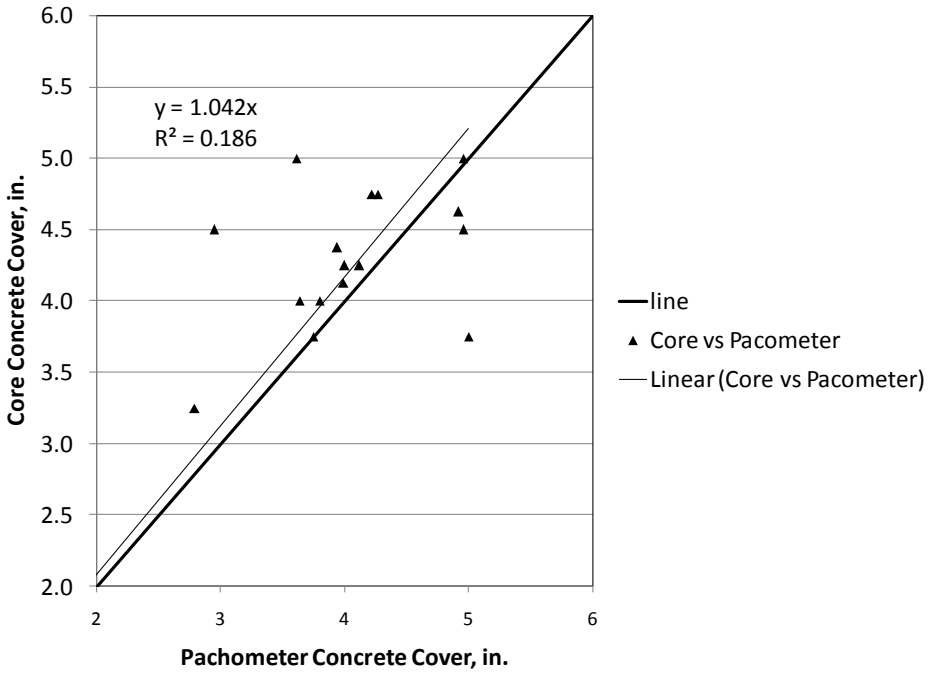

Figure 5-13. Core versus pachometer concrete cover for north and southbound I-85.

Figure 5.14 shows the ultrasonic linear array measured concrete cover versus pachometer measured concrete cover for northbound lane 3, including a linear fit assuming a y-intercept of 0. There is a very low correlation (less than 2%) between the ultrasonic linear array and pachometer measurements.

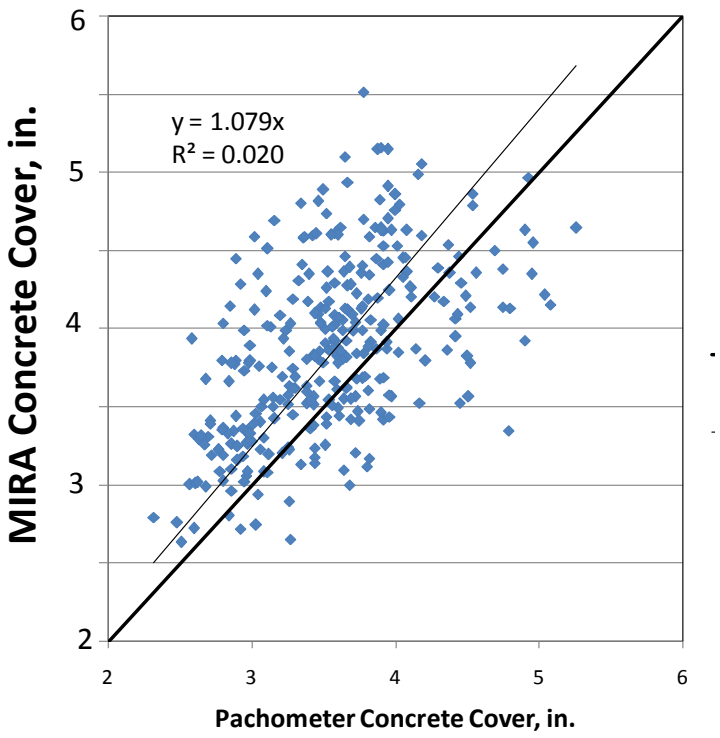

Figure 5-14. Ultrasonic linear array versus pachometer measured concrete cover for lane 3 of northbound I-85.

Testing on I-85 in Atlanta, GA was the first extensive application of the ultrasonic linear array and automated procedures for a large scale pavement evaluation. The results of over 3 miles of testing showed that the device and associated reconstruction and interpretation methods can reliably determine the depth of rebars with an accuracy significantly exceeding pachometer results. Concrete pavement thickness was also determined for the southbound I-85 sections comparing favorably to the accuracy of depth measurements determined by coring.

A summary of the results of the measured locations is given below:

- Northbound lane 3 from 145+00 to 324+00: 53 percent of the measured concrete covers were out of the range between 3.5 and 4.25 in (tolerance levels).
- The northbound shoulder/lane 4 from 145+00 to 321+50: 79 percent of the measured concrete covers where out of the range between 3.5 and 4.25 in (tolerance levels).

- The southbound shoulder/lane 4 from 360+82 to 430+19: 67 percent of the measured concrete covers were out of the range between 3.5 and 4.25 in (tolerance levels), where 18 percent were below 2.5 inches of concrete cover. Overall, concrete slab thickness showed a similar out-of-tolerance pattern with 40 percent of the measurements outside the 11 to 13 inch thickness range.

5.2 Partial Depth Bond Condition on I-94

5.2.1 Testing Procedure and Interpretation Methods

MnDOT personnel allowed for access to in-service highway that was recently rehabilitated at the transverse joints using partial depth repairs. Chaining (the state of practice NDT method for this type of diagnostics) was carried out by experienced MnDOT personnel to identify general areas where there was potential debonding. Ultrasonic linear array scans were also taken with corresponding core verification.

Figure 5.15 shows an example SAFT-IA reconstruction taken at a properly bonded partial depth repair location showing a typical backwall reflection at the interface between the concrete and base as well as some additional lower intensity reflection at shallower depths where the new and old concrete interface is located. These lower intensity reflections are caused by the presence of two different concrete layers with slightly different acoustic impedance as well as coarse aggregate. This was determined through the consistent appearance of moderate intensity reflections in SAFT-IA reconstructions at the depth of the repair material layer, even in cases where cores verified a proper bond.

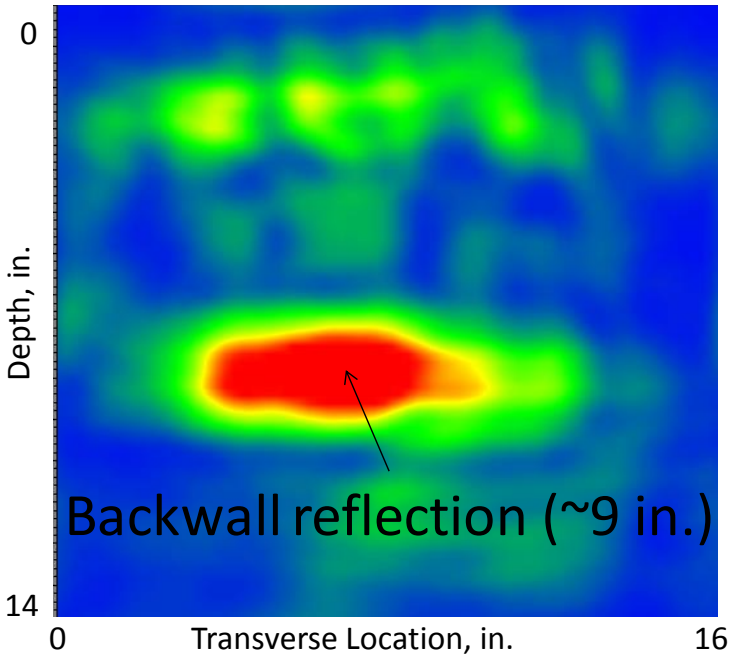

Figure 5-15. Example SAFT-IA reconstruction taken at a partial depth repair location where no metal reinforcements are present.

Metal inclusions can also cause reflections of the shear waves. Figure 5.16 shows an example SAFT-IA reconstruction taken at transverse joint indicating the presence of dowels. The high intensity reflections near 4 in. (~100 mm) indicate the presence of dowels. However since the SAFT-IA reconstruction uses multiple measurement pairs, the presence of the backwall reflection between the concrete and base is still visible.

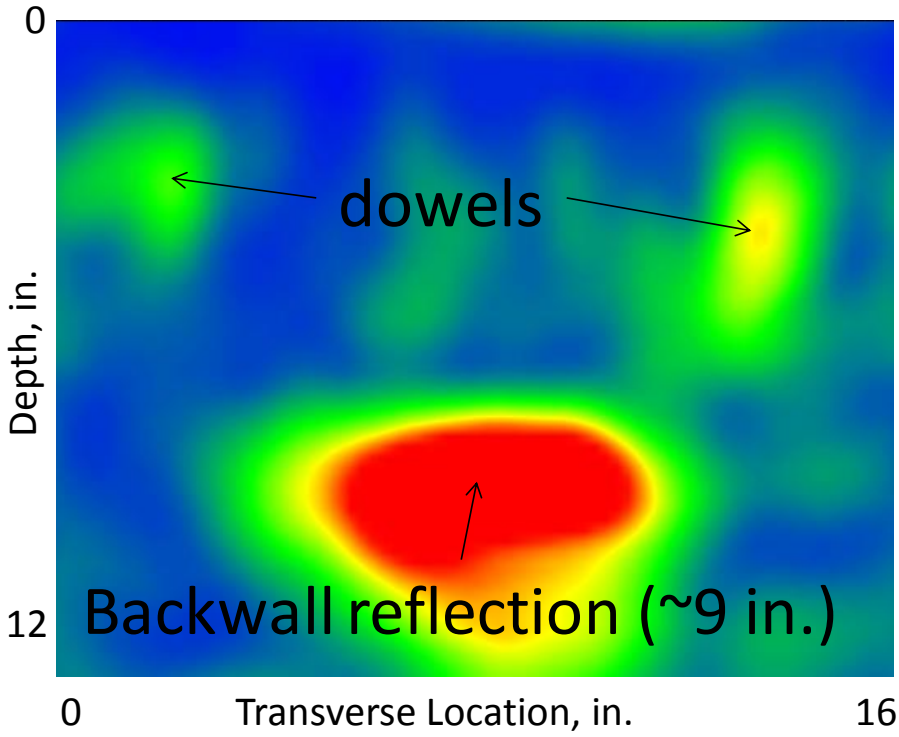

Figure 5-16. SAFT-IA reconstruction taken at a partial depth repair near a transverse joint where dowels are present.

The SAFT-IA reconstruction shown in figures 5.15 and 5.16 are the type of reconstructions that indicate a sound concrete condition with high reflectivity areas only associated with locations of metal dowels (if present) and the depth of the concrete/base interface. Variation from these types of SAFT-IA reconstructions can indicate the presence of subsurface damage.

One type of variation from a typical SAFT-IA reconstruction that indicates subsurface damage is called shadowing. Shadowing refers to the absence of a high intensity of reflection at a location where there is a change in acoustic impedance as explained in more detail in section 4.1.5. The depth of the interface between the top concrete layer and base is primarily used for the shadowing analysis and this interface will be referred to as the "backwall" in this study. Since there is a large difference in acoustic impedance between the concrete layer and the base layer a high intensity of reflection at this planar

depth should be expected. However, if there is an obstruction at a shallower depth, shear waves will either be reflected back to the surface or attenuate before they penetrate to the depth of the backwall. Therefore, since there are 45 transmitting and receiving pairs in each measurement, it can be assumed that there is a planar obstruction such as debonded partial depth repair or deteriorated concrete if a low intensity of reflection is observed at the backwall depth within a SAFT-IA reconstruction. This type of analysis is useful for diagnosing the presence or extent of subsurface damage at concrete pavement joints and/or evaluating the quality of rehabilitation construction.

5.2.2 Results and Forensic Validation

An example partial depth repair section where verification cores were taken illustrates the capabilities of SAFT-IA analysis for quality assurance of partial depth repair bond with existing concrete. Figure 5.17 shows a series of MIRA scans (positions 1 through 12) taken at an approximately 2 ft. by 2 ft. partial depth repair located at a transverse joint. The left side of the partial depth repair (shown in) figure 5 is approximately 3 ft from the truck lane fog line.

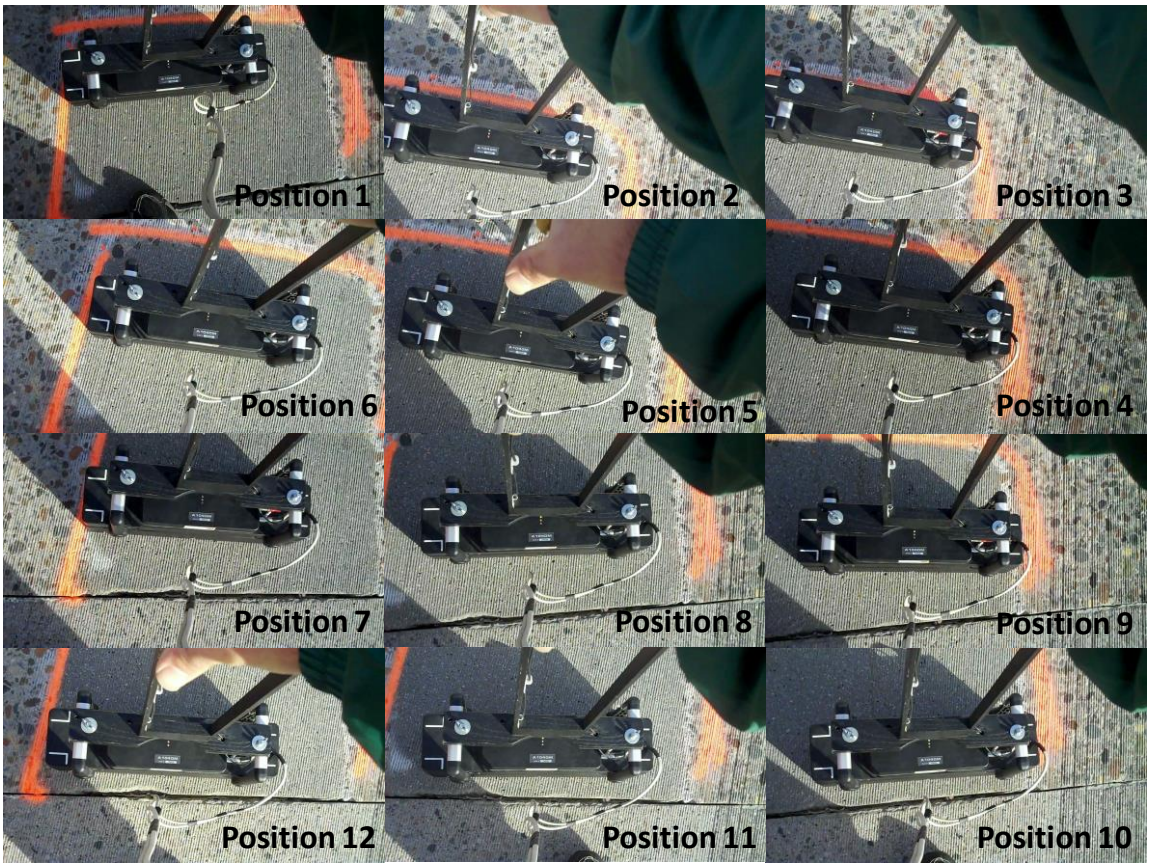

Figure 5-17. Twelve MIRA scan locations taken at the example partial depth repair.

Each of these scans resulted in SAFT-IA reconstruction results associated with the condition of the concrete below (shown in Figure 5.18). It can be observed from Figure 5.18 that a large majority of these SAFT-IA reconstructions experience shadowing of the backwall reflection at about 9 in. (~225 mm). The SAFT-IA reconstructions indicating debonding were located on the lower right corner near the joint, while the sound concrete conditions were located away from the joint on the upper left area away from the joint. Chain drag results indicated general debonding of the repair but could not differentiate between bond or no bond within the repair area.

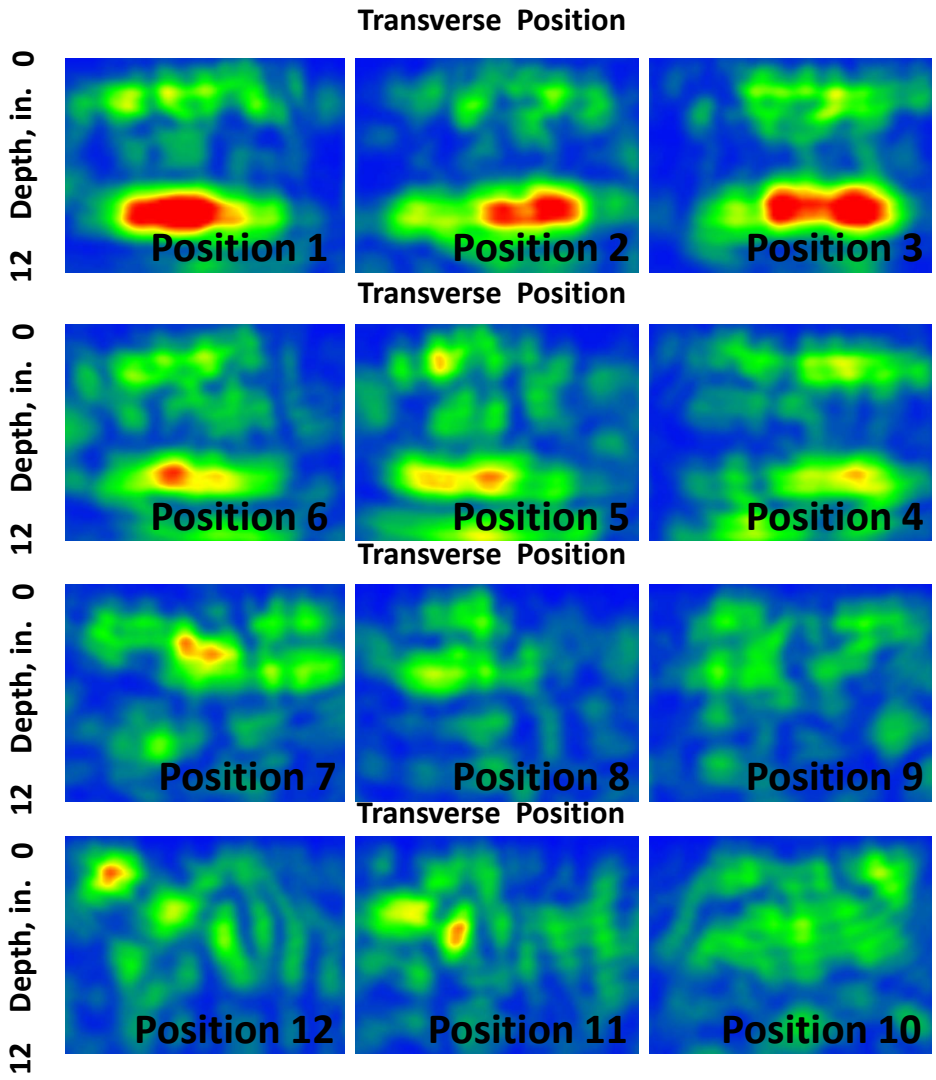

Figure 5-18. SAFT-IA reconstructions associated with the 12 MIRA scan positions shown above (depth of each scan: 300 mm).

A core was taken at a location within the partial depth repair (towards the fog line and away from the transverse joint) as shown in Figure 5.19. The core at this location showed a proper bond between the partial depth repair and the existing concrete upon inspection of the cross-section as shown in Figure 5.19 on the right. This core result confirmed the SAFT-IA reconstructions in this vicinity where a strong backwall reflection indicated a proper bond. This core did not agree with the chain drag results which showed general debonding of the partial depth repair.

Figure 5-19. Core location (left) and result showing properly bonded partial depth repair.

Figure 5.20 shows the positions in the vicinity of the core with position 1 (left) and position 6 (right) SAFT-IA reconstructions indicating a strong bond. It can be observed that these SAFT-IA reconstructions are similar to the example SAFT-IA reconstruction shown in Figure 5.15 which indicates a proper partial depth repair bond. The clear backwall reflection at the concrete and base interface gives the indication of a proper partial depth repair bond above.

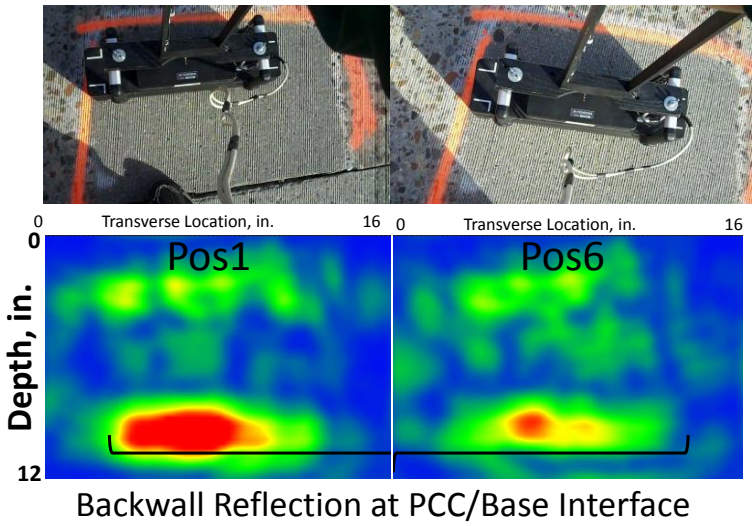

Figure 5-20. SAFT-IA reconstructions in the location where the first core was taken with a strong backwall reflection indicating a proper bond between of the partial depth repair.

Locations where the backwall reflection experienced clear shadowing (positions 8, 9, 10, and 11) were inspected further with MIRA measurements to pinpoint a location where the core would verify the debonding within this general vicinity (positions 9 and 10).

Figure 5.21 shows the position 9 (left) and position 10 (right) scan locations and associated SAFT-IA reconstructions. It can be observed that these SAFT-IA reconstructions are dissimilar to the type of SAFT-IA reconstruction that should be expected for a properly bonded partial depth repair. In these SAFT-IA reconstructions the backwall reflection at the depth of the interface between the existing concrete and base layer is not present. This is an indication that the un-bonded condition at the partial depth repair interface obstructed the shear waves from through transmission to the depth of the concrete.

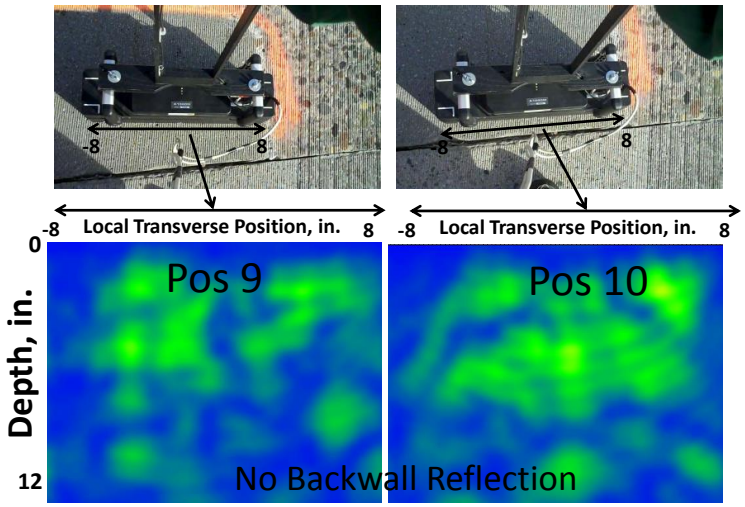

Figure 5-21. SAFT-IA reconstruction locations indicating a poor bond between the partial depth repair and existing concrete.

The core taken using this pinpointed location is shown in figure 5.22 (b). It can be observed that the partial depth repair is de-bonded, especially when compared to the properly bonded location core shown in figure 5.22(a). This validated the ultrasonic tomography diagnosis of an improperly bonded partial depth repair.

Figure 5-22. Cores taken at the area (B) towards the centerline near the transverse joint indicating an improperly bonded partial depth repair in comparison to (A) the properly bonded repair.

A similar process was used to pinpoint a debonded location in other joint locations where SAFT-IA analysis indicated debonding. Another core verifying debonding of the partial depth repair as indicated by SAFT-IA diagnosis is shown in Figure 5.23.

Figure 5-23. Core showing debonding of the partial depth repair.

5.3 MnROAD Joint Evaluation

5.3.1 Initial Ultrasound Analysis and Forensics

A field trial at the Minnesota Road Research Facility (MnROAD) was conducted to determine the subsurface condition near transverse joints including the presence and/or extent of potential flaws. Multiple scans were taken at various transverse joints in an initial screening. Analysis of the SAFT-IA reconstructions at one joint location indicated potential flaws. An example SAFT-IA reconstruction at a right wheel path is shown on the left in figure 5.24. In this, and other locations around the right wheel path, the high intensity of reflection areas corresponded to dowel locations and the depth of the concrete-base interface as should be expected for undamaged concrete. Analysis of the remaining portion of the joint indicated a much different subsurface condition. SAFT-IA reconstructions at the center of the joint, as well as toward the centerline of the joint, indicated damage. Instead of strictly reflections at the dowels and concrete thickness, there was an uneven reflectivity region at a shallower depth that should not be expected. This shallow and uneven reflection indicated deterioration of the concrete at the interface with the base.

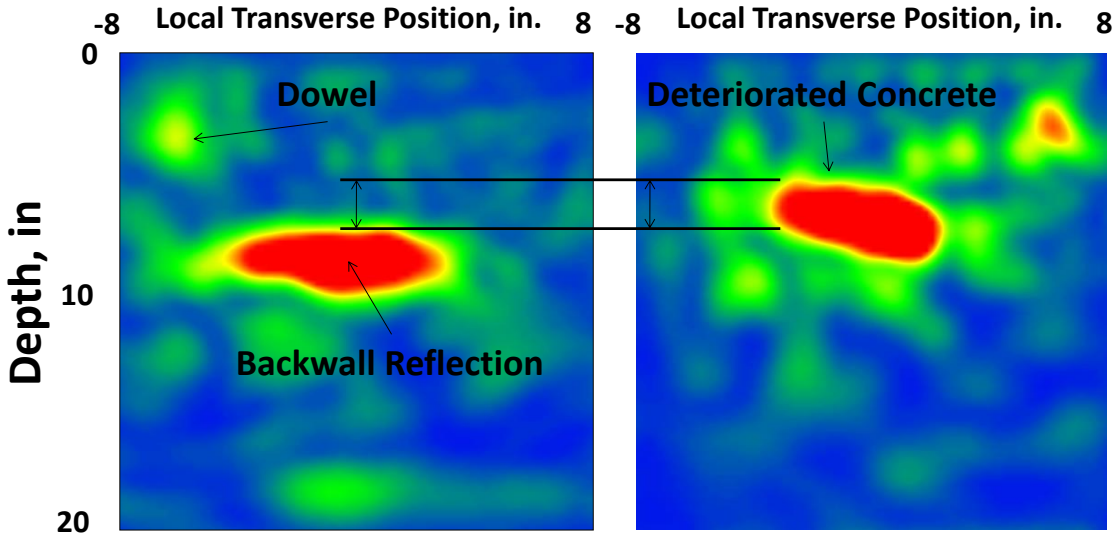

Figure 5-24. MIRA SAFT-IA reconstruction locations in suspected sound (left SAFT-IA reconstruction) and deteriorating (right SAFT-IA reconstruction) conditions.

MnDOT personnel subsequently took a 12 ft by 3 ft full-depth concrete sample from along the transverse joint to validate the MIRA SAFT-IA reconstruction diagnosis. As shown in Figure 5.25, the sample was flipped so that the interface between the concrete and base is shown at the top. It can be observed that the underside of the concrete near the right wheel path is in relatively good condition as was diagnosed by SAFT-IA reconstructions. The underside of the concrete near the base in the samples at the middle of the joint and at the centerline show significant deterioration. This verified the nondestructive diagnosis of deterioration using SAFT-IA reconstruction prior to forensic verification.

Figure 5-25. Forensic sample sections used to verify the concrete condition on the underside at various locations near the transverse joint.

5.3.2 Blind Test Comparison with other Nondestructive Testing Methods

After the initial screening described above, a blind test evaluation of the capabilities of various nondestructive testing techniques in determining the extent of the concrete joint deterioration was scheduled. In this study, four different nondestructive testing techniques were used to diagnose deterioration. The evaluated methods included well established techniques such as ground penetrating radar (GPR), rod sounding, and chaining as well as the ultrasonic linear array methods described in this thesis (MIRA). It

should be noted that all indications of subsurface distress were not marked on the pavement to ensure blind test results for all methods. The results for all four techniques were submitted to MnROAD independently. Subsequent forensic activities were conducted to evaluate the accuracy of each of the methods.

The testing was conducted at the bypass along westbound I-94 adjacent to the MnROAD Mainline Test Section in MnDOT District 3. I-94 in this area is a four lane divided concrete roadway with a nominal thickness of 9 inches consisting of 27 foot skewed joints. The pavement, built in 1974, had exhibited very few cracked panels but high severity faulting causing poor ride. Falling weight deflectometer (FWD) measurements showed the joints to have low joint efficiency. Two transverse joints of the MnROAD bypass were evaluated in this study using nondestructive testing. The east most joint located toward the beginning of the bypass is referred to as Joint 1 in this study while the west most joint is referred to as Joint 2. The area was evaluated along the entire transverse joint extending to 18 inches on both sides of the joints.

MnDOT personnel used an "S" type motion to drag the chain along the joint and determine where a hollow sounding response was observed. A heavy steel bar was also used to sound the pavement with the same MnDOT personnel listening for a hollow response. Since the MnDOT operator in this study observed a better sound penetration with the rod sounding technique as compared to the chaining, this method was used to map areas of delamination. The "X" marks from the chain drag and map of the deteriorated areas from the rod sounding were marked into notes on-site, and then submitted using an electronic diagram before forensic evaluation.

In this study a MnDOT owned and operated 2.6 GHz ground-coupled antenna was used. A grid was painted above the concrete joints, with 2 foot intervals marked transversely. The 2 ft points are marked with dashed lines at the top of the image shown in figure 5.26. The first mark was 4 inches from the right edge of concrete while the last mark was 4 inches from the left edge of concrete.

The data obtained from the ultrasonic linear array measurements were processed using the Synthetic Aperture Focusing Technique (SAFT) reconstruction methods described in this thesis inclusing SAFT-Pan and SAFT 3D reconstructions allowing for detailed reconstruction of subsurface features. An example measurement from this study can be observed in figure 5.26.

Figure 5-26. Example ultrasonic scan.

Figure 5.27 shows four approximately 6 ft. SAFT panoramic reconstructions each resulting from overlapping SAFT-IA reconstructions taken in 4 inch step sizes on joint 2 after they have been fused together. The four SAFT panoramic reconstructions were centered (from top to bottom in Figure 5.28) at 16 in., 10 in., 8 in, and 3 in. away from the joint at the same location along the leave slab of passing lane joint 2.

On the left side of each of the scans the high intensity reflections can be observed at the approximate depth of the pavement (~9 in.) indicating relatively sound concrete condition. Conversely, shallower high intensity reflections can be observed at the right side of the SAFT panoramic. These shallow reflections were used to diagnose delamination. It can be observed that the shallow high intensity reflections extend further left as they approach the joint. The filled orange squares at the top of each reconstruction

indicate the delamination crack initiation. This trend of extended delamination closer to the joints was observed at multiple locations. This type of analysis was useful when mapping the extent and severity of the deterioration prior to the forensic evaluation. By creating a continuous reflection at the depth of the PCC allowing for deterioration analysis with an effectively wider aperture, distress trends along the joints tested in this study could be evaluated.

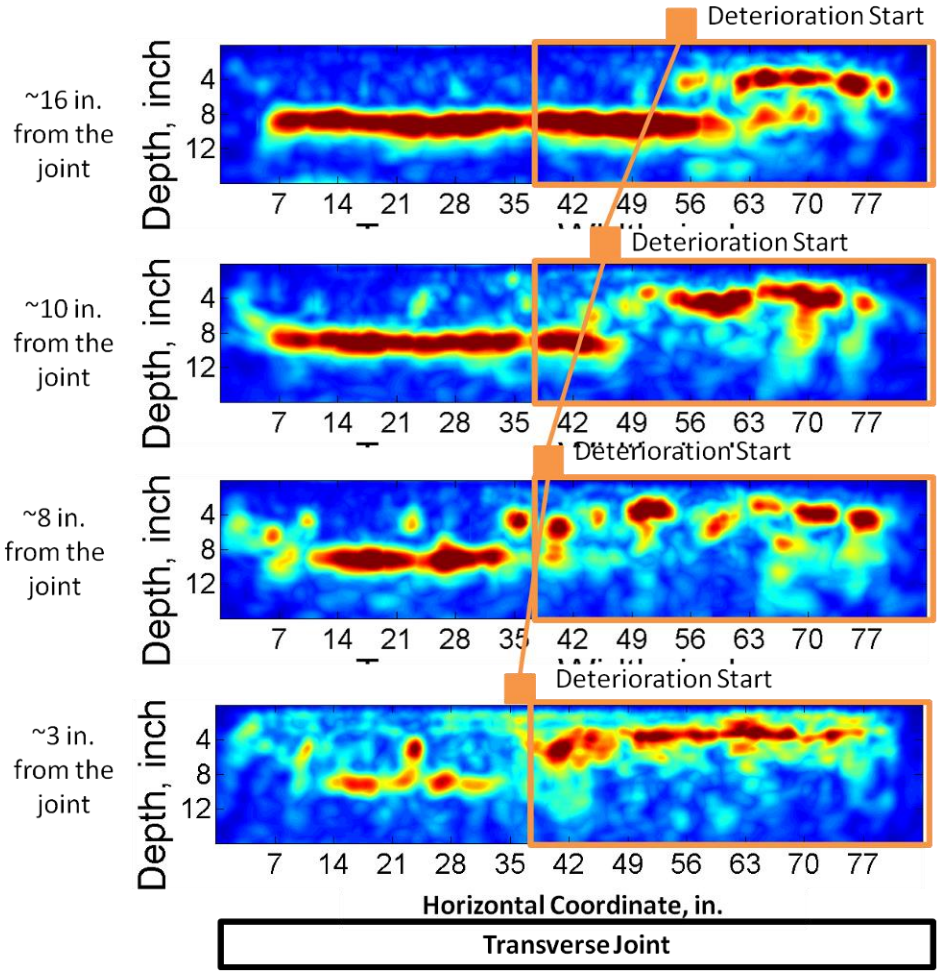

Figure 5-27. SAFT panoramic reconstructions from top to bottom at 16 in., 10 in., 8 in., and 3 in. from the joint.

Figure 5.28 shows the delamination in this area as viewed from the SAFT 3D reconstruction. Similar to the SAFT panoramic reconstruction shown in figure 5.27, a majority of the high intensity shallow reflections indicating delamination can be observed

on the right side. On the right side of figure 5.28, the high intensity reflections can be observed along the depth of the dowels including locations between the dowels. This type of reflection indicates a horizontal plane of delamination. Using the SAFT 3D reconstructions the extent of delamination can be observed in both lateral and depth directions by looking at different angles of the SAFT 3D reconstruction. This type of SAFT 3D reconstruction can be useful for getting relational information about the high intensity reflections to determine if the reflection is caused by an as designed inclusion or damaged concrete in the vicinity.

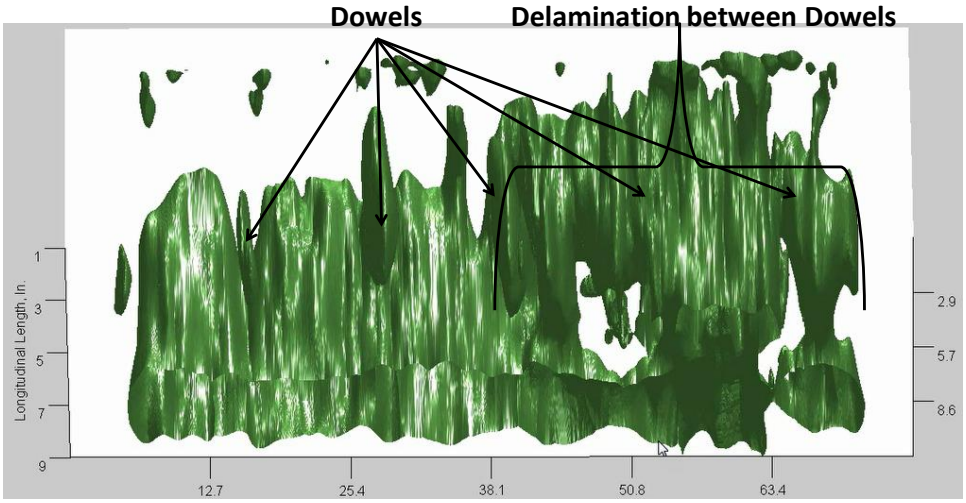

Figure 5-28. SAFT 3D reconstruction indicating a delaminated condition in the joint #2 passing lane leave slab.

5.3.2.1 Results Summary

A summary of testing results for the conventional sounding methods (chain drag and rod sounding) as well as the ultrasonic array technology is presented in figure 5.29. The chain drag-detected deterioration is denoted with an "X." The brown markings shown in the center of figure 5.29 show the boarder of rod sounding-detected deterioration. The ultrasound array deterioration is marked using darker shades of gray to indicate deteriorated conditions. The legend in figure 5.29 shows the associated markings. GPR testing did not result in a mapped evaluation of the condition, so the results are given in Table 5.1. Also, since the analysis was based on intensity of the dowel reflection, any information past the end of the dowels or below the dowels was not available.

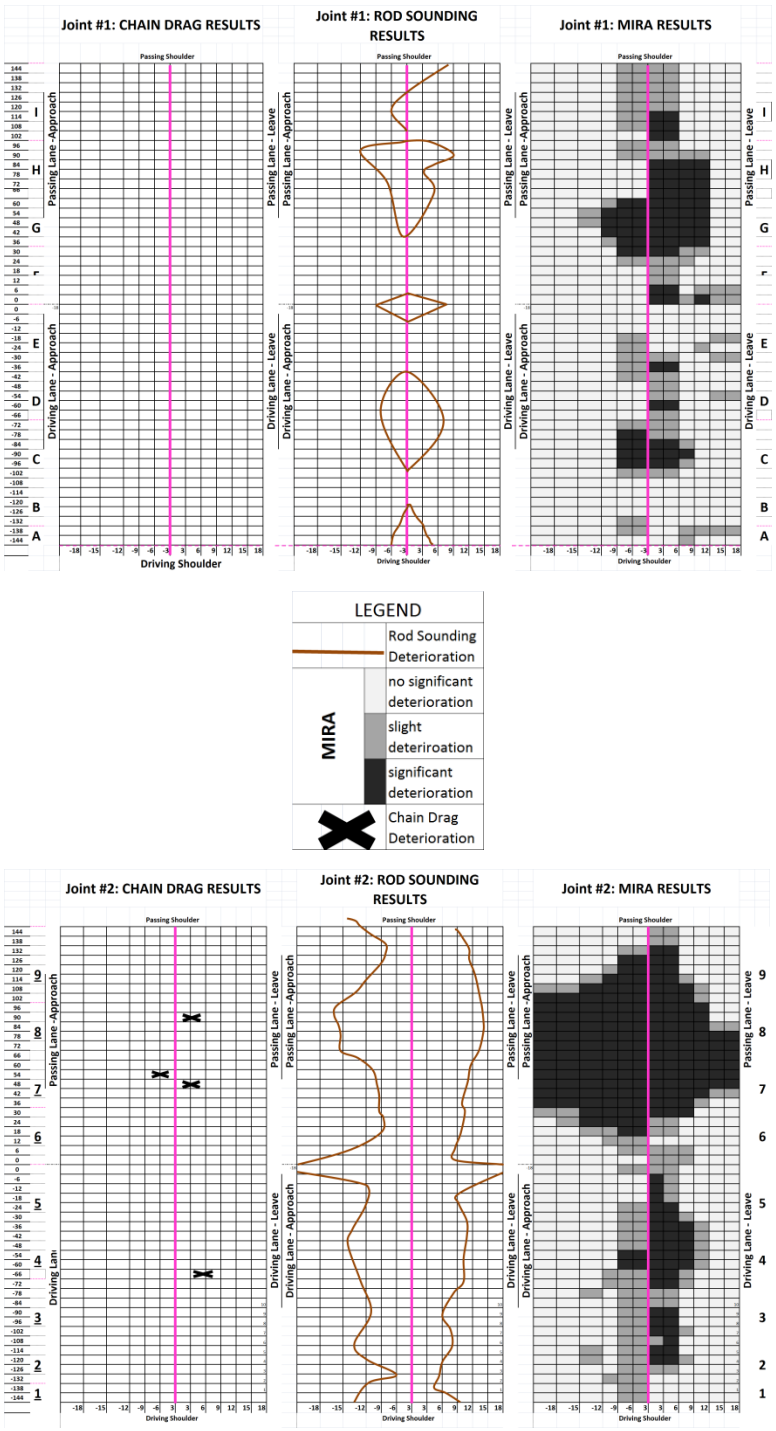

Figure 5-29. Conventional sounding and ultrasonic array technology (MIRA) summary of test results (Joint 1 is shown on the top and Joint 2 is shown on the bottom).

Table 5-1. GPR general test results.

Location	GPR Evaluation
Joint 1: 4 in. east of joint	All dowels visible in both lanes, bars near the center of roadway in both lanes visible indicating possible corrosion or socketing
Joint 1: Directly over joint	Only one dowel clearly visible in right lane, indicating probable corrosion and/or socketing. Dowels in passing lane barely visible indicating probable corrosion and/or socketing, but not quite as severe as in driving lane.
Joint 1: 4 in. west of joint	All dowels visible in both lanes, bars near center of roadway somewhat less visible indicating possible corrosion and/or socketing.
Joint 2: 4 in. east of joint	Dowel bars in truck lane are present and look ok. Dowels in passing lane are significantly less visible, indicating probable corrosion and/or socketing.
Joint 2: Directly over joint	Only one dowel is slightly visible in truck lane. Dowels in passing lane not visible; mid–depth deterioration and/or voids are apparent – particularly in the left-most 8 feet of the joint.
Joint 2: 4 in. west of joint	All dowels visible, but dowels in passing lane are less clear indicating possible corrosion or socketing.

Comparison of the outputs from each technique shows that chain dragging and GPR resulted in a limited amount of data as compared to the coverage of rod sounding and ultrasonic array technology. Moreover, there were inconsistencies in the joint assessment among the techniques. There were some locations where all four methods indicated the presence of deterioration. For example, the presence of subsurface distress was detected by each method in the passing lane of joint 2, although to various extents. At the same time, there are various locations, especially at joint 1, where there was disagreement in joint deterioration assessments. To resolve these discrepancies, forensic activities were conducted.

5.3.2.2 Forensic Evaluation

Forensic analysis was conducted after nondestructive testing results were submitted at two transverse joint locations. The saw cuts were made 18 in. away from the transverse joint on both the approach and leave slab creating a 3 ft. wide (longitudinally) trench. Additional saw cuts were made in the longitudinal direction resulting in 1 approximately 1 ft by 3 ft slab, and 8 approximately 3 ft by 3 ft concrete slabs at each joint. The slabs of joint 1 were labeled A through I in the transverse direction from driving lane to passing lane with an underline denoted on the approach slab side. The slabs were similarly labeled 1 through 9 in joint 2.

To evaluate the presence and extent of deterioration of the underside of the concrete initiated at the joints the slabs were flipped upside-down. This type of deterioration initiated at the joint is referred to as "tenting" herein, where the amount of deteriorated concrete increases with depth at the transverse joint. Figure 5.30 gives an example upside-down slab location where significant tenting can be observed at joint 2, slab #2.

Figure 5-30. Example "tenting" distress observed at joint 2, in both approach and leave slab #2 as viewed from the south side of the slab.

Spalling and PCC cracking information could be gathered at each of the saw cut interface locations of each of the slabs provided. This observed distress was generally horizontal and initiated at uncut tie wires of the dowel baskets and is referred to as "delamination" herein. Additional cores were taken to determine the amount of delamination within locations where no side surface was visible and differing nondestructive testing results were submitted. Figure 5.31 shows example locations where delamination can be observed. An interface where the crack has not propagated a significant distance can be observed at joint 2, slab #8, on the right side of figure 5.31. A location where the crack has initiated at the tie wire and propagated to the joint can be observed on the bottom left of figure 6.7 showing joint 2, slab #6, on the south side. The top, left corner of figure 6.7 shows delamination initiated at the tie wire that has propagated to the joint as well as to 18 inches away from the joint. It can also be observed that the crack at this pictured location (joint 2, slab #8) is deteriorating and widening.

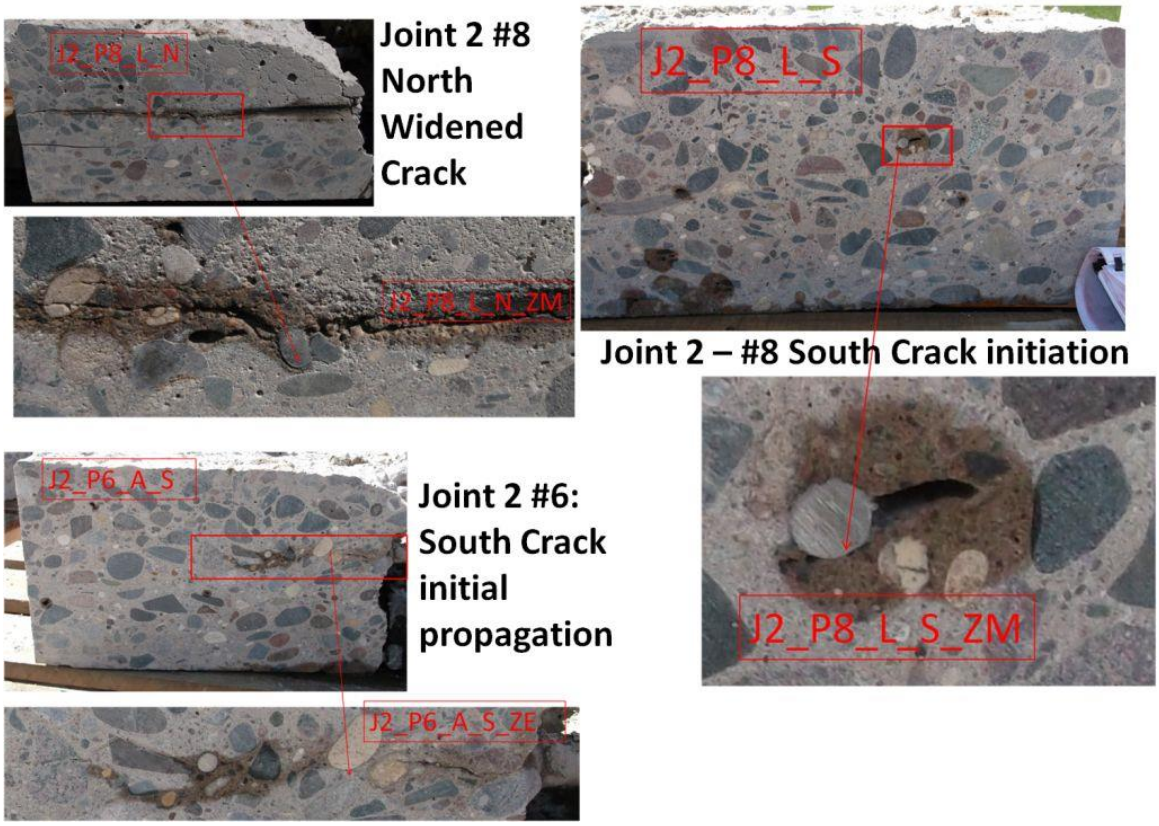

Figure 5-31. Example delamination observations at various locations showing the different extents of observed delamination.

5.3.2.3 *Comparison of Results*

Comparison of ultrasonic array technology with traditional methods, and subsequent forensics showed the ultrasonic method with associated signal interpretation tools to be the most proficient at identifying the extent and depth of subsurface deterioration. Rod sounding was found to be the best alternative to ultrasound as it correlated fairly well with the "tenting" results near the joint, although it did not detect a significant portion of the delamination, especially at greater depths and further away from the joint.

While ground coupled GPR and chaining were able to detect several significantly deteriorated areas, a detailed map of the tested area could not be provided and a significant amount of the distresses confirmed by forensics was not identified by these methods. Due to the dependence of electromagnetic waves on changes in dielectric

properties to gather information, GPR is more sensitive to metal or water inclusions as compared to layer boundaries such as delamination or the interface between the concrete and the base. It was also indicated by the GPR operator that the dry conditions might have contributed to the lack of detailed information at deteriorated areas. In the case of chaining, the operator indicated that the impact was not as great as the rod sounding making it more difficult to determine flaws at greater depths.

Ultrasonic array technology and rod sounding were the only methods able to map the general location of deterioration, while the ultrasonic array method showed the most extensive and accurate results including the depth of the deterioration. Forensic activities identified that the deterioration covered the extent of the tested area at both approach and leave slabs of the passing lane of Joint #2. Comparing this result to those submitted prior to forensic activities showed that ultrasonic array technology blind testing was the only method that indicated deterioration to the extent of the tested area at these locations. There were also other cases where forensics was used to resolve discrepancies between methods as detailed in the section below. The following section also uses forensic results to verify that the depth of the distresses identified by ultrasonic array analysis in the blind test.

There were some situations where there was disagreement between the various NDT methods. The forensic results at some of these locations are presented to enable objective evaluation of the tested techniques. Ultrasonic array technology was the only technique that showed significant deterioration away from the joint. The results of forensics confirm this assessment. Figure 5.32 presents the ultrasound array technology analysis results along with associated forensics at a portion of the leave slab of joint #2. The figure shows the starting and stopping point of the ultrasonic array technology measurements for the given section (top), the SAFT panoramic reconstruction (middle), as well as the forensic verification (bottom). The orange box around the SAFT panoramic reconstruction corresponds to the orange box around the cross section of the pavement at that scanned location as revealed by trenching the joint.

It can be observed that the mid-depth of the high intensity reflection on the left of the SAFT panoramic is approximately 9 inches, which corresponds to the PCC slab thickness and indicates sound concrete. Forensics confirms this assessment as shown on the left side of the interface in figure 5.32. A shallower high intensity reflection can be observed on the right side of the SAFT panoramic reconstruction. The mid-depth of this reflection is approximately at 4.5 in. This corresponds with the depth of the delamination that can be observed at about 4.5 in. depth on the right side of the forensic interface. Although, as can be observed by figure 5.32, this is a fairly straight forward diagnosis using ultrasonic array technology, the other techniques were not able to identify this delamination (see figure 5.29). Similarly, only ultrasonic array analysis diagnosed delamination away from the joint in the approach slab of joint #2. Figure 5.33 shows similar results where the depth of the delamination diagnosis corresponds to the depth of the delamination verified by forensics.

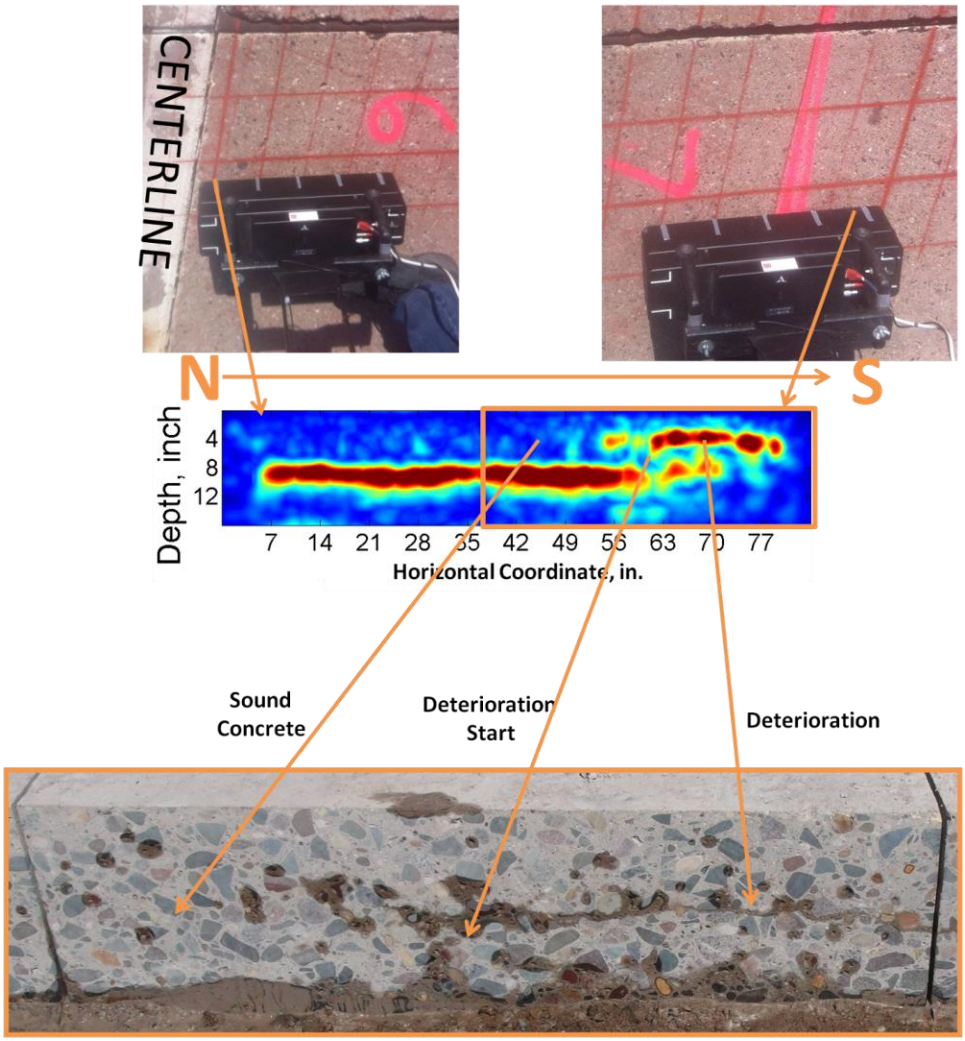

Figure 5-32. SAFT Panoramic reconstruction and comparison with the actual delamination crack path at 18 in. from Joint #2 in the leave slab.

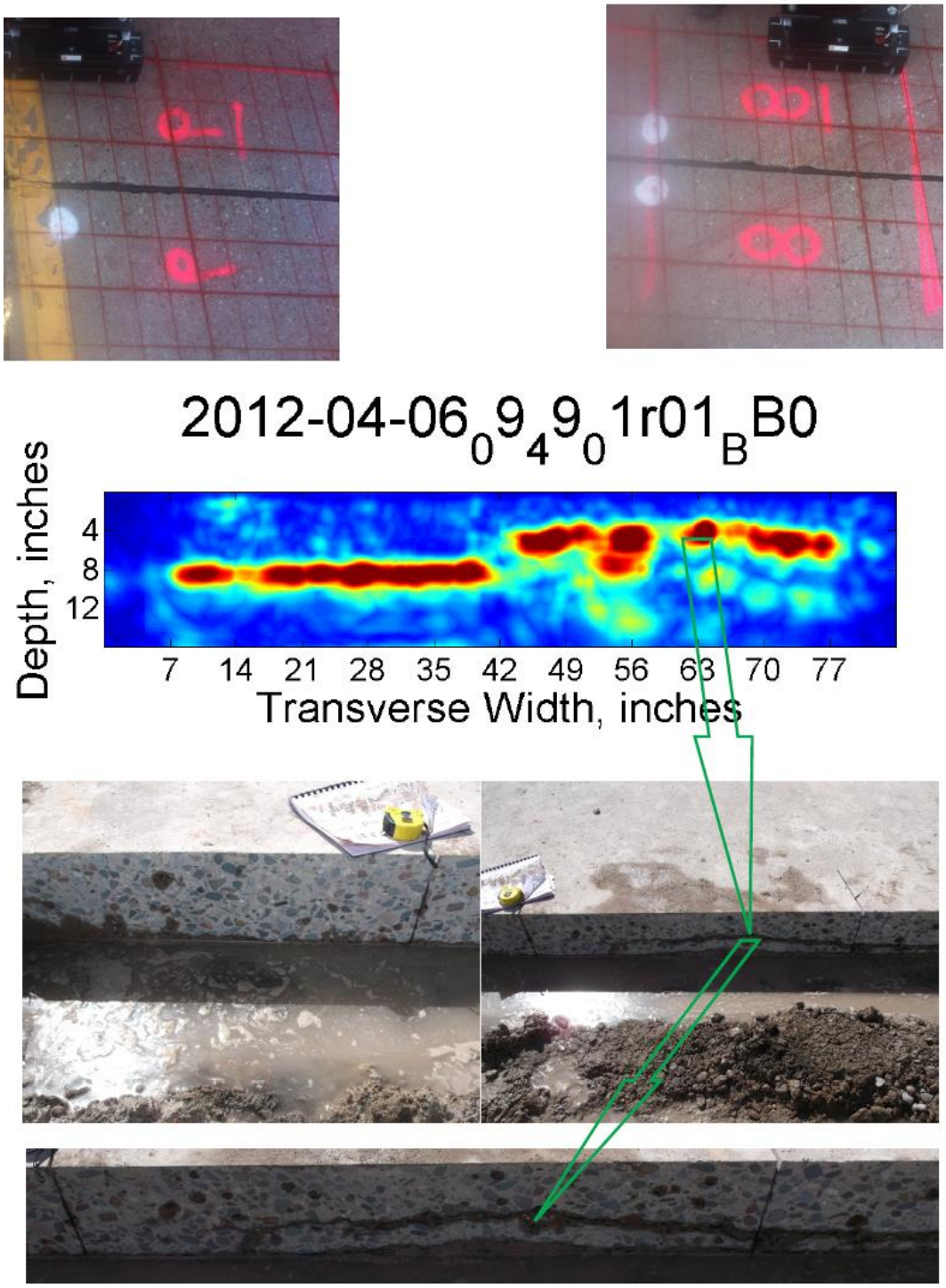

Figure 5-33. SAFT Panoramic reconstruction and comparison with the actual delamination crack path at 18 in. from Joint #2 in the approach slab.

At some of the locations, the SAFT-based analysis tools and interpretation methods showed subsurface deterioration where the conventional methods did not, and were located where forensic information was not initially available. In a couple of these locations cores were taken to resolve the discrepancies. The cores taken in these examples confirmed the ultrasonic SAFT-based diagnosis of delamination. Figures 5.34 through 5.36 illustrate an example where core verification was used. In the example case shown here, a core was taken in panel G of the leave slab at 10 in. away from the joint. Figure 5.34 gives a zoomed in view of this location with a red circle denoting the core location.

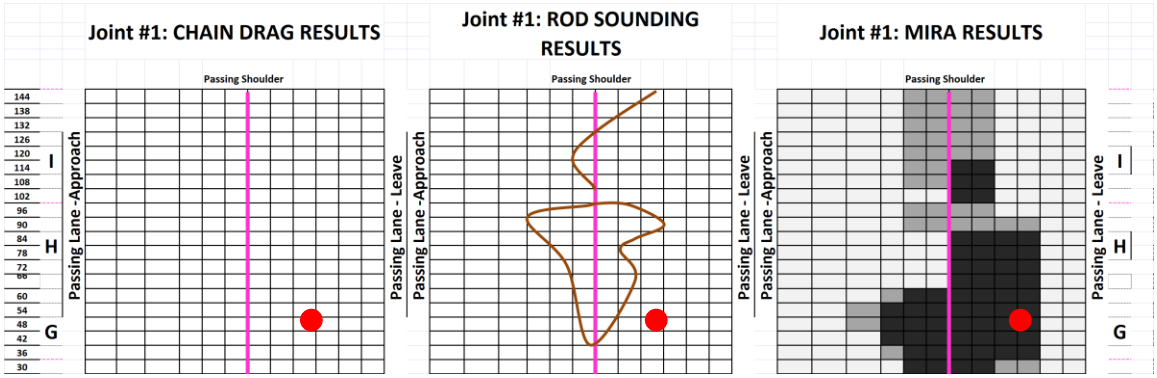

Figure 5-34. Zoomed in view of figure 5.29 showing a core location where ultrasound tomography was the only method to show deterioration.

Figure 5.35 shows the SAFT panoramic reconstructions of the Joint 1 leave slab panel G location. Shallow high intensity reflections can be observed on the right side of the SAFT panoramic at this location. Figure 5.36 shows the associated core where delamination is clearly visible at the depth of the indications from ultrasonic array analysis.

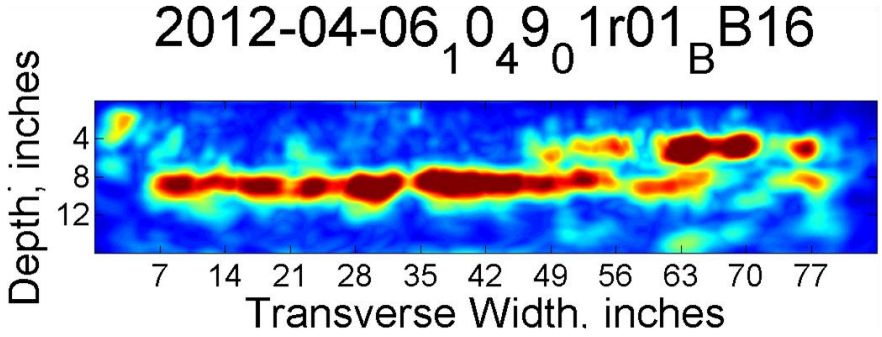

Figure 5-35. SAFT panoramic reconstructions of the Joint 1 leave slab (panels G and F) at 10 and 8 in. from the joint.

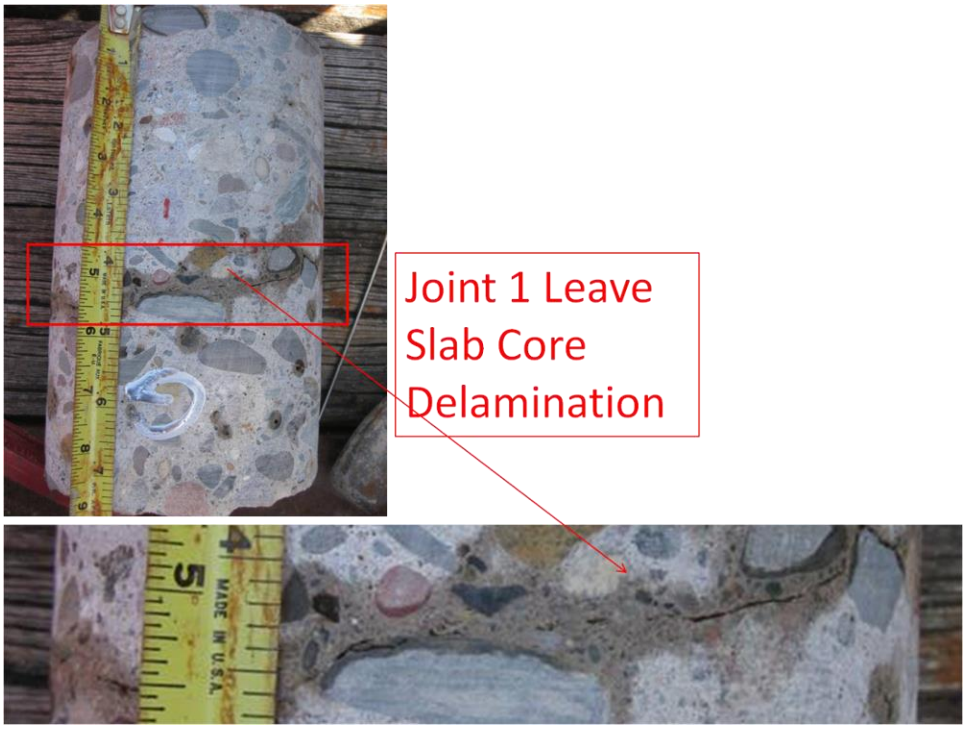

Figure 5-36. Core centered at approximately 10 in. from joint one in the leave slab direction.

6 Conclusions and Future Work Recommendations

6.1 Conclusions

Quantitative subsurface nondestructive diagnostics of concrete pavements is an important and challenging problem. This thesis documented development of methods that can be applied to signal interpretation of ultrasonic linear array transducer pair data or combinations, thereof for concrete structures. These developments were made with the aim of improving the quantitative analysis capabilities through the use of various reconstructions and automated detection methods.

The fundamental synthetic aperture reconstruction (SAR) expression and synthetic aperture focusing technique (SAFT) formulation were generalized for signals sent from one location but received at various locations along the surface. This method was used to determine locations of changes in acoustic impedance by integrating the impulse time histories from each transducer pair over each point within the region of interest (ROI). Various methods were also introduced in the reconstruction process to improve the focusing capabilities of the SAFT reconstructions. Methods for reliable determination of parameters such as shear wave velocity and impulse time-history shift factors were applied to associate the impulse time-histories with the correct conversion from time to space domain. Additionally, the Hilbert transform was applied for further focusing of the instantaneous amplitudes within the reconstruction to the physical location of changes in acoustic impedance. An apodization factor was developed to eliminate structural noise by accounting for the divergent nature of elastic wave propagation as wells as the effect of incident angle on reflectivity when reconstructing the image.

Virtual arrays and associated data fusion and reconstruction techniques were also developed for important practical concrete pavement problems. It was illustrated that situations where measurements may be inconclusive when the linear array is located above the edge of a defect can be corrected by creating a virtual array that expands the

reconstructed image. The SAFT-Pan method was developed to utilize an additional redundancy in the measurements and create large panoramic cross sections with increased resolution. To address issues with possible imprecise relative scan locations this method was further improved by analysis of the similarity of potential overlapping regions of adjacent scans. The resulting procedure, SAFT-EPan, was shown to provide accurate focusing of the reflectivity even in cases where the target scan locations differ from the actual scan locations. In addition, three-dimensional reconstructions (SAFT-3D) of subsurface characteristics were developed to simplify interpretation of multiple ultrasonic array scans using various techniques for interpolation and filtering.

While the Kirchoff-migration based SAFT reflectivity reconstructions discussed above created an intuitive focused image of subsurface reflectivity in pavements, qualitative analysis of these reconstructions require expertise and can be time consuming. Several pavement specific quantitative procedures were developed allowing for automated interpretation of the reconstructions to increase productivity while often improving the accuracy and reliability of the interpretation.

Each of the analytical tools described above was subjected to extensive validation through comparison with ground truth forensics and field case studies. It was demonstrated that the concrete pavement-related subsurface characterization can be reliably quantified using the signal interpretation techniques developed in this thesis. This included important concrete pavement problems such as reinforcement location (sections 3.1.2, 4.1.2, and 5.1.2), PCC thickness (sections 4.1.1 and 5.1.1), bond condition assessment (sections 4.3 and 5.2), poor consolidation (section 4.1.4 and 4.4.1), delamination (sections 4.1.3, 4.2.1, 4.4.1, 4.4.2, and 5.3.2) and deterioration (section 4.1.5 and 5.3.1). The favorable comparison with other nondestructive testing methods makes this emerging technology and associated methods developed in this thesis and attractive alternative for improvement of concrete pavement subsurface evaluation.

Automated inclusion, thickness, and flaw detection interpretation techniques were also validation through comparison with ground truth forensic of full-scale concrete

pavements. Blind testing showed these automated procedures to be capable of identifying designed features such as reinforcement location and thickness detection, as well as naturally occurring subsurface defects. It was also observed that the generalized reference scan selection procedure for UTSA analysis allowed for damage detection even for cases where *a priori* knowledge of the presence, type, and location of any possible defects are unknown. The automated methods developed in this study proved useful for rapid large-scale concrete pavement subsurface quantitative interpretation by allowing for more productive and objective analysis. In some cases this eliminated the need for subjective engineering judgment where it is not feasible to evaluate each reconstruction in detail.

6.2 Future Work Recommendations

While the signal interpretation concepts, developments, and adaptations discussed in this thesis were presented with the objective of advancing the state of the art in nondestructive evaluation of concrete pavements, most of the work presented in this thesis is also applicable for other structural applications. For example, delamination is a very common distress in concrete bridge decks. The methods for delamination detection in concrete pavements should be applicable for this important structural problem.

The work presented in this thesis was applied to elastic wave propagation using a ultrasonic linear array system, but the mathematical approach to many of the signal interpretation methods presented in this thesis are analogous to techniques for interpretation of impulse responses based on different physical principles such as electromagnetic wave propagation (Langenberg et al., 2004, Marklein et al., 2002, Marklein et al., 2006). It would be useful to use and adapt some of the same signal interpretation methods presented in this thesis to different applicable structures and nondestructive testing methods using similar laboratory and field trials for validation.

Additionally, while the analysis methods presented in this thesis where demonstrated to provide subsurface assessments that are practical for pavement condition evaluation, steps need be taken to make the measurement process and evaluation more routine. While the automated tools were designed to mitigate the need for engineering judgment, the algorithms developed to process the data should be made more user-friendly to allow for more routine application. Also, similar tools should be developed for other types of distresses. Additionally, it would be useful to have an archived comprehensive set of examples of ground truth comparisons for various applications that are available for potential users to determine applicability for their specific problem.

Although the ultrasonic linear array methods presented in this study can be used as a stand-alone tool for concrete pavement diagnostics, it can also be effectively used in combination with other NDT methods. More work in determining situations where complementary aspects of different techniques for data fusion would also significantly improve the quality of concrete pavement nondestructive evaluation.

Often the testing procedure and analysis methods are a tradeoff between accuracy, time, and cost to acquire and process the data. While efforts were made in this thesis to improve the productivity of signal interpretation to allow for full-scale testing of concrete pavements, the focus was based on validation and establishing baseline capabilities of the signal interpretation techniques for various concrete pavement problems. More work should be conducted to further improve the data analysis and scanning process productivity. This could be accomplished using automated data collection processes.

Bibliography

1. ABDALLAH, I. N., WILLIAMS, R. & NAZARIAN, S. Application of Data Fusion Using Fuzzy Logic Method to Nondestructive Evaluation of Pavements. Transportation Research Board 88th Annual Meeting, 2009.
2. ACHENBACH, J. D. 1973. Wave propagation in elastic solids, North-Holland Amsterdam.
3. AMERICAN ASSOCIATION OF STATE, H. & TRANSPORTATION, O. 1993. AASHTO Guide for Design of Pavement Structures, 1993, American Association of State Highway & Transportation Officials.
4. ANSARI, F. & STURE, S. Nondestructive testing of concrete elements and structures. 1992. ASCE.
5. ARNDT, R. W., CUI, J. & HUSTON, D. R. MONITORING OF REINFORCED CONCRETE CORROSION AND DETERIORATION BY PERIODIC MULTI-SENSOR NON-DESTRUCTIVE EVALUATION. AIP Conference Proceedings, 2011. 1371.
6. AVSETH, P., MUKERJI, T. & MAVKO, G. 2005. Quantitative seismic interpretation: Applying rock physics tools to reduce interpretation risk, Cambridge University Press.
7. BAMLER, R. 1992. A comparison of range-Doppler and wavenumber domain SAR focusing algorithms. Geoscience and Remote Sensing, IEEE Transactions on, 30, 706-713.
8. BARBONE, P. E. & GOKHALE, N. H. 2004. Elastic modulus imaging: on the uniqueness and nonuniqueness of the elastography inverse problem in two dimensions. Inverse Problems, 20, 283.
9. BASU, U. & CHOPRA, A. K. 2004. Perfectly matched layers for transient elastodynamics of unbounded domains. International Journal for Numerical Methods in Engineering, 59, 1039-1074.
10. BELLI, K., WADIA-FASCETTI, S. & RAPPAPORT, C. 2008. Model based evaluation of bridge decks using ground penetrating radar. Computer-Aided Civil and Infrastructure Engineering, 23, 3-16.

11. BELYTSCHKO, T. & HUGHES, T. J. R. 1983. Computational methods for transient analysis. Amsterdam, North-Holland(Computational Methods in Mechanics., 1.
12. BENAROYA, H. 2004. Mechanical vibration: analysis, uncertainties and control, CRC.
13. BENEDETTO, A., MANACORDA, G., SIMI, A. & TOSTI, F. 2012. Novel perspectives in bridges inspection using GPR. Nondestructive Testing and Evaluation, 27, 239-251.
14. BHARDWAJ, M. C., NEESON, I. & STEAD, G. 2000. Introduction to contact-free ultrasonic characterization and analysis of consolidated materials. NDT. net, 5.
15. BISHKO, A. V., SAMOKRUTOV, A. A. & SHEVALDYKIN, V. G. Ultrasonic Echo-Pulse Tomography of Concrete Using Shear Waves Low-Frequency Phased Antenna Arrays. 17th World Conference on Nondestructive Testing, 2008. 25-28.
16. BLOUIN, A., LEVESQUE, D., NERON, C., DROLET, D. & MONCHALIN, J. P. 1998. Improved resolution and signal-to-noise ratio in laser-ultrasonics by SAFT processing. Optics Express, 2, 531-539.
17. BLUM, P. 1997. Physical properties handbook: a guide to the shipboard measurement of physical properties of deep-sea cores. ODP Tech. Note, 26.
18. BOLOTIN, V. V. 1961. Dynamic edge effect in the elastic vibrations of plates. lnzhenernyi Sbornik (Eng. J.), 31, 3-14.
19. BOLOTIN, V. V., MAKAROV, B. P., MISHENKOV, G. V. & SHVEIKO, Y. Y. 1960. Asymptotic method of investigating the natural frequency spectrum of elastic plates. Raschet na Prochnost, Mashgiv, Moscow, 6, 231, 256.
20. BOLOTINA, I., DENNIS, M., MOHR, F., KROENING, M., REDDY, K. M. & ZHANTLESSOV, Y. 3D Ultrasonic Imaging by Cone Scans and Acoustic Antennas.
21. BORWICK, J. 1990. Microphones: technology and technique, Focal Press Oxford.
22. BUCKLEY, J. & LOERTSCHER, H. 1999. Frequency considerations in air-coupled ultrasonic inspection. Insight, 41, 696-9.
23. BUNGEY, J. 2006. Testing of concrete in structures, Routledge.
24. BÜYÜKÖZTÜRK, O. 1998. Imaging of concrete structures. NDT & E International, 31, 233-243.
25. CAO, Y. 2011. Full Waveform Analysis of Ground Penetrating Radar Measurements. UNIVERSITY OF MINNESOTA.

26. CAO, Y., GUZINA, B. B. & LABUZ, J. F. 2008. Pavement evaluation using ground penetrating radar.
27. CAO, Y., LABUZ, J. & GUZINA, B. Evaluating a Pavement System Based on GPR Full-Waveform Simulation. Transportation Research Board 90th Annual Meeting, 2011.
28. CARINO, N. J. Characterization of electromagnetic covermeters. Conference proceedings of the british institute of non-destructive testing international conference, ndt in civil engineering 14-16 april 1993, liverpool university. volume 2, 1993.
29. CARINO, N. J. The impact-echo method: an overview. Proceedings of the 2001 Structures Congress & Exposition, May, 2001. 21-23.
30. CATAPANO, I., CROCCO, L., MORABITO, A. F. & SOLDOVIERI, F. 2012. Tomographic imaging of holographic GPR data for non-invasive structural assessment: the Musmeci bridge investigation. Nondestructive Testing and Evaluation, 27, 229-237.
31. CERJAN, C., KOSLOFF, D., KOSLOFF, R. & RESHEF, M. 1985. A nonreflecting boundary condition for discrete acoustic and elastic wave equations. Geophysics, 50, 705-708.
32. CHENG, C. & SANSALONE, M. 1993. The impact-echo response of concrete plates containing delaminations: numerical, experimental and field studies. Materials and Structures, 26, 274-285.
33. CHO, Y. S. 2003. Non-destructive testing of high strength concrete using spectral analysis of surface waves. NDT & E International, 36, 229-235.
34. CHONG, K. P., CARINO, N. J. & WASHER, G. 2003. Health monitoring of civil infrastructures. Smart Materials and Structures, 12, 483.
35. CLAERBOUT, J. F. 2004. Earth soundings analysis: Processing versus inversion, Blackwell Scientific Publications.
36. CLARK, M. R., MCCANN, D. M. & FORDE, M. C. 2003. Application of infrared thermography to the non-destructive testing of concrete and masonry bridges. NDT & E International, 36, 265-275.
37. CLEAR, K. C. 1989. Measuring rate of corrosion of steel in field concrete structures. Transportation research record.
38. CLEMENA, G. G. 1991. Short-pulse radar methods.

39. CLEMEÑA, G. G., JACKSON, D. R. & CRAWFORD, G. C. 1992. Inclusion of rebar corrosion rate measurements in condition surveys of concrete bridge decks. Transportation Research Record.
40. COLTON, D. & KRESS, R. 1998. Inverse acoustic and electromagnetic scattering theory, Springer.
41. DARTER, M. I., BARENBERG, E. J. & SALSILLI, R. A. CALIBRATED MECHANISTIC DESIGN PROCEDURE TO PREVENT TRANSVERSE CRACKING OF JOINTED PLAIN CONCRETE PAVEMENTS. Fifth International Conference on Concrete Pavement Design and Rehabilitation, 1993.
42. DAVIS, A. G. 2003. The nondestructive impulse response test in North America: 1985–2001. NDT & E International, 36, 185-193.
43. DAVIS, A. G., ANSARI, F., GAYNOR, R. D., LOZEN, K. M., ROWE, T. J., CARATIN, H., HEIDBRINK, F. D., MALHOTRA, V. M., SIMONS, B. P. & CARINO, N. J. 1998. Nondestructive Test Methods for Evaluation of Concrete in Structures. ACI.
44. DAVIS, A. G., LIM, M. K. & PETERSEN, C. G. 2005. Rapid and economical evaluation of concrete tunnel linings with impulse response and impulse radar non-destructive methods. NDT & E International, 38, 181-186.
45. DUARTE, M. G., BUTTON, V. L. S. N., MAIA, J. M., COSTA, E. T. & OLIVEIRA, E. J. V. Apodization process of piezoelectric ceramics for ultrasound transducers. Medical Imaging 2003, 2003. International Society for Optics and Photonics, 452-459.
46. DUTOIT, N. E., BRIAN, L. W. & SANG-GOOK, K. I. M. 2005. Design considerations for MEMS-scale piezoelectric mechanical vibration energy harvesters. Integrated Ferroelectrics, 71, 121-160.
47. ECONOMOU, N., VAFIDIS, A., HAMDAN, H., KRITIKAKIS, G., ANDRONIKIDIS, N. & DIMITRIADIS, K. 2012. Time-varying deconvolution of GPR data in civil engineering. Nondestructive Testing and Evaluation, 27, 285-292.
48. EDWARDS, L. & MASON, Q. 2011. Evaluation of Nondestructive Methods for Determining Pavement Thickness. DTIC Document.
49. ESCALANTE, E. 1989. Elimination of IR error in measurements of corrosion in concrete. The Measurement and Correction of Electrolyte Resistance in Electrochemical Tests, 180.

50. GIBSON, A. & POPOVICS, J. S. 2005. Lamb wave basis for impact-echo method analysis. Journal of Engineering mechanics, 131, 438-443.
51. GOLD, B., OPPENHEIM, A. V. & RADER, C. M. Theory and implementation of the discrete Hilbert transform. Proceedings of the Symposium on Computer Processing in Communications (Polytechnic, New York, 1970), 1969.
52. GRAFF, K. F. 1991. Wave motion in elastic solids, Dover publications.
53. GRAY, S. H., NOTFORS, C. H. & BLEISTEIN, N. H. Imaging using multi-arrivals: Gaussian beams or multi-arrival Kirchhoff? 2002 SEG Annual Meeting, 2002.
54. GREEN JR, R. E. 2004. Non-contact ultrasonic techniques. Ultrasonics, 42, 9-16.
55. GRIFFITHS, D. J. & REED, C. 1999. Introduction to electrodynamics, prentice Hall New Jersey.
56. GROVE, J., JONES, K., YE, D. & GUDIMETTLA, J. M. 2012. Nondestructive Tests of Thickness Measurements for Concrete Pavements. Transportation Research Record: Journal of the Transportation Research Board, 2268, 61-67.
57. GUCUNSKI, N., RASCOE, C., PARRILLO, R. & ROBERTS, R. L. Complementary Condition Assessment of Bridge Decks by High-Frequency Ground-Penetrating Radar and Impact Echo. Transportation Research Board 88th Annual Meeting, 2009.
58. GUCUNSKI, N., ROMERO, F., KRUSCHWITZ, S., FELDMANN, R., ABU-HAWASH, A. & DUNN, M. 2010. Multiple complementary nondestructive evaluation technologies for condition assessment of concrete bridge decks. Transportation Research Record: Journal of the Transportation Research Board, 2201, 34-44.
59. GUCUNSKI, N. & WOODS, R. D. 1992. Numerical simulation of the SASW test. Soil Dynamics and Earthquake Engineering, 11, 213-227.
60. GUZINA, B. B. & BONNET, M. 2004. Topological derivative for the inverse scattering of elastic waves. The Quarterly Journal of Mechanics and Applied Mathematics, 57, 161-179.
61. HAHN, S. L. 1996. Hilbert transforms in signal processing, Artech House Boston, MA, USA.
62. HALABE, U. B., VASUDEVAN, A., KLINKHACHORN, P. & GANGARAO, H. V. S. 2007. Detection of subsurface defects in fiber reinforced polymer composite bridge decks using digital infrared thermography. Nondestructive Testing and Evaluation, 22, 155-175.

63. HAZELL, C. R. & MITCHELL, A. K. 1986. Experimental eigenvalues and mode shapes for flat clamped plates. Experimental mechanics, 26, 337-344.
64. HOEGH, K., KHAZANOVICH, L., "Correlation Analysis of 2D Tomographic Images for Flaw Detection in Pavements." ASTM International. Journal of Testing and Evaluation. Volume 40. Issue 2. March 2012."
65. HOEGH, K., KHAZANOVICH, L., MASER, K. R. & TRAN, N. Evaluation of Ultrasonic Technique for Detecting Delamination in Asphalt Pavements. Transportation Research Board 91st Annual Meeting, 2012a.
66. HOEGH, K., KHAZANOVICH, L. & YU, H. T. 2011. Ultrasonic Tomography for Evaluation of Concrete Pavements. Transportation Research Record: Journal of the Transportation Research Board, 2232, 85-94.
67. HOEGH, K., KHAZANOVICH, L. & YU, H. T. Concrete Pavement Joint Diagnostics Using Ultrasonic Tomography. Transportation Research Board 91st Annual Meeting, 2012b.
68. HOEGH, K., YU, T. & KHAZANOVICH, L. Magnetic imaging tools scanner (MIT Scan-2) application in North America: five years after. Proceedings: 9th international conference on concrete pavements, 2008. International Society for Concrete Pavements San Francisco, CA, 450-462.
69. HOSSAIN, M. S. & ELFINO, M. K. 2006. Field Demonstration of Magnetic Tomography Technology for Determination of Dowel Bar Position in Concrete Pavement.
70. HUANG, N. E. & ATTOH-OKINE, N. O. 2005. The Hilbert-Huang transform in engineering, CRC.
71. JAIN, S. 1987. Amplitude-vs-offset analysis: A review with reference to application in western Canada: J. Canadian Journal of Exploration Geophysics, 23, 27-36.
72. JUNGER, M. C. & FEIT, D. 1972. Sound, structures, and their interaction, MIT press Cambridge.
73. KAUSEL, E. 1988. Local transmitting boundaries. Journal of engineering mechanics, 114, 1011-1027.
74. KEEFE, D. H., LING, R. & BULEN, J. C. 1992. Method to measure acoustic impedance and reflection coefficient. The Journal of the Acoustical Society of America, 91, 470.

75. KELLEZI, L. 2000. Local transmitting boundaries for transient elastic analysis. Soil dynamics and earthquake engineering, 19, 533-547.
76. KHAZANOVICH, L., VELASQUEZ, R. & NESVIJSKI, E. G. 2005. Evaluation of top-down cracks in asphalt pavements by using a self-calibrating ultrasonic technique. Transportation Research Record: Journal of the Transportation Research Board, 1940, 63-68.
77. KIMOTO, K., UENO, S. & HIROSE, S. 2006. Image-based sizing of surface-breaking cracks by SH-wave array ultrasonic testing. Ultrasonics, 45, 152-164.
78. KONTOE, S., ZDRAVKOVIC, L. & POTTS, D. M. 2009. An assessment of the domain reduction method as an advanced boundary condition and some pitfalls in the use of conventional absorbing boundaries. International journal for numerical and analytical methods in geomechanics, 33, 309-330.
79. KOSMATKA, S. H., WILSON, K. 2011. Design and Control of Concrete Mixtures: The guide to applications, methods, and material. Portland Cement Association.
80. KRAUTKRAMER, J. Unconventional methods of generating, coupling and receiving ultrasound in non-destructive testing. 9th World Conference on Non-destructive Testing, 1980.
81. KRSTULOVIC-OPARA, N., WOODS, R. D. & AL-SHAYEA, N. 1996. Nondestructive testing of concrete structures using the Rayleigh wave dispersion method. ACI Materials Journal, 93.
82. KSCHISCHANG, F. R. 2006. The hilbert transform. University of Toronto.
83. LANGENBERG, K. J., MARKLEIN, R., MAYER, K., KRYLOW, T., AMPHA, P., KRAUSE, M. & STREICHER, D. 2004. Wavefield inversion in nondestructive testing. Electromagnetics in a Complex World, 277-285.
84. LI, J., ZOLLINGER, D. G. & LYTTON, R. L. 2008. Detection of Delamination in Concrete Pavements Using Ground-Coupled Ground-Penetrating Radar Technique. Transportation Research Record: Journal of the Transportation Research Board, 2087, 68-77.
85. LIANG, J. R. & LIAO, W. H. 2009. Piezoelectric energy harvesting and dissipation on structural damping. Journal of Intelligent Material Systems and Structures, 20, 515-527.

86. LIN, L. & CHU, F. 2011. Approximate entropy as acoustic emission feature parametric data for crack detection. Nondestructive Testing and Evaluation, 26, 119-128.
87. LINGVALL, F., OLOFSSON, T. & STEPINSKI, T. 2003. Synthetic aperture imaging using sources with finite aperture: Deconvolution of the spatial impulse response. The Journal of the Acoustical Society of America, 114, 225.
88. LIU, P. L. & YEH, P. L. 2010. Vertical spectral tomography of concrete structures based on impact echo depth spectra. NDT & E International, 43, 45-53.
89. LIU, T., ZHOU, J., OSTERMAN, K. S., ZHANG, P., WOODHOUSE, S. A., SCHIFF, P. B. & KUTCHER, G. J. Measurements of radiation-induced skin changes in breast-cancer radiation therapy using ultrasonic imaging. BioMedical Engineering and Informatics, 2008. BMEI 2008. International Conference on, 2008. IEEE, 718-722.
90. LOULIZI, A. 2001. Development of ground penetrating radar signal modeling and implementation for transportation infrastructure assessment. Virginia Polytechnic Institute and State University.
91. LUE, N., CHOI, W., POPESCU, G., BADIZADEGAN, K., DASARI, R. R. & FELD, M. S. 2008. Synthetic aperture tomographic phase microscopy for 3D imaging of live cells in translational motion. Optics express, 16, 16240-16246.
92. LUUKKALA, M. & MERILÄINEN, P. 1973. Metal plate testing using airborne ultrasound. Ultrasonics, 11, 218-221.
93. MAIERHOFER, C. 2003. Nondestructive evaluation of concrete infrastructure with ground penetrating radar. Journal of Materials in Civil Engineering, 15, 287-297.
94. MALHOTRA, V. M. & CARINO, N. J. 2004. Handbook on nondestructive testing of concrete, ASTM International.
95. MANNING, D. G. & HOLT, F. B. 1980. Detecting delamination in concrete bridge decks. Concrete International, 2, 34-41.
96. MARCHETTI, M., LUDWIG, S., DUMOULIN, J., IBOS, L. & MAZIOUD, A. Active infrared thermography for non-destructive control for detection of defects in asphalt pavements. 9th international conference on quantitative infrared thermography, 2008.
97. MARKLEIN, R., MAYER, K., HANNEMANN, R., KRYLOW, T., BALASUBRAMANIAN, K., LANGENBERG, K. J. & SCHMITZ, V. 2002. Linear and

nonlinear inversion algorithms applied in nondestructive evaluation. Inverse problems, 18, 1733.

98. MARKLEIN, R., MIAO, J., RAHMAN, M. & LANGENBERG, K. J. Inverse scattering and imaging in NDT: recent applications and advances. Proceedings of European Conference on Non-Destructive Testing (ECNDT'06), 2006. Berlin.
99. MARPLE JR, L. 1999. Computing the discrete-time "analytic" signal via FFT. Signal Processing, IEEE Transactions on, 47, 2600-2603.
100. MASER, K. R. 1996. Condition assessment of transportation infrastructure using ground-penetrating radar. Journal of infrastructure systems, 2, 94-101.
101. MASER, K. R. 2000. Pavement characterization using ground penetrating radar: State of the art and current practice. Astm special technical publication, 1375, 313-326.
102. MASER, K. R. Integration of Ground Penetrating Radar and Infrared Thermography for Bridge Deck Condition Evaluation. Proc. of Symp. NDE/NDT for Highways and Bridges, SMT, 2008. Citeseer, 67-74.
103. MASER, K. R. & RODDIS, W. M. K. 1990. Principles of thermography and radar for bridge deck assessment. Journal of transportation engineering, 116, 583-601.
104. MATLAB User's Guide. 1998. "The Mathworks. Inc., Natick, MA.
105. MAYER, K., LANGENBERG, K. J., KRAUSE, M., MILMANN, B. & MIELENTZ, F. 2008. Characterization of reflector types by phase-sensitive ultrasonic data processing and imaging. Journal of Nondestructive Evaluation, 27, 35-45.
106. MINALGA, E., PAYNE, A., MERRILL, R., TODD, N., VIJAYAKUMAR, S., KHOLMOVSKI, E., PARKER, D. L. & HADLEY, J. R. 2012. An 11-channel radio frequency phased array coil for magnetic resonance guided high-intensity focused ultrasound of the breast. Magnetic Resonance in Medicine.
107. MOHEIMANI, S. O. R. 2003. A survey of recent innovations in vibration damping and control using shunted piezoelectric transducers. Control Systems Technology, IEEE Transactions on, 11, 482-494.
108. MOREY, R. M. 1998. Ground penetrating radar for evaluating subsurface conditions for transportation facilities, Transportation Research Board.

109. MOROPOULOU, A., AVDELIDIS, N. P., KOUI, M., AGGELOPOULOS, A. & KARMIS, P. 2002. Infrared thermography and ground penetrating radar for airport pavements assessment. Nondestructive Testing And Evaluation, 18, 37-42.
110. NESVIJSKI, E. 1997. On the Problem of Application of the Conic and Exponential Wave Guiding Extensions for Ultrasonic Transducers for Materials Testing. Journal: NASTA Technical Bulletin, Philadelphia, PA, USA, 49-56.
111. NESVIJSKI, E. G. 2000. Some aspects of ultrasonic testing of composites. Composite structures, 48, 151-155.
112. NESVIJSKI, E. G. 2003. Dry Point Contact Transducers: Design for New Applications. Journal of Nondestructive Testing, 8, 1-10.
113. OPPENHEIM, A. V., SCHAFER, R. W. & BUCK, J. R. 1989. Discrete-time signal processing, Prentice hall Englewood Cliffs, NJ:.
114. PACKARD, R. G. 1984. Thickness design for concrete highway and street pavements.
115. PARK, C. B., MILLER, R. D. & XIA, J. 1999. Multichannel analysis of surface waves (MASW). Geophysics, 64, 800-808.
116. PLATI, C. & LOIZOS, A. 2012. Using ground-penetrating radar for assessing the structural needs of asphalt pavements. Nondestructive Testing and Evaluation, 27, 273-284.
117. POPOVICS, J. S., OH, T. & HAM, S. Effective visualization of impact-echo data for bridge deck NDE. AIP Conference Proceedings, 2012. 1681.
118. POPOVICS, S. & POPOVICS, J. S. A critique of the ultrasonic pulse velocity method for testing concrete. Nondestructive testing of concrete elements and structures, 1992. ASCE, 94-103.
119. PRATT, D. & SANSALONE, M. 1992. Impact-echo signal interpretation using artificial intelligence. ACI Materials Journal, 89.
120. QI, J., MIAO, J. H. & XIE, Y. X. 2012. Synthetic Aperture Focusing Technique and Contrast Source Inversion Algorithm Applied in Elastic Wave Imaging. Advanced Materials Research, 340, 402-408.
121. RACHLIN, D. 1990. Direct estimation of aberrating delays in pulse-echo imaging systems. The Journal of the Acoustical Society of America, 88, 191.

122. RAO, S., HOEGH, K., YU, T. & KHAZANOVICH, L. 2009. Evaluation of dowel alignment constructability in Portland cement concrete pavements. Transportation Research Record: Journal of the Transportation Research Board, 2098, 86-93.
123. ROSE, J. L. 2004. Ultrasonic waves in solid media, Cambridge university press.
124. RUPITSCH, S. J., MAIER, F. & ZAGAR, B. G. Synthetic Aperture Focusing Technique in High-Frequency Ultrasound Imaging to Locate Layer Delamination. Instrumentation and Measurement Technology Conference, 2006. IMTC 2006. Proceedings of the IEEE, 2006. IEEE, 1953-1958.
125. SAARENKETO, T. & SCULLION, T. 2000. Road evaluation with ground penetrating radar. Journal of applied geophysics, 43, 119-138.
126. SACK, D. A. & OLSON, L. D. 1995. Advanced NDT methods for evaluating concrete bridges and other structures. NDT & E International, 28, 349-357.
127. SADRI, A. & MIRKHANI, K. 2009. Wave Propagation Concrete NDT Techniques for Evaluation of Structures and Materials.
128. SANSALONE, M., CARINO, N. J. & HSU, N. N. 1987. A finite element study of transient wave propagation in plates. Journal of research of the National Bureau of Standards, 92, 267-278.
129. SANSALONE, M. J. & STREETT, W. B. 1997. Impact-echo. Nondestructive evaluation of concrete and masonry.
130. SAXENA, P, HOEGH, K., KHAZANOVICH, L. "Laboratory and analytical modelling of misaligned dowel." International Journal of Pavement Engineering 13.3 (2012): 209-215.
131. SCHICKERT, M., KRAUSE, M. & MÜLLER, W. 2003. Ultrasonic imaging of concrete elements using reconstruction by synthetic aperture focusing technique. Journal of Materials in Civil Engineering, 15, 235-246.
132. SCHMITZ, V., CHAKHLOV, S. & MÜLLER, W. 2000. Experiences with synthetic aperture focusing technique in the field. Ultrasonics, 38, 731-738.
133. SCHUBERT, F. & KOEHLER, B. 2001. Three-dimensional time domain modeling of ultrasonic wave propagation in concrete in explicit consideration of aggregates and porosity. Journal of computational acoustics, 9, 1543-1560.

134. SCHUBERT, F. & KÖHLER, B. 2008. Ten lectures on impact-echo. Journal of Nondestructive Evaluation, 27, 5-21.
135. SCHUBERT, F., LAUSCH, R. & WIGGENHAUSER, H. Geometrical effects on impact-echo testing of finite concrete specimens. Proceedings of International Symposium Non-Destructive Testing in Civil Engineering (NDT-CE), 2003. 16-19.
136. SCHUBERT, F., WIGGENHAUSER, H. & LAUSCH, R. 2004. On the accuracy of thickness measurements in impact-echo testing of finite concrete specimens—numerical and experimental results. Ultrasonics, 42, 897-901.
137. SCOTT, M., DUKE, J. C., DAVIDSON, N., WASHED, G. & WEYERS, R. 2000. Automated characterization of bridge deck distress using pattern recognition analysis of ground penetrating radar data. Materials evaluation, 58, 1305-1309.
138. SCOTT, M., REZAIZADEH, A., DELAHAZA, A., SANTOS, C. G., MOORE, M., GRAYBEAL, B. & WASHER, G. 2003. A comparison of nondestructive evaluation methods for bridge deck assessment. NDT & E International, 36, 245-255.
139. SCULLION, T. & SAARENKETO, T. Ground penetrating radar technique in monitoring defects in roads and highways. Proc, 1995.
140. SHI, L. & SHAO, Z. Ultrasonic damage detection of concrete structures by using pulse-echo sensor arrays and SAFT. Proc. of SPIE Vol, 2009. 749312-1.
141. SHLIVINSKI, A. & LANGENBERG, K. J. 2007. Defect imaging with elastic waves in inhomogeneous–anisotropic materials with composite geometries. Ultrasonics, 46, 89-104.
142. SHOKOUHI, P. & WIGGENHAUSER, H. Multiprobe Ultrasonic Testing for Detection of Delamination in Concrete Bridge Decks. Transportation Research Board 91st Annual Meeting, 2012.
143. SHOKOUHI, P., WOESTMANN, J., SCHNEIDER, G., MILMANN, B., TAFFE, A. & WIGGENHAUSER, H. Nondestructive Detection of Delamination in Concrete Slabs: A Multi-method Investigation. Transportation Research Board 90th Annual Meeting, 2011.
144. SHUEY, R. T. 1985. A simplification of the Zoeppritz equations. Geophysics, 50, 609-614.

145. SNOWDON, P. C., JOHNSTONE, S. & DEWEY, S. 2003. A 2D static ultrasonic array of passive probes for improved probability of detection. Nondestructive Testing and Evaluation, 19, 111-120.
146. SOIZE, C. 2001. Maximum entropy approach for modeling random uncertainties in transient elastodynamics. Journal of the Acoustical Society of America, 109, 1979-1996.
147. SOKOLOV, I. V. 2003. The split-method of ultrasonic nondestructive testing. Nondestructive Testing and Evaluation, 19, 1-13.
148. SONG, P. 2010. Ultrasound Transient Shear Wave Elasticity Imaging for Tendon Tissue.
149. SPIES, M., RIEDER, H., ORTH, T. & MAACK, S. Simulation of ultrasonic arrays for industrial and civil engineering applications including validation. AIP Conference Proceedings, 2012. 841.
150. STEPINSKI, T. 2007. An implementation of synthetic aperture focusing technique in frequency domain. Ultrasonics, Ferroelectrics and Frequency Control, IEEE Transactions on, 54, 1399-1408.
151. STOKOE, K. H., WRIGHT, S. G., BAY, J. A. & ROESSET, J. M. 1994. Characterization of geotechnical sites by SASW method. Technical Reportâ€" Geophysical Characterization of Sites, 15-26.
152. TODORAN, G. 2007. The±α Phase Shift Filter Combination between the Fourier Transform and Hilbert Transform. Acta Electrotehnica, 48, 240.
153. TODORAN, G., HOLONEC, R. & IAKAB, C. 2008. Discrete Hilbert Transform. Numeric Algorithms.
154. TOMPKINS, D., KHAZANOVICH, L, DARTER, M, FLEISCHER. "Design and Construction of Sustainable Pavements." Transportation Research Record: Journal of the Transportation Research Board 2098.-1 (2009): 75-85.
155. VLADIŠAUSKAS, A., MAŽEIKA, L., SLITERIS, R., RAIŠUTIS, R. & JANKAUSKAS, A. 2011. Pulse and frequency responses of broadband low frequency ultrasonic transducers. Ultragarsas" Ultrasound", 66, 32-39.
156. VLADIŠAUSKAS, A., RAIŠUTIS, R., ŠLITERIS, R., SENIŪNAS, G. & JANKAUSKAS, A. 2010. Investigation of the characteristics of the low frequency broadband contact transducers. Ultragarsas (Ultrasound), 65, 41-44.

157. VONRAMM, O. T. & THURSTONE, F. L. 1976. Cardiac imaging using a phased array ultrasound system. I. System design. Circulation, 53, 258.
158. WASHER, G., FENWICK, R., BOLLENI, N. & HARPER, J. 2009. Effects of Environmental Variables on Infrared Imaging of Subsurface Features of Concrete Bridges. Transportation Research Record: Journal of the Transportation Research Board, 2108, 107-114.
159. YU, H. T., TAYABJI, S. D. & TRANSPORTATION RESEARCH, B. Need for Improved Specifications on Dowel Bar Placement Tolerance. Transportation Research Board 86th Annual Meeting, 2007.
160. ZHU, J. & POPOVICS, J. Non-contact detection of surface waves in concrete using an air-coupled sensor. AIP Conference Proceedings, 2002. 1261.
161. ZHU, J. & POPOVICS, J. S. 2007. Imaging concrete structures using air-coupled impact-echo. Journal of engineering mechanics, 133, 628-640.
162. ZHU, J., POPOVICS, J. S. & SCHUBERT, F. 2004. Leaky Rayleigh and Scholte waves at the fluid–solid interface subjected to transient point loading. The Journal of the Acoustical Society of America, 116, 2101.
163. ZOLLINGER, D. G., SENADHEERA, S. P. & TANG, T. 1994. Spalling of continuously reinforced concrete pavements. Journal of transportation engineering, 120, 394-411